A Thesis Submitted for the Degree of PhD at the University of Warwick

**Permanent WRAP **

warwick.ac.uk/lib-publications

The Effect of Increasing Molecular Complexity on the Dynamics of Biologically Relevant Chromophores

From dynamic competition to wavepacket evolution

Jamie D. Young

A thesis submitted in partial fulfilment of the
requirements for the degree of
Doctor of Philosophy

Department of Chemistry
University of Warwick
UK
April 2016

Contents

List of Figures

vii

List of Tables

Acknowledgements

First and foremost I would like to extend my utmost thanks to my project supervisor Dr Vasilios Stavros, a real inspiration to me from the get-go. Your work ethic is unrivalled and something I can only aspire to recreate; if more people worked as hard as you, the world would be a much more pleasant and productive place. Thank you so much for your patience, support, belief and guidance throughout my project and thank you for making my time in your group so enjoyable.

I would be remiss if I didn't take time to extend a special thanks to my 'work-wife', Dr Mick Staniforth for putting up with me and my incessant questions for the last 3 years. I'm certain I would not be the researcher I am today without your support - "You know this, Jamie. Jamie, *you KNOW this*!".

Throughout my time at Warwick I have had the pleasure of working with some of the most wonderful people. Special thanks to: Michael 'Mitch' Horbury (*aka* the Ham Guru), for the many interesting discussions that took place when we should have been writing our theses; my LaTeX sensei, Lewis Baker, my thesis looks this good because of you; Victor Quan, your views on the world are something truly unique; Dr Ed Greenough, who only ever beat me at squash once, but was pretty great at most other things; Nat the Spaniard who joined the dark-side in my final year, it's been a pleasure working and exploring the many nuances of the Portuguese language with you; and finally, Yoann Peperstraete, the mathmagician, while we haven't done many experiments together, I've very much enjoyed (trying to keep up with) your mathematical wizardry!

I would also like to mention the past members of Team Stavros and also the Costantini group: Dr Gareth Roberts, Dr Dave Hadden, Dr Adam Chatterley, Federico Mazzoni, Dr Ada Della Pia, Dr Luís Perdigão, Jon D. Blohm, Dan Warr, James Lawrence, Phil Blowey and the various Masters and summer students over the years. All of you deserve thanks for the countless insightful discussions and also for contributing to the great deal of fun I've had along the way.

This work would not have been possible without the help and support of our fantastic collaborators, in particular Prof. Martin Paterson from Heriot-Watt, Prof. Tim Zwier, Dr Jacob Dean, Patrick Walsh and Joseph Gord from Purdue Univer-

Declaration

This thesis is submitted to the University of Warwick in support of my application for the degree of Doctor of Philosophy. It has been composed by myself and has not been submitted in any previous application for any degree. The work presented (including data generated and data analysis) was carried out by the author except in the cases outlined below:

(1) The majority of the theoretical calculations throughout this thesis were performed by Dr Michael Staniforth at the University of Warwick in collaboration with Prof. Martin Paterson at Heriot-Watt University. The specific sections are as follows:

  i. Section 3.3.1 - Vertical excitation energies, electronic ground and excited state optimised geometries, torsional barriers and potential energy cuts.

  ii. Section 4.2.2 - Electronic ground and excited state optimised geometries for varying torsion angles, potential energy cuts and tunnelling probabilities.

 iii. Section 5.1 - Electronic ground and excited state optimised geometries for phenol and guaiacol.

The exceptions to (1) are as follows:

(2) The structures of the gradient difference (GD) and derivative coupling (DC) branching space motions in Section 3.3.1b and the tunnelling probabilities discussed in Section 3.4.2 were calculated by Dr Gareth M. Roberts at the University of Warwick.

(3) The electronic ground and excited state geometries of syringol shown in Section 5.1 were calculated by Jacob C. Dean at Purdue University.

(4) The TKER spectra of syringol and guaiacol in Section 5.3.4 were collected in collaboration with Prof. Mike Ashfold and Dr Tolga Karsili at Bristol University.

Parts of this thesis have been published by the author:

Chapter 3:

Young, J. D., Staniforth, M., Chatterley, A. S., Paterson, M. J., Roberts, G. M., and Stavros, V. G. *Phys. Chem. Chem. Phys.* **16**(2), 550-562 (2014).

Chapter 4:

Young, J. D., Staniforth, M., Dean, J. C., Roberts, G. M., Mazzoni, F., Karsili, T. N. V., Ashfold, M. N. R., Zwier, T. S., and Stavros, V. G. *J. Phys. Chem. Lett.* **5**(12), 2138-2143 (2014)

Chapter 5:

Young, J. D., Staniforth, M., Paterson, M. J., and Stavros, V. G. *Phys. Rev. Lett.* **114**(23), 233001 (2015).

Abstract

The work undertaken in this thesis focuses on the effect of increasing molecular complexity on the excited state dynamics in biologically relevant chromophores which have been isolated in the gas phase. The prototypical species phenol is used as a foundation upon which the remainder of the thesis is built. By sequentially adding functionality to the phenol archetype, we gradually develop an understanding of the effect such modifications can have on the excited state landscape, and hence the observed dynamics. The results obtained provide some important first steps towards understanding the excited state dynamics exhibited by larger, more complex, biologically relevant systems.

The first part of this thesis presents H atom elimination dynamics from resorcinol (1,3-dihydroxybenzene) following excitation with ultraviolet light. This investigation utilises time-resolved velocity map imaging and ion yield techniques. Building on previous experiments on phenol-type species, this chapter provides detailed insight into the profound effect that a seemingly small modification can have on the excited state landscape in heteroaromatic, phenol-like systems. Increasing the excitation energy allows the competition between tunnelling and internal conversion to be observed; highlighting that as the absorbed energy increases, internal conversion quickly becomes the dominant relaxation pathway.

The results observed in the latter part of the thesis elegantly highlight the sensitivity of time-resolved ion yield spectroscopy for the study of vibrational motion in important biological motifs. For all three species that we investigate: catechol (1,2-dihydroxybenzene), guaiacol (2-methoxyphenol) and syringol (2,6-dimethoxyphenol), exquisite insight into the early-time vibrational motions is garnered. This is achieved by virtue of the varying ionisation cross-section afforded by the dramatic geometry change following photoexcitation (and photoionisation).

The highly complementary techniques of time-resolved ion yield and velocity map imaging utilised throughout this thesis provide unprecedented insight into the excited state dynamics of the target species, and by coupling with high level *ab initio* calculations, we are able to rationalise the dynamics of increasingly complex biologically relevant molecules.

Abbreviations

1D	One-dimensional
2D	Two-dimensional
3D	Three-dimensional
BBO	Beta barium oxide
BDE	Bond dissociation energy
BO	Born-Oppenheimer
CCD	Charge-coupled device
CASSCF	Complete-active space self-consistent field
CI	Conical intersection
DFT	Density functional theory
DOS	Density of states
DNA	Deoxyribonucleic acid
DC	Derivative coupling
eBE	Electron binding energy
eKE	Electron kinetic energy
EOM-CCSD	Equation-of-motion coupled cluster with single and double excitations
FFT	Fast-Fourier transform
fs	Femtosecond
FC	Franck-Condon
FWHM	Full width at half maximum
GD	Gradient difference
IR	Infrared
IRF	Instrument response function
IC	Internal conversion
ISC	Intersystem crossing
IVR	Intramolecular vibrational energy redistribution
IP($_{ad}$)	Ionisation potential (*adiabatic*)
KET	Keto-enol tautomerisation
KE	Kinetic energy
LIF	Laser-induced fluorescence
MCP	Micro-channel plate
MCSCF	Multi-configurational self-consistent field
MECP	Minimum energy crossing point
ns	Nanosecond

OPA	Optical parametric amplifier
PE	Photoelectron
PES	Potential energy surface
ps	Picosecond
POP	Polar onion peeling
PEC	Potential energy cut
REMPI	Resonance enhanced multi-photon ionization
RNA	Ribonucleic acid
SFG	Sum frequency generation
SHG	Second harmonic generation
TDM	Transition dipole moment
TD	Time-dependant
TOF	Time-of-flight
TR-IY	Time-resolved ion yield
TRPES	Time-resolved photoelectron spectroscopy
TKER	Total kinetic energy release
UV/Vis	Ultraviolet/visible
UV	Ultraviolet
VMI	Velocity map imaging
vFC	Vertical Franck-Condon
WKB	Wentzel-Kramers-Brillouin
ZPE	Zero point energy

Chapter 1

Introduction

1.1 Overview

Understanding the interaction of ultraviolet (UV) radiation (*i.e.* sunlight) with biologically relevant molecules is of fundamental importance in the effort towards understanding the evolution of life on this planet. Following absorption of a UV photon, a molecule in its excited electronic state will often exhibit vastly different reaction dynamics compared to a relaxed ground electronic state molecule and as such may be able to access pathways that were previously inaccessible. This can lead to undesirable, potentially harmful reactions; a pertinent example being photo-induced mutagenesis in DNA leading to melanoma.[1–4] In order to prevent these possibly life-threatening mutations from occurring on a regular basis, the crucial building blocks of life must possess mechanisms through which they are able to dispose of any excess energy quickly *via* non-destructive pathways.

The ability to probe and monitor these deactivation mechanisms comes under the field of *chemical dynamics*, in which we seek to explain time-dependant chemical phenomena, in terms of the detailed motion of nuclei and electrons. Moreover, we seek to characterise the energy content of the system throughout the experiment. Given the often ultrafast[i] nature of energy transfer processes, such as those governing important biological systems, the experimental and theoretical tools used to study these mechanisms must necessarily be able to operate on the timescales at which the dynamics proceed.

The recent advances in laser technology,[5] notably the implementation of mode-locked systems,[6] have made it possible to accurately record snapshots of chemical reactions proceeding on the order of femtoseconds (1×10^{-15} s) giving sub-Ångström (1 Å $= 1 \times 10^{-10}$ m) resolution.[7] The application of ultrafast laser pulses to study chemical processes in 'real time' was pioneered by the investigations of Prof. Ahmed Zewail in the late 80's and early 90's.[8] His work, on di- and tri-atomic molecules[9–12] all the way through to larger systems,[13–15] paved the way for monitoring chemical reactions and processes with femtosecond resolution and ultimately resulted in him being awarded the 1999 Nobel Prize for his important contributions to the field of Femtochemistry.[7]

The work presented here aims to apply femtosecond time-resolved spectroscopic techniques in order to better understand the complex photophysics[ii] associated with biologically relevant species. In this thesis, and in the field in general, a "bottom-up" approach has been favoured,[16] wherein the relaxation pathways followed by smaller "model" heteroatom-containing molecules have first been studied in the gas phase, isolated from external effects (*e.g.* solvent perturbations *etc.*), with the

---

[i]In this thesis, the term *ultrafast* refers to processes that occur on timescales faster than nanoseconds (1 ns $= 1 \times 10^{-9}$ s)

[ii]It is worthwhile highlighting the important difference between photochemistry and photophysics. *Photochemistry* is responsible for the chemical reactions initiated by light, while *photophysics* deals with the relaxation mechanisms that occur within single molecules after excitation.
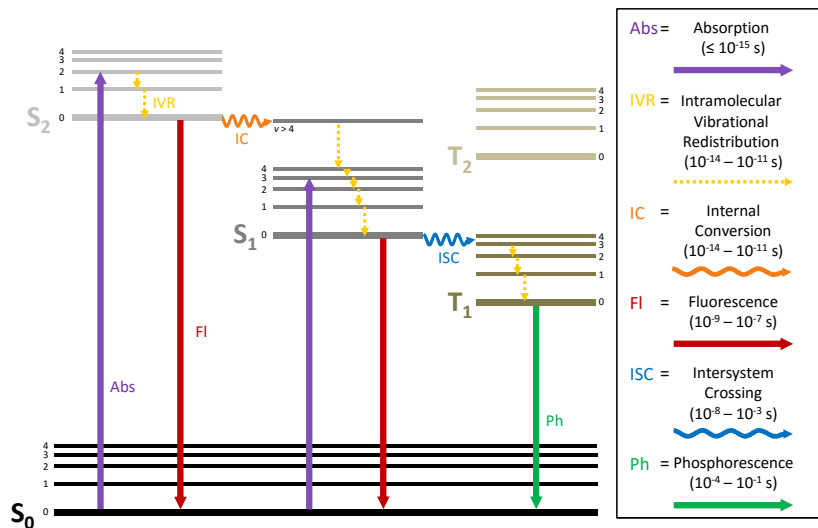
Figure 1.1: Jablonski diagram depicting molecular states and the various photophysical processes that connect them. Example timescales for each of the processes are shown on the right side of the diagram.

understanding that the molecules investigated play an important role as UV chromophores in a multitude of larger biological species, such as the aromatic amino acids,[17–22] DNA bases[23–31] and (eu)melanin pigments.[32–36] The molecular complexity is then increased, as well as potentially introducing solvent perturbation, in order to explore more complex and hence more realistic scenarios. With this approach in mind the introduction to this thesis is structured as follows: initially we explore the possible relaxation pathways that are available to photoexcited species, before moving on to discuss excited state landscapes and the rules and principles that govern transitions within these states. Next, a brief introduction to wavepacket formation and coherent behaviour is given, leading into a description of femtosecond pump-probe spectroscopy, highlighting some important examples of probing techniques. Finally, the concept of photostability is reviewed, focussing primarily on the motivation for the studies reported in later chapters.

1.2   Relaxation Processes

Following the absorption of a photon, a molecule in an excited electronic state will evolve as a function of time, usually relaxing to lower energy levels. It is the various deactivation mechanisms that we are attempting to resolve, and what follows is an introduction to the ways in which a polyatomic system is able to release excess energy. It is important to note as we are discussing these processes that the relative *photostability* of a biological species is governed by the rates of each process and the competition between them, hence important time-frames will be highlighted when appropriate.

The topic of molecular photostability and photoprotection will be recurring themes throughout this thesis. In essence, if a molecule is able to release excess

energy on a timescale that outcompetes any potentially harmful side reactions, the molecule is deemed to be photostable under UV irradiation. A simple example of photostable systems is that of carotenoids. These species possess highly efficient internal conversion pathways that outcompete other photochemical processes allowing the excess energy to be dissipated as heat.[37–39] Figure 1.1 shows a Jablonski diagram that summarises several of the pathways that are relevant to the work reported in the subsequent chapters of this thesis. We will now consider each part of the figure in turn.

1.2.1   Absorption

The first step in the Jablonski diagram, and our experiments, is the initial excitation step, indicated by the vertical (see Section 1.3.2) purple arrow (Abs) in Figure 1.1. The absorption of a UV photon leads to the promotion of an electron from a lower electronic state to a higher one.[iii] The timescale for the initial photon absorption process is sub-femtosecond ($\leq 1 \times 10^{-15}$ s) and is considered instantaneous when compared to the relaxation pathways, see Section 1.3.1. Absorption processes are prevalent throughout this thesis, with both pump and probe steps requiring the absorption of one, or many, UV photons. The former initiates the chemistry, while the latter ionises the particle allowing us to detect it.

There are a number of factors that control the rate and efficiency of an absorption process (and equivalently an emission process) and we will go on to discuss many of them in the following paragraphs. Fundamentally, however, in order for a molecule to be able to interact with an incident electromagnetic field and absorb a photon, it must possess, if only transiently, a dipole that oscillates resonantly with the frequency of the incident photon. This dipole is expressed quantum mechanically in terms of the transition dipole moment (TDM), $\vec{\mu}_{if}$ between two states, i and f:[40]

$$\vec{\mu}_{if} = \int \psi_f^* \, \hat{\mu} \, \psi_i \, d\tau \tag{1.1}$$

where ψ_i and ψ_f are the wavefunctions[iv] of the initial and final state respectively, $\hat{\mu}$ is the molecular dipole moment operator and $\int d\tau$ indicates that we are integrating over all coordinates. In general terms, the TDM, also known as the electric dipole moment, is a vector that aligns from a negative charge, q^-, to a positive charge, q^+, which are displaced relative to each other by some distance, $\mathbf{r}$. Within our experiments, those molecules whose TDM is aligned parallel to the polarisation

---

[iii]Herein, the ground electronic state will be termed S_0. Higher lying electronic states will be labelled S_n, D_n or T_n (where $n \geq 0$) for singlet, doublet and triplet states, respectively. A description of the transitions electronic character ($\pi/\sigma/n$) will be given in parentheses. Photodissociation products will be labelled according to the states they are formed in ($\tilde{X}, \tilde{A}, \tilde{B}$ etc.)

[iv]The wavefunction is a mathematical description of a system and contains all the information about it, e.g. the energy and momentum of the particle.

vector of the excitation laser (ε_{pu}) will be preferentially promoted to the excited state, falling off with a cos^2 distribution as the TDM tends towards perpendicular. Due to this, the TDM is particularly important when it comes to correlating our experiments with the 'lab frame' *i.e.* the alignment of the molecular species under investigation relative to the detector array. This has important connotations for measuring the angular distribution of photodissociation events, see Section 2.3.3.

1.2.2 Radiative Decay

Following the absorption step, a molecule in its excited state is able to release excess energy through the emission of a photon. This can be a *spontaneous* process or *stimulated* by a second incident photon of the same frequency. Fluorescence (Fl - red arrow in Figure 1.1) and phosphorescence (Ph - green arrow in Figure 1.1) are radiative processes that involve the spontaneous release of excess energy. The former involves decay from an excited singlet state (S_n) while the latter first undergoes intersystem crossing (ISC - see Section 1.2.3), to an excited triplet state (T_n), before returning to the ground state. While the detection of both fluorescence and phosphorescence are immensely powerful spectroscopic techniques,[41,42] they are comparatively slow (typically on the order of nanoseconds and milliseconds, respectively) and as such will be out-competed by the more efficient non-radiative processes described below.[43]

Stimulated emission, as mentioned above, occurs when a system that is already in an excited state interacts with a second photon. The emitted photon will be created in coincidence with the incident electromagnetic wave and will thus possess identical phase, frequency, polarisation and propagation vector. When there is notable population inversion, *i.e.* significantly more population in the excited state relative to the ground state, the rate of stimulated emission dominates absorption resulting in a net amplification of the radiation. This is the process of laser action and is pivotal in the operation of femtosecond laser systems.

1.2.3 Non-radiative Decay

IVR

The first non-radiative process we will explore is intramolecular vibrational energy redistribution (IVR - dashed, yellow lines in Figure 1.1). This is the mechanism by which vibrational energy localised in one, or a few, initially populated states is dispersed amongst other vibrational modes[v] within a given electronic state.[44,45]

It is pertinent at this stage to make an important distinction between vibrational *redistribution* and vibrational *relaxation*. When isolated in the gas phase, as in the experiments described here, the total internal energy of the system cannot decrease,

---

[v]A vibrational mode can be described as a specific stretch, bend or torsion, or combination thereof, of atoms in the molecule.

due to the conservation of energy, meaning the excess vibrational energy is not *removed* from the system, it is simply redistributed into modes orthogonal to the coordinate of interest. As a result of this, the IVR arrows in Figure 1.1 are only correct when viewed along a specified coordinate.[vi] On the other hand, in the condensed phase it is more appropriate to use the term *relaxation* since the excess vibrational energy is irreversibly lost as heat to the solvent, actively lowering the total energy of the target molecule.

In smaller molecular systems, there are very few vibrational modes meaning that IVR can be a reversible process. This allows for the observation of periodicity in the vibrational mode population as the excited state evolves.[45] In larger systems however, the density of (vibrational) states (DOS - ρ) is high enough such that we can think of them as a 'bath', or continuum, to which energy flows irreversibly. This being the case, we can approximate the rate of IVR using *Fermi's golden rule*:[43,46]

$$k_{\text{IVR}} = \frac{2\pi}{\hbar}|M_{fi}|^2 \rho_f \tag{1.2}$$

This succinct expression asserts that the rate of IVR (k_{IVR}) is proportional to the square modulus of the transition matrix element, *i.e.* the strength of the coupling between the two states, and the density of vibrational levels in the final state (ρ_f).

As shown in the Jablonski diagram above, the timescale for IVR is often much faster than that of the other relaxation mechanisms and as such is able to out-compete them.[45] Once the molecule has relaxed to the lower vibrational level, it can then undergo, for example, spontaneous emission; the ejected photon being of longer wavelength (lower energy) than the originally absorbed photon. The observation of a shift in emission wavelength, relative to absorption, is known as the Stokes shift.[41,47]

Internal Conversion and Intersystem Crossing

IVR dealt with the coupling of vibrational levels within the same electronic state. However, the possibility also exists for *vibronic* levels to have significant coupling such that population can be efficiently transferred between different electronic states.[48] Much the same as radiative decay, this process can occur from states of singlet or triplet multiplicity. If the spin of the system is conserved, *e.g.* $S_2 \rightarrow S_1$, the process is termed internal conversion (IC - orange arrow in Figure 1.1).

The rate of IC can be treated in a similar fashion to IVR (Equation 1.2), where k_{IC} is dependent on the coupling strength between the initial and final vibronic states and the vibrational DOS in the final state (following a Fermi's golden rule model). In the case of IC the strength of the coupling between the two vibronic levels is a function of the energy difference between the two states (ΔE) and as

---

[vi]If we were able to draw an accurate *multi-dimensional* Jablonski diagram, the arrows would point to energy levels perpendicular to the ones depicted in the diagram.

such k_{IC} has the following proportionality:[49]

$$k_{IC} \propto exp^{(-\Delta E / h\nu)} \tag{1.3}$$

where ν is the vibrational frequency. Given this relationship, it follows that the probability of IC is highest when the initial and final state are close in energy, *i.e.* ΔE is small. There exists a special case when ΔE becomes zero, *i.e.* the two states are energetically degenerate. In this instance, the states cross and form what is known as a *conical intersection* (CI). CIs are ubiquitous in polyatomic systems and are responsible for a significant proportion of the excited state relaxation mechanisms discussed through the course of this thesis. A more rigorous description is given in Section 1.3.3.

Formally, the transfer of population between states of different spin is forbidden. However, spin-orbit coupling, which is enhanced in the presence of heavy atoms (*e.g.* bromine and iodine), results in intersystem crossing (ISC - blue arrow in Figure 1.1).[50] Following transfer to the triplet manifold ($S_1 \rightarrow T_1$), the excited state population can become "trapped", where after stepping down the vibrational ladder *via* IVR, the spin forbidden radiative transition (phosphorescence) is the most probable pathway accessible for decay back to S_0.[vii] Since this process is considered classically forbidden, the transition is kinetically disfavoured and occurs orders of magnitude slower than the allowed transitions observed in fluorescence.[50] As with IC the probability of ISC is enhanced if the vibrational energy levels of the initial (S_n) and final (T_n) states lie close in energy.

1.2.4 Photodissociation

The final molecular relaxation process that is relevant to the work presented here is photodissociation, or photolysis. Figure 1.2 shows a simple schematic of the dissociation process, which can be explained as follows: the absorption step first promotes electron density from the ground state into the A–B anti-bonding orbital ($\pi\sigma^*$, formed as a result of a $\sigma^* \leftarrow \pi$ transition). This causes the two nuclei to repel each other causing a lengthening of the A–B bond until, eventually, the atoms are sufficiently separated that the bond between them is broken, yielding A and B radicals.[viii] The schematic in Figure 1.2 shows a *direct dissociation* process, where population is promoted straight to the dissociative state. The more common situation, owing to the fact that the absorption coefficients of dissociative states are often small, is when electrons are first excited to a higher lying bound state (often an optically bright $\pi\pi^*$ state) before undergoing IC onto the dissociative

---

[vii]ISC from the triplet manifold *back* to the ground state ($T_1 \rightarrow S_1$) is also possible, but is again highly unfavourable.)

[viii]The products of such photodissociation mechanisms are often termed photofragments or photoproducts and both of these terms will be used interchangeably throughout the remainder of this thesis.
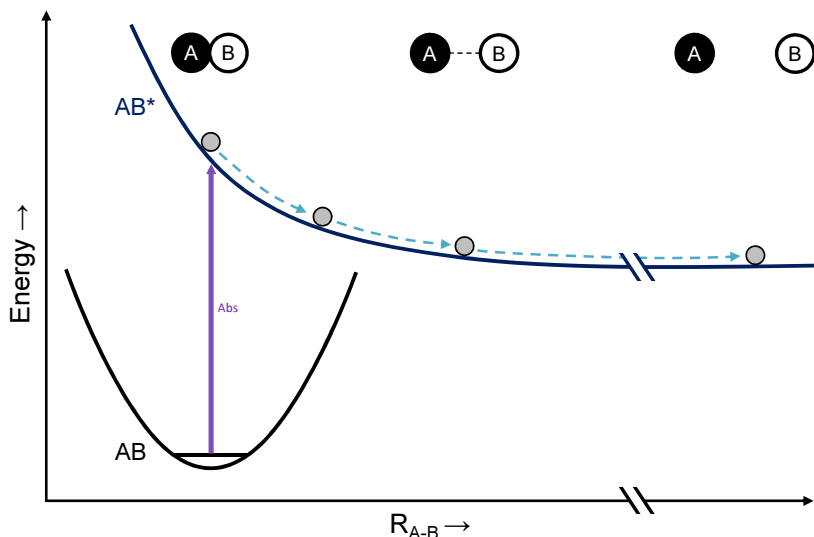
Figure 1.2: Schematic of the photodissociation process. Following absorption of a photon, the bound species AB is promoted to a dissociative state. After some time the A–B bond will extend until eventually the A–B bond is broken, leaving A and B photofragments.

state whereupon bond fission occurs. This is known as *predissociation*, and is the primary photolysis mechanism seen in this thesis. Further detail regarding the role of $\pi\sigma^*$ states in photostability processes is given in Section 1.6.1.

The dissociation of photofragments also provides a convenient method with which to probe photodissociation mechanisms. By tuning our probe laser to be resonant with an electronic transition in a specific photofragment we are able to selectively ionise photofragment species and study their behaviour using spectroscopy. The methodologies for such probing mechanisms are discussed in Section 1.5.2.

1.3 Excited State Landscapes

The energy level diagrams shown in Figures 1.1 and 1.2 are useful tools for visualising the transitions that are able take place within an excited state molecule, however they are not quantitative and as such provide little information regarding the energetics of the excited state. In order to explore the complex deactivation mechanisms within polyatomic systems we must first understand how the energy of the system changes as a function of its electronic and nuclear coordinates. Such a rigorous description of the system, of course, requires quantum mechanical treatment and as such we must solve the time-independent Schrödinger equation, which can be expressed as follows:[50–52]

$$\hat{H}\psi(\mathbf{r};\mathbf{R}) = E\psi(\mathbf{r};\mathbf{R}) \tag{1.4}$$

where E is the energy eigenvalue for the system, $\psi(\mathbf{r};\mathbf{R})$ is the wavefunction that depends on both electronic ($\boldsymbol{r}$) and nuclear ($\boldsymbol{R}$) coordinates, respectively, and $\hat{H}$ is the Hamiltonian operator, which, for a one electron system takes the form:

$$\hat{H} = T_e + T_N + V \tag{1.5}$$

which corresponds to the sum of the kinetic energy operators for both the electron, T_e, and the nuclei, T_N, plus the potential energy of the particles within the system, V. Solving 1.4 analytically is impossible for a system containing more than one electron, and as such we must introduce the Born-Oppenheimer (BO) approximation.

1.3.1   The Born-Oppenheimer Approximation

Adiabatic approximations such as BO and the related rigid-rotor approximation, which greatly simplifies the investigation of rotational motions within molecular systems, are of fundamental importance in quantum mechanics. In addition to providing a mechanical framework within which we can simplify, and attempt to solve, the Schrödinger equation, such assumptions also provide us with the "language" required to discuss the observations made during our experiments. This is vital throughout this thesis and indeed the entire field of chemical dynamics.

The BO approximation is a simplification that utilises the fact that electrons are orders of magnitude lighter compared to nuclei, ($m_{proton}/m_{electron} \approx 1840$), this means that the electronic motion can be thought of as being independent of the nuclear motion. Mathematically, the BO approximation allows the total molecular wavefunction[ix] to be separated into its constituent electronic ($elec$) and nuclear (N) components:

$$\Psi_{total} = \psi_{elec} \times \psi_N \tag{1.6}$$

where the nuclear wavefunction (ψ_N) can be expressed as the product of the vibrational (vib) and rotational (rot) wavefunctions:

$$\psi_N = \psi_{vib} \times \psi_{rot} \tag{1.7}$$

As a result of the above, we can consider any electronic motion to be completely decoupled from the nuclear motions. This simplifies the Schrödinger equation such that it is now possible to express the electronic wavefunction as a function of the Coulombic field created by the nuclei:

$$\hat{H}_e(\mathbf{r};\mathbf{R})\psi(\mathbf{r};\mathbf{R}) = E_{elec}\psi(\mathbf{r};\mathbf{R}) \tag{1.8}$$

In this instance the electronic energy eigenvalue, E_{elec}, is dependant on $\mathbf{R}$, the position of the nuclei. Varying these positions and repeatedly solving the electronic

---

[ix]Formally, the total wavefunction also includes a spin component (ψ_s). However, given the fact that we are only concerned with states of the same spin (singlet states) throughout this thesis, it is not discussed further.

form of the Schrödinger equation yields the molecule's potential energy as a function of nuclear geometry, known as a potential energy surface (PES). [43]

For a diatomic molecule (A–B), the potential energy can be a function of only one variable, the internuclear separation (R), and so it is feasible to construct simple, accurate PESs using theoretical methods. For non-linear polyatomic molecules, however, the situation becomes more complex owing to the increased number of atoms (N), within the molecule. In the case of polyatomic molecules, the Schrödinger equation must be solved for all $3N - 6$ molecular coordinates ($3N$ for the internal x, y and z coordinates of each atom, minus 3 translational and 3 rotational degrees of freedom) leading to a more complicated, multi-dimensional PES. It becomes increasingly more difficult and computationally expensive to construct accurate PESs for large molecules owing to the huge range of vibrational modes, which equate to the $3N - 6$ degrees of freedom, available to non-linear polyatomic species.

As alluded to above, an additional approximation can be made in order to greatly reduce computational expense by the careful selection of which coordinates are responsible for the photochemistry under investigation. It is now somewhat commonplace to construct fairly accurate PESs along various internal coordinates (e.g. X–H bonds, torsional angles etc.) using computational methods to find the approximate solution to the electronic Schrödinger equation. A PES of this type, one along a single coordinate, is more accurately described as a potential energy cut (PEC) since it can be thought of as a two dimensional (2D) slice through the multi-dimensional PES. While these 2D cuts do not provide a full characterisation of the excited state landscape, they can be useful models for visualising the excited state topography. O–H dissociation dynamics, for example, will primarily be a
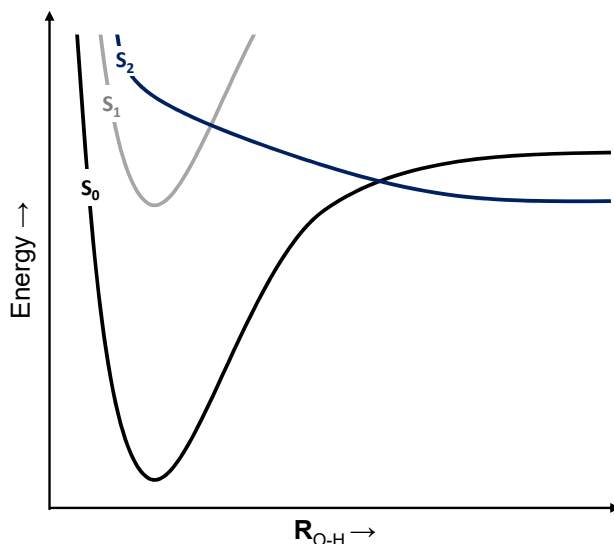
Figure 1.3: A schematic example of a potential energy cut along an O-H coordinate. The cuts shown are the typical form for the R_{O-H} coordinate of a phenol-type system, details of which are discussed in greater detail later in this chapter.

function of the O–H bond length and as such it is viable to construct a PEC along that specific coordinate as a tool for understanding O–H bond fission in simple molecular systems. A representative example of PECs of this form, and hence the form seen throughout this thesis, is shown in Figure 1.3.

1.3.2 Franck-Condon Principle

Now that we have a basic understanding of the form that a molecule's excited state takes we can begin to investigate the quantum mechanical principles that govern the electronic and vibrational transitions that occur within a system.

The Franck-Condon (FC) principle is a well known rule in spectroscopy and quantum chemistry; it states that an electronic transition will take place much faster than the nuclei in the system can respond.[53] Throughout this thesis the "vertical FC (vFC) region" and "FC window" will be discussed. Put simply, the vFC region describes the nuclear coordinates where the transition takes place. The vertical nature of the transition is a result of the FC principle - the absorption process is instantaneous when compared to the nuclear motion hence the system is projected vertically upwards on the stationary PES. The FC window is then the area of the PES where the overlap between the ground and excited state wavefunctions is favourable.

Given this assumption, it follows that the most probable vibronic transition is a vertical transition between *electronic* states, as governed by the TDM, at which the overlap of the relevant *vibrational* wavefunctions, given by the FC factor (see below), is greatest. This is shown schematically in Figure 1.4. The purple arrow represents a good FC overlap between the states $\nu'' = 0$ and $\nu' = 2$, and hence an observed transition between two vibrational levels on the two different electronic surfaces.[x]

The intensity of an allowed electronic transition is proportional to the square of the TDM, $\vec{\mu}_{if}$, for the transition between an initial state, i, and a final state, f. When interacting with polarised light, the transition from i to f is determined by the association between the incoming photon, and $\vec{\mu}_{if}$. By squaring the TDM, and applying the BO approximation to separate the electronic and vibrational motions, we are left with Equation 1.9:[xi]

$$(\vec{\mu}_{if})^2 = \int \left[\psi_f^{*vib} \, \psi_i^{vib} d\tau \right]^2 \int \left[\psi_f^{*elec} \, \vec{\mu}_{if} \, \psi_i^{elec} \, d\tau \right]^2 \tag{1.9}$$

Equation 1.9 governs the intensity of a vibronic transition in the FC region.

---

[x]As is convention, vibrational levels are labelled ν'' and ν' for vibrational states in the ground electronic state and excited electronic state, respectively.

[xi]Formally, there is also a rotational component associated with the TDM which, within the rigid rotor approximation, should result in an additional term in Equation 1.9. Whilst the rotational component provides important information for rotational selection rules, we will not consider rotational transitions since none of the spectra presented in this thesis are rotationally resolved.
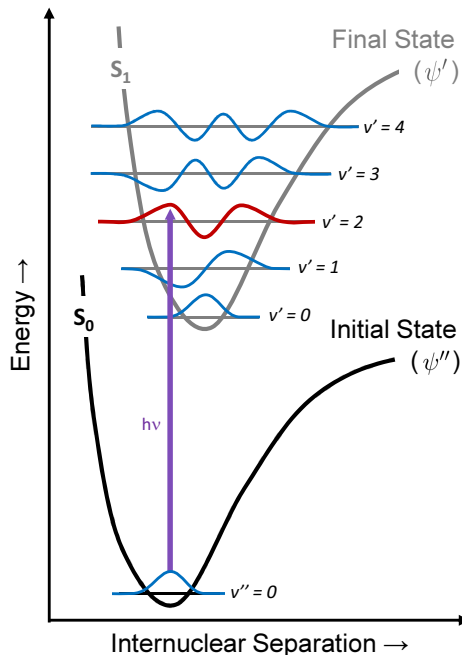
Figure 1.4: Schematic representation of the FC principle showing the overlap between two vibrational energy levels. The purple arrow represents a vertical transition with good overlap and hence an observed peak in the resulting spectrum.

The left hand term of the right hand side of the equation, the square of the overlap integral between the two vibrational wave functions, is known as the *FC factor*. The right hand side describes the electrical component of the transition.

1.3.3 Conical Intersections

As mentioned previously, CIs are a common feature of excited state landscapes in complex polyatomic systems. The adiabatic states within these systems are able to cross in a $(3N - 8)$ subspace of the $(3N - 6)$-dimensional potential energy surface with the remaining two dimensions, the gradient difference $(\vec{\mathbf{g}})$ and the derivative coupling $(\vec{\mathbf{h}})$, forming what is known as the *branching space*.[54] These branching motions are the nuclear motions responsible for lifting the energetic degeneracy between the two electronic surfaces at the crossing point of the CI.[55] The two modes correspond to the gradient of the energy difference between the two electronic states $(\vec{\mathbf{g}})$ and the derivative coupling $(\vec{\mathbf{h}})$, which is parallel to the non-adiabatic coupling gradient. The latter is typically responsible for driving non-adiabatic (vibronic) coupling between the two electronic states and leading to population transfer through the CI.[55] Figure 1.5 shows the crossing of two potential surfaces plotted as a function of the branching space motions, examples of which are also shown. In this view the location of the CI forms a "double cone", hence the name conical intersection, with one cone representing the upper surface and the other corresponding to the lower surface. The crucial fact, for excited state dynamics at least, is that at the exact crossing point, *i.e.* where the two cones meet, the electronic wavefunctions are degenerate. This causes a breakdown in the BO approximation
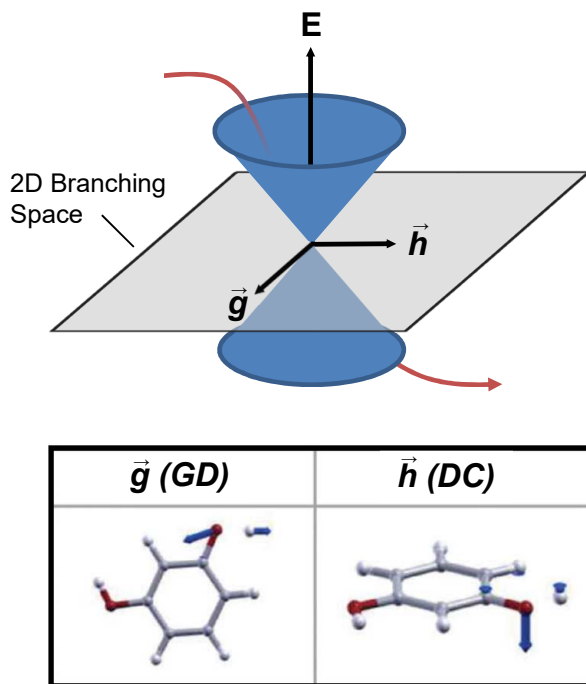
Figure 1.5: The crossing of two PES in the $\vec{\mathbf{g}}$, $\vec{\mathbf{h}}$ branching space (grey shading) resulting in the formation of a conical intersection. Also shown are some representative branching motions calculated for the $1^1\pi\pi^*/1^1\pi\sigma^*$ CI found in resorcinol, see Chapter 3, in order to illustrate the motions that can be responsible for the non-adiabatic coupling of electronic states.

leading to non-adiabatic dynamics (red arrow) that can occur on timescales $< 1\,ps$.

CIs have been found, through high level theoretical calculations, to be an exceptionally efficient pathway for funnelling excited state population, non-radiatively, from higher lying energy levels to lower ones. A particularly relevant example is of DNA and its building blocks. These systems are highly photostable and it is speculated that this is due to the presence of CIs.[31] Such strong couplings between the electronic states in these systems enable photoexcited molecules to redistribute energy efficiently along non-destructive pathways before harmful photochemical reactions can take place. We explore the role of CIs in the photostability of the exemplar system phenol in Section 1.6.

1.3.4   Symmetry

It is pertinent at this point to consider another incredibly important concept which governs the excited state dynamics of the species under investigation throughout this thesis: symmetry. Group theory, or the mathematical application of symmetry to an object, allows us to obtain knowledge of a molecules physical properties without rigorous calculation. The symmetry of a molecule can be very easily related to its physical properties and provides a quick, simple method to determine relevant physical information. For example, it is possible, and in fact somewhat trivial, to determine which transitions can occur between energy levels (selection rules) within a molecule.[50]

With reference to the previous section, symmetry has a large impact on the non-adiabatic coupling of electronic states. In order to successfully couple two electronic states, promoting modes of specific symmetry are often required[56], *i.e.* the product of all three representations must be totally symmetric, symbolically:[57]

$$\Gamma_f \otimes \Gamma_c \otimes \Gamma_i \supseteq \Gamma_{TS} \tag{1.10}$$

where Γ is an irreducible representation, i and f label the initial and final states, respectively, c labels the coupling mode, and TS is the totally symmetric representation of the relevant point group or molecular symmetry group.

A particularly relevant example is the coupling of the S_1 and S_2 states in phenol. It was revealed by Nix *et al.* that within phenol's non-rigid G_4 symmetry group (isomorphous with C_{2v}) the ν_{16a} vibrational mode, which has a_2 symmetry, is required in order to vibronically couple the S_1 ($^1B_2$) and S_2 ($^1B_1$) states, *i.e.* $B_1 \otimes a_2 \otimes B_1 = A_1$.[58,59]

1.4 Wavepackets

The description of the FC principle above highlights excitation with only a single frequency of light. In the case of ultrafast lasers, the pulses are necessarily broadband, *i.e.* possessing a broad optical spectrum, as a result of the uncertainty principle which is discussed below. This means, therefore, that photoexcitation with a femtosecond pulse will excite several vibrational states simultaneously, creating a coherent superposition of the vibrational eigenstates. This is known as a wavepacket and can be thought of as a localised "envelope" of wave action which will evolve as a function of time.[60] The subsequent paragraphs explore the uncertainty principle and its impact on the generation of time-resolved wavepackets.

1.4.1 The Uncertainty Principle and The Time-bandwidth Product

The uncertainty principle is another consideration we must take into account when discussing the quantum mechanical rules that govern pump-probe spectroscopy. Werner Heisenberg in 1927[61] (and later generalised by H. P. Robertson[62]), the principle outlines how one cannot know precisely the value of two non-commuting quantum mechanical operators simultaneously. The most famous of these is Heisenberg's pioneering work which resulted in the following relationship between a particle's linear momentum and position:[61]

$$\Delta p \Delta x \geq \frac{\hbar}{2} \tag{1.11}$$

where Δp is the uncertainty in a particle's momentum and Δx, its uncertainty in position. There exists a similar relationship between energy and time, formalised by Paul Dirac in 1926, which can be expressed as:

$$\Delta E \Delta t \geq \frac{\hbar}{2} \tag{1.12}$$

Here, ΔE and Δt^{xii} are the uncertainties in energy and time, respectively. Perhaps a more ubiquitous, and arguably more useful, form of the above uncertainty is given by the time-bandwidth product for a Gaussian laser pulse:

$$\Delta t = \frac{0.441}{\Delta \nu} \tag{1.13}$$

where $\Delta \nu$ is the full width at half maximum (FWHM) of the pulse in frequency.

The important outcome of this uncertainty, as alluded to above, is that any laser pulse that is well defined in time must, by necessity, have poorly defined energy. For example, a fs pulse will have an energy bandwidth of hundreds of wavenumbers, whereas a ns pulse will have a bandwidth of $\ll 1 \text{ cm}^{-1}$. It is for this reason that any ultrafast excitation pulse will likely promote a superposition of several vibrational modes. A seemingly obvious caveat to this statement is that it can only be true provided the vibrational frequency of the particular mode that is being excited is less than the bandwidth of the laser pulse. An excellent example that goes against this, is the diatomic species, HCl. The H–Cl stretching frequency is greater than the spectral bandwidth of fs pulses and so only a single mode can be excited in this instance.

1.4.2 Wavepacket Generation and Evolution

A time-dependant wavepacket composed of n vibrational wavefunctions (ψ_n) can be expressed mathematically as follows:[50,63,64]

$$\Psi(t) = \sum_n A_n \psi_n e^{-iE_n t/\hbar} \tag{1.14}$$

where E_n is the energy of each of the n wavefunctions, ψ_n, and A_n is a scaling factor that takes into account its FC factor and TDM, as well as the spectral profile of the excitation pulse (which is assumed to be Gaussian throughout this thesis). Following initial photoexcitation, which, we recall, is essentially instantaneous compared to nuclear motion, the individual wavefunctions will constructively interfere creating a localised vibrational envelope with high amplitude in the vFC region and near zero amplitude elsewhere on the PES. The time-dependancy of the above equation causes the position at which the constructive interference occurs to change. This results in the wavepacket "moving" as a coherent entity, oscillating on the PES as the position of interference moves. The motion of the wavepacket, within a harmonic potential at least, can be likened to that of a classical particle oscillating in a parabolic well.

---

xiiPlease note, from here on Δt will refer to the delay between the pump and probe pulses, however Δt is used here as the uncertainty in time purely for conformity with tradition.

1.4.3 Quantum Beating

As mentioned above, upon photoexcitation with a broadband laser pulse, a coherent, *time-dependent* wavepacket is created. If the wavepacket is composed of equally spaced vibrational wavefunctions, as in a quantum harmonic oscillator, the form of the superposition remains governed by the initially imposed shaping factor, A_n, and as a result will not change as it evolves in time - the harmonic frequencies will retain their phase relationships. This results in the wavepacket oscillating indefinitely, in the absence of the other relaxation mechanisms discussed above, with frequencies equal to the spacing between the vibrational levels.[7,65]

In more realistic systems, where the potential well is anharmonic, the evolution of the wavepacket will be subject to the phenomenon known as "dispersion". This causes the individual frequencies to become out-of-phase, causing the shape of the wavepacket to change as the system evolves in time, resulting in a loss of coherence. Given sufficient time (on the order of ps), a decoherent wavepacket can often return to being in-phase, provided there are no other relaxation pathways present, leading to so-called wavepacket revivals.[66–70]

Careful selection of probing methodologies allows for the extraction of this detailed vibrational information. For example, if the vibrational modes contained within the wavepacket bring about a significant geometry change, this will result in large changes to the FC window as a function of the molecular geometry, allowing one to preferentially ionise at different points of the PES. This is discussed in more detail in Chapters 4 and 5.

1.4.4 Quantum Tunnelling

Tunnelling is a purely quantum mechanical phenomenon (with no inherent classical analogue), where the "wave-like" nature of a particle facilitates passage through an energetic barrier which exceeds the particle's kinetic energy. This is a consequence of the fact that the wave-solutions to the Schrödinger equation must be continuous. This boundary condition means that the wavefunction decays exponentially within the classically forbidden region (*i.e.* where V < E) and, provided the barrier is finite, will therefore be non-zero after the barrier. Hence, the probability of a given particle's existence on the opposite side of a potential barrier is necessarily non-zero, and particles will appear in this region.[50]

As a particle approaches a potential barrier, it is described by a free particle wavefunction as described in Section 1.3. When it reaches the barrier, it must satisfy the Schrödinger equation of the form:[50]

$$\frac{-\hbar^2}{2m}\frac{d^2\psi(u)}{du^2} = (E - V(u))\psi(u) \tag{1.15}$$

which has the solution

$$\psi = A\,e^{(-\alpha x)} \tag{1.16}$$
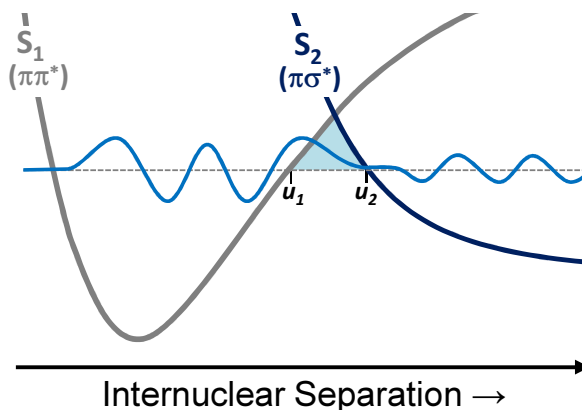
Figure 1.6: Quantum tunnelling of a wavefunction through a potential barrier $(u_1 - u_2)$ along an arbitrary internuclear coordinate. In the bound region of the S_1 PEC a normal anharmonic wavefunction is observed. The potential barrier, *i.e.* the classically forbidden region, causes the wavefunction to undergo an exponential decay before appearing on the S_2 state with a reduced amplitude.

where

$$\alpha = \sqrt{(2m(V(u) - E))/\hbar^2} \tag{1.17}$$

In this instance, A is a normalisation factor, α is the transmission coefficient, m is the mass of the particle, $V(u)$ is the potential barrier along the reaction coordinate, u, and E is the kinetic energy of the tunnelling particle. The transmission coefficient is used to describe the behaviour of a wave incident on a barrier. It represents the probability flux of the transmitted wave relative to that of the incident wave or, in this case, the particle's wavefunction.

In chemical terms, tunnelling can be more easily visualised utilising PECs. Figure 1.6 shows a schematic for tunnelling as applied to a dissociating molecule along the internuclear separation coordinate. Given the reactant molecule travels along the reaction coordinate, the molecule must overcome the potential energy barrier $(V(u) - E)$ in order to form atomic products. In the classical regime, if the molecule lacks the required energy to cross the barrier, dissociation would not be possible and the excited state population would remain in S_1. This would force the molecule to relax back to the ground state *via* an alternative mechanism such as fluorescence (*vide supra*). When treated quantum mechanically however, there is a finite probability that the molecule can tunnel straight through the barrier. As can be seen in the schematic, the amplitude of the wavefunction is decreased following the tunnelling process. It is important to note that this is indicative of the reduced *probability* of finding the particle, not a reduction in the particles energy (or frequency).

It is possible to approximate the tunnelling lifetime (and hence the tunnelling probability) along a 1D PEC using the semi-classical Wentzel-Kramers-Brillouin (WKB) method:[71]
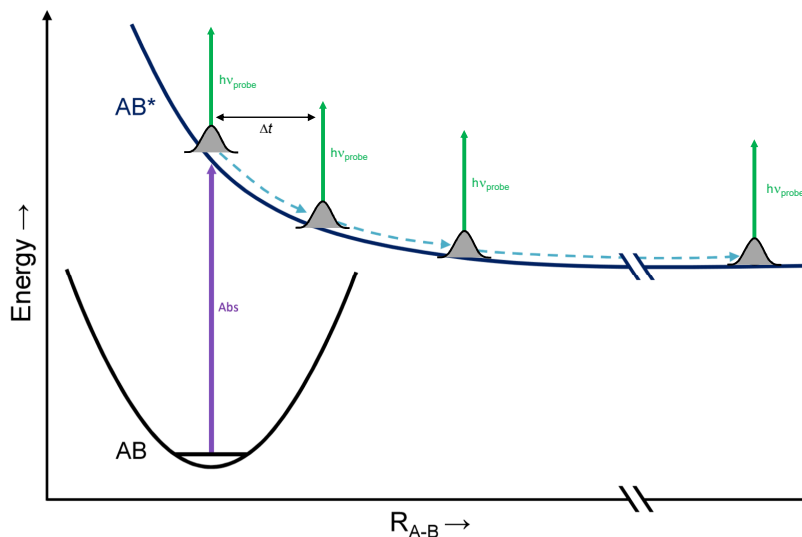
Figure 1.7: An adapted version of Figure 1.2 highlighting how changing Δt allows one to probe the temporal evolution of a wavepacket on the excited state surface.

$$\tau = \left[\nu_u \, exp \left(-2 \int_{u_1}^{u_2} \sqrt{\frac{2m}{\hbar^2} (V(u) - E)} \, du \right) \right]^{-1} \tag{1.18}$$

where ν_u is the frequency of the vibrational wavefunction. It can be seen from this equation that the tunnelling rate has an exponential dependancy on the mass of the particle and the "width" of the energy barrier. Hence, short lifetimes are only observed for small particles, *e.g.* hydrogen, tunnelling through small barriers. While the WKB method is a useful tool for shedding light on a simplistic molecular system (see Reference 59 for example), it is well known that in larger polyatomic systems the PES is multi-dimensional in nature, leading to the WKB approximation falling short when predicting the tunnelling lifetime.

H atom tunnelling has been recognised to play a fundamental role in a myriad of chemical[72] and biological processes,[73] particularly in enzyme activity, such as alcohol dehydrogenases[74] and Photosystem II.[75] In the latter species, the active mechanism is proposed to involve H tunnelling from the O–H bond of a phenol moiety. We will revisit tunnelling in Chapter 3 when discussing H atom elimination in the dihydroxybenzene species, resorcinol.

1.5   Pump-Probe Spectroscopy

Pump-probe spectroscopy has become a staple technique for investigating the excited state dynamics of molecular species in recent years, with a multitude of methods employing this relatively simple procedure.[7,16,76] In essence, a sample is first pumped (photo-excited) by a laser pulse, in order to initiate some kind of chemical or physical response, before being probed by a second laser pulse. The real power, and huge versatility, of pump-probe spectroscopy originates from the probe

step. Primarily, in this work, the probe step brings about ionisation of dissociated photoproducts yielding charged fragments which can be easily manipulated and detected.

The time-resolved variant of pump-probe spectroscopy is an incredibly powerful tool for probing and characterising the electronic and structural properties of very short-lived ($<$ ps) excited states. Simply by varying the time delay between the pump and probe pulses, Δt, the probe pulse is able to record a snapshot at various time delays and the temporal evolution of the excited state can be probed in real time. Figure 1.7 is an adapted version of Figure 1.2, this time showing the probe step as vertical green arrows. One can think of the probe step as an ultrafast stop motion camera, wherein a "picture" of the evolving wavepacket is recorded by projecting the population into a higher lying state (*e.g.* an ionic state) that is detectable in some way. There are a number of time-resolved techniques that allow for the detection of excited state evolution as well as a plethora of complementary methods that grant the ability to characterise excited state photoproducts with energy (frequency) resolution. What follows is a short introduction of multiphoton processes accompanied by a brief overview of several time-resolved probing techniques that are pertinent to the work presented in this thesis.

1.5.1   Multiphoton Processes and Resonance Enhanced Multiphoton Ionisation

Multiphoton Absorption

In Section 1.2.1 we discussed the process by which a molecular system is able to absorb a single photon in order to promote electrons from the relaxed ground state into some higher lying electronic state, governed by Equation 1.9. It is possible however for a system to absorb two (or more) photons in order to achieve electronic
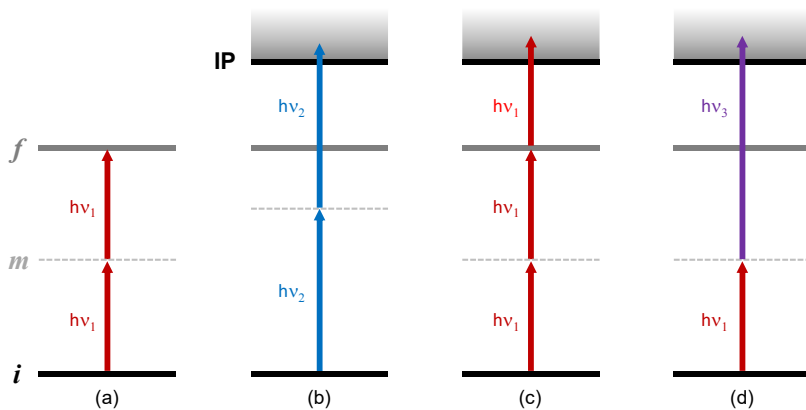
Figure 1.8: Pictorial representation of multiphoton processes. (a) A multiphoton excitation scheme proceeding through a virtual state (m). (b) [1+1] multiphoton ionisation through an intermediate state. (c) [2+1] REMPI scheme, this is the scheme used for H atom probing discussed in more detail below. (d) A [1+1'] multiphoton ionisation scheme using two different wavelengths of incident light.

excitation. Figure 1.8 (a) shows excitation to a higher lying state by a two-photon process, mediated by an intermediate '*virtual*' state. This virtual state is very short lived and so, for the process to be efficient, the absorption of the second photon must be (near) instantaneous. This requires high laser fluence in order to increase the probability of a successful transition. The probabilty (W) for a two photon event *via* an intermediate state is proportional to the square of the radiation intensity (I) as shown in the following equation:[77]

$$W \propto I^2 \left| \sum_m \frac{<f|\vec{\mu}|m><m|\vec{\mu}|i>}{\Delta E_{mf} - h\nu} \right|^2 \tag{1.19}$$

where i, m and f are the initial, virtual and final states respectively. ΔE_{mf} represents the energy difference between the intermediate state and the final state. The probability is a sum over m; this accounts for the spectral bandwidth of the absorbed photons by giving a range of accessible virtual levels. For an x photon process, the transition probability scales proportionally to I^x.

In an analogous process, it is possible for a system to be *ionised* following multiphoton absorption, as shown in Figure 1.8 (b). In this instance the system is excited, again *via* a virtual state, with enough energy to exceed the molecule's ionisation potential (IP), yielding parent cation and electron (or photoelectron) photofragments.

Resonance Enhanced Multiphoton Ionisation

The schematic in Figure 1.8 (c) shows a multiphoton ionisation scheme that proceeds through a higher lying electronic state before reaching the ionisation continuum. This mechanism is described as resonance enhanced multiphoton ionisation (REMPI) and is a common technique used in spectroscopy to explore vibronic transitions. By convention REMPI schemes are labelled $[i + j]$, where i represents the number of photons required to excite to the resonant higher lying state and j is the number of photons needed to ionise this state. Often excitation and ionisation photons are of different wavelengths; this being the case $[i + j']$ is used. With reference to the example given in Figure 1.8 (c), a $[2 + 1]$ REMPI scheme describes a two-photon excitation to a resonant excited state followed by single photon ionisation.

REMPI is a very powerful technique for elucidating transition energies for electronic and vibrational energy levels by virtue of the increased ionisation probability of the resonant electronic state compared to non-resonant ionisation. By scanning the excitation laser wavelength and plotting the change in parent ion (or photofragment) yield as a function of this wavelength one can acquire a spectrum of the transitions that are available within the system of interest. Spectra such as this are an immensely useful accompaniment when exploring the individual modes present in vibrational wavepackets and quantum beats such as those seen in Chapters 4 and 5.[78,79]

In the experiments performed in this thesis REMPI is employed as a highly selective probing method in order to spectroscopically monitor any photodissociated H atoms. A [2 + 1] REMPI scheme, using three 243 nm photons, is utilised to preferentially ionise H atoms through the two photon allowed $2s \leftarrow 1s$ transition.[xiii]

1.5.2 Femtosecond Probing

While REMPI (and other frequency resolved experiments) provides useful information regarding the electronic transitions in molecular systems, tracking the temporal evolution of the excited state requires other spectroscopic methods. The methodologies discussed below are based on the premise that we are primarily investigating systems wherein, following excitation, the molecule undergoes some dissociation process yielding photofragments (and, by virtue of the ionisation process, photoelectrons). By probing the kinetic energy and angular distribution of these photoproducts one can gain exquisite insight into the ultrafast dynamical processes that occur following UV excitation.

1.5.3 Time-resolved Photoelectron Spectroscopy

Photoelectron spectroscopy revolves around the detection of emitted electrons and has its roots in the photoelectric effect, discovered by Hertz in 1887[80] and later explained by Einstein.[81] The photoelectric effect is a simple phenomenon where an incident photon is able to cause the ejection of an electron from a system, provided the electron binding energy, eBE, is less than the photon energy, $h\nu$. The kinetic energy of the emitted electron, (eKE), can be measured and then eBE calculated, from the conservation of energy:[82]

$$h\nu = eBE + eKE \tag{1.20}$$

The equation shows that following absorption of a photon, and given eKE is known, it is possible to accurately calculate the eBE of any ejected electrons. Monitoring the evolution of eKE as a function of time allows for the accurate tracking of the excited state energies since each electronic eigenstate will have a distinct binding energy, giving insight into the flow of population following photoexcitation.[83,84]

This phenomenon can be utilised as an effective femtosecond probing technique since photoelectrons (being charged particles) are very easily detected through time of flight (TOF) or velocity map imaging (VMI) techniques (see below).[63,85–89] An additional advantage to using photoelectron spectroscopy stems from the fact that the selection rules that govern photodetachment are relaxed. In principle, this means any state can be probed given sufficient photon energy. This is particularly attractive for studying optically dark and non-fluorescent states.[63,90]

[xiii]The $2s \leftarrow 1s$ transition is also known as the Lyman-α transition.

1.5.4 Time-resolved Photofragment Spectroscopy

Time-resolved Ion Yield

In recent years, TOF mass spectrometry has been extensively used in order to detect charged fragments following photodissociation. In these experiments any ionised photofragments are accelerated into a drift tube, commonly replicating the set-up originally described by Wiley and McLaren.[91] This process imparts equal KE to each ion, however the ion's velocity along the flight tube is dependant on their mass to charge ratio (m/z) and as such the photofragments become separated, with lighter fragments arriving earlier at the detector[xiv].[91] This yields a mass spectrum which gives information regarding the types of photofragments released following excitation. By integrating the ion yield of a particular fragment (or, indeed, the entire mass spectrum) as a function of Δt one can acquire a time-resolved spectrum, or transient, which, when fit using the appropriate function(s) (see Appendix A), yields the appearance time of the photoproduct.

Similarly, it is possible to track the ion yield of the parent cation which will also be generated by the pump-probe process, the so-called time-resolved ion yield (TR-IY). In contrast to photofragments however (which will increase with time), the parent cation will decay over time (into the photoproducts). This, in essence, provides the lifetime of the initially prepared excited state. One caveat to parent cation TR-IY is that the decay time extracted from the transient is a measure of the collaborative effect of *all* available decay pathways, making it somewhat difficult to extract precise relaxation mechanisms from these measurements alone.

1.5.5 Time-resolved Velocity Map Imaging

VMI is an extremely powerful technique that has earned itself widespread use throughout the chemical physics community since its inception in the late 90's.[92,93] Eppink and Parker were the first to modify the already established Wiley-McLaren TOF spectrometer in order to map charged particles according to their translational velocity, irrespective of their position in space following the photodissociation event.[94] The vital step that sets VMI apart from similar TOF and imaging methods[95] is the use of ion optics, in the form of an Einzel lens, to focus charged particles with the same initial velocity vector onto the same point of a *position sensitive* detector. In simple terms, each ion with the same initial velocity is mapped onto the same pixel of the detector.

Following interaction with the photodissociation laser (the pump pulse) any dissociated fragments will recoil away from the focal point creating a so-called *Newton sphere*. The Newton sphere is focused by the ion optics onto the position sensitive

---

[xiv]For now it suffices to know that the detector, often a set of micro-channel plates, monitors the number of ions that reach it, more detailed information on the detector used in these experiments can be found in Section 2.3.3.

detector creating a two-dimensional (2D) image. In contrast to conventional TOF methods, where the KE information is extracted based on the arrival time of ions, the VMI technique is able to extract all information (kinetic energy and angular distributions) from the spatial appearance of the recorded image. The full three-dimensional (3D) image can be reconstructed using an appropriate mathematical treatment (Abel inversion or polar onion peeling (POP), for example, see Section 2.3.3), to determine the pixel radius at which ions with a specific speed appear.[96–98] As mentioned above, each pixel on the detector is correlated to ions with a specific translational velocity, and hence their KE, allowing for the accurate extraction of the photoproduct energy information contained within the original 3D distribution.

A major advantage to VMI (and other position sensitive methods) is the extraction of the photofragment angular distribution (θ) relative to the electric field vector, ε_{pu}, of the pump laser. This angular information provides insight into the states that are accessed following the initial excitation step by virtue of each state possessing a different dipole moment. There is further discussion regarding the angular distribution of photofragments in Section 2.3.3.

1.6 Photostability

We have briefly touched upon the subject of photostability in a number of the sections above, however, we now take time to explore the concept in more detail; investigating how the aforementioned fundamental theory and techniques allow us to study the intrinsic photostability of important biomolecular species.

We previously stated that UV radiation, when absorbed by biologically relevant molecules, can often be very detrimental to a system since the incident high energy photons can easily induce irreversible bond cleavage (*via* dissociative states) and photochemical reactions.[99] We also pointed out that these potentially harmful pathways can occur on the order of ns - ps,[1] with the molecule remaining in the excited state for the duration. Provided there is a sufficiently rapid non-radiative decay pathway available, the molecule will take the kinetically favoured route and be termed photostable since any excess energy will be efficiently funnelled from the reactive excited state as heat, leaving the molecule once again in its relaxed ground state.

These photoprotective mechanisms are particularly important for the biological species that comprise the essential building blocks of life. At a molecular level, the majority of organic life can be broken down into surprisingly few unique species (DNA/RNA bases, amino acids *etc.*). Given the fact that these molecules came to form such crucial biological species, they must possess some intrinsic photostability mechanism that allows for the efficient disposal of excess energy, or else life would not have been able to withstand the high flux of UV radiation that was incident on the Earth before the ozone layer was formed.

With that said, $\sim$4 billion years later photostability is still a highly relevant subject. On a sunny day the average exposure to high energy photons (< 310 nm)

is on the order of 10^{18} photons per second (given a fluence of $\sim$250 W/cm^2),[100] even with a fully formed UV filtering ozone layer, however, far less than 1% of absorbed UV photons actually results in the formation of photolesions (UV induced photochemistry within DNA). This means that photostable molecules continue to act as a highly efficient frontline defence against UV radiation exposure. Eumelanin, for example, the brown pigment copolymer found in human skin, is proposed to serve as the first bastion of protection against UV induced photodamage as a result of its photostability.[17,32–34,101] Beyond the search for understanding these photochemical/photophysical processes, any information pertaining to these mechanisms can be highly beneficial towards other research areas; sunscreen photoprotective properties,[102–104] photoactivated complexes for use in photodynamic therapy[105–107] and photovoltaics[108,109] as particularly relevant, modern examples.

1.6.1 $^1\pi\sigma^*$ states

We have already introduced dissociative states and photodissociation mechanisms, albeit briefly, in Section 1.2.4. Here, we explore in greater detail $^1\pi\sigma^*$ states and their role in the excited state dynamics of heteroaromatic biomolecules, and related UV chromophore subunits, focusing on phenol as a prototypical system.

The potential role of $^1\pi\sigma^*$ states in photostability mechanisms in biological systems was first recognised by Sobolewski *et al.* in their seminal theoretical work.[76,110–112] The authors postulated that $^1\pi\sigma^*$ states, which are dissociative with respect to some X–H bond (where X = O or N), offer a simple, non-radiative decay pathway from the excited state back to the ground state (S_0) by virtue of the $^1\pi\sigma^*/S_0$ CIs formed at extended X–H bond lengths (see Figure 1.9). The photoprotective mechanism put forth by the authors was such that, following population transfer to (or direct population of) the $^1\pi\sigma^*$ state, the lower $^1\pi\sigma^*/S_0$ CI can facilitate either (i) fast IC, yielding vibrationally hot molecules on the S_0 state or (ii) dissociation of the X–H bond to eliminate the H atom. Note that the latter case, despite a bond being broken (which we previously suggested could be harmful), can still provide a protective mechanism, as in a more realistic environment, such as in a DNA base pair,[76] the hydrogen can easily recombine after releasing excess energy thermally.

The relaxation mechanism described above is proposed to account for the low fluorescence quantum yields observed in many aromatic systems that possess protonated heteroatoms; for example azoles, pyrroles, phenols, indoles *etc.* which are chromophores of important biological species (see References 76 and 111 and references therein). Phenol, for instance, is the UV chromophore of the amino acid tyrosine. Tyrosine, as well as being a crucial amino acid, is suggested to play a key role in the active site of a number of enzymes, most notably Photosystem II, a known light-harvesting complex. As a result, the excited-state dynamics of phenol have received considerable interest in recent years from both theoretical[110,113–116] and experimental standpoints.[117–124]
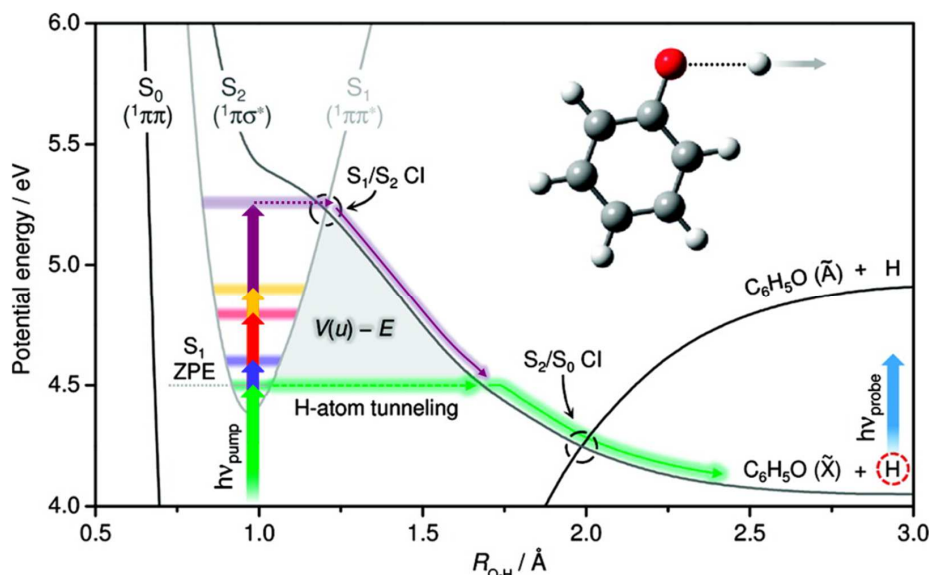
Figure 1.9: Calculated potential energy cuts along the O–H coordinate in phenol (molecular structure inset), for the first two electronic excited states, $^1\pi\pi^*$ and $^1\pi\sigma^*$, together with the S_0 ground state. These cuts are adapted from those calculated in Reference 123. The shaded gray area, labelled $V(u) - E$, represents the potential barrier through which tunnelling occurs.

The general electronic excited state landscape of phenol (at least along the O–H bond coordinate, $R_{O–H}$) is, by now, well described.[59,121,123] It is widely accepted that the first excited $^1\pi\pi^*$ state accounts for the first absorption onset in the UV absorption spectrum of most phenols (such as that shown in Figure 3.1 for resorcinol, see Chapter 3). The 'optically dark' $^1\pi\sigma^*$ state, which is dissociative with respect to $R_{O–H}$, lies above the $^1\pi\pi^*$ state in the vFC excitation region. It has been revealed, in accordance with Sobolewski *et al.*'s postulate,[110] that non-adiabatic interactions between the bright $^1\pi\pi^*$ state and dark $^1\pi\sigma^*$ state, play a major role in the excited state relaxation dynamics in phenol. At extended $R_{O–H}$ distances ($R_{O–H} \approx 2.0$ Å), the $^1\pi\pi^*$ state becomes degenerate with the $^1\pi\sigma^*$ state creating a $^1\pi\pi^*/^1\pi\sigma^*$ CI. At energies above this CI, population is transferred non-adiabatically from $^1\pi\pi^* \rightarrow {}^1\pi\sigma^*$ on an ultrafast timescale (purple arrows in Figure 1.9). Once on the $^1\pi\sigma^*$ state, further extension of the O–H bond leads to the lower lying $^1\pi\pi^*/S_0$ CI. Nonadiabatic coupling through this CI yields one of the two situations outlined above, (i) or (ii), with the latter resulting in the production of high KE H atoms in association with radical co-fragments - in the representative example here, phenoxyl radicals ($C_6H_5O^\bullet$).

Perhaps somewhat counter-intuitively, excitation below the $^1\pi\pi^*/^1\pi\sigma^*$ CI in phenol, and many (but not all) of its derivatives, still results in the formation of high KE H atoms. This is a signature for $^1\pi\sigma^*$ driven O–H scission, occurring on a longer timescale, despite the considerable barrier to dissociation ($\sim$4000 cm^{-1} in phenol). It is now the general understanding that these high KE H atoms are borne through non-adiabatic coupling from the $^1\pi\pi^*$ state onto the $^1\pi\sigma^*$ state mediated by H atom *tunnelling* beneath the $^1\pi\pi^*/^1\pi\sigma^*$ CI (green arrows in Figure 1.9).
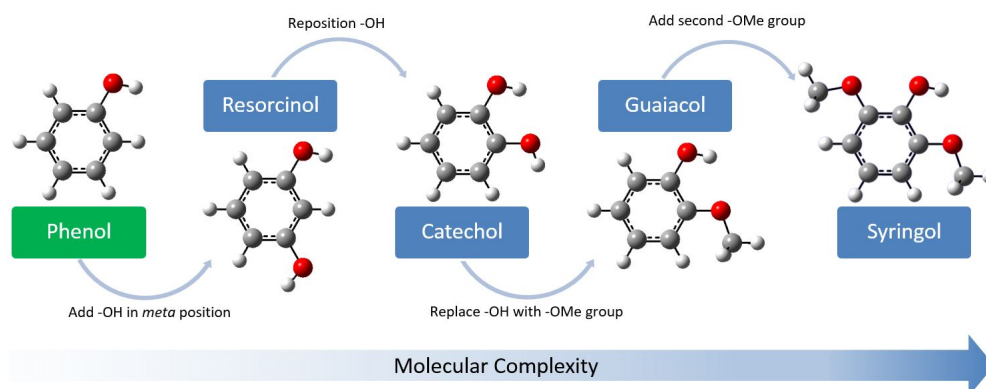
Figure 1.10: Schematic showing the structures of the species studied in this thesis. From left to right: phenol, resorcinol (1,3-dihydroxybenzene), catechol (1,2-dihydroxybenzene), guaiacol (2-methoxyphenol) and syringol (2,6-dimethoxyphenol). This also demonstrates our "bottom-up approach"; highlighting increasing molecular complexity as we proceed from phenol to syringol.

From their Rydberg tagging experiments, Ashfold and co-workers concluded the tunnelling process is mediated by a torsional motion of the phenyl ring, labelled the $\nu 16a$ mode in Wilson's notation,[125] although earlier theoretical treatments implied O–H torsion (τ_{OH}) should drive such behaviour.

Phenol provides an excellent basis for understanding the excited state landscapes of the species throughout this thesis; resorcinol, catechol, guaiacol and syringol are all phenol-like species whose excited states closely resemble that of the prototypical system. The structures of the above molecules are shown in Figure 1.10. Where appropriate, comparison will be made between the molecule under investigation and phenol.

1.7 Summary

In this chapter we have explored the fundamental principles of the experiments employed herein. We first took an in depth look at the possible relaxation pathways available to species that have been prepared in their excited state following absorption of a high energy UV photon. We then proceeded to explore the quantum mechanical theories that govern the excited state dynamics of these species and went onto a broad introduction to the experimental methods used to perform femtosecond pump-probe experiments, highlighting in particular the importance of the probe step. We closed out the chapter with a brief introduction to the real purpose of this thesis; exploring the excited state dynamics and photostability of biologically relevant molecules in the isolated gas phase with a focus on $^{1}\pi\sigma^{*}$ mediated relaxation.

Figure 1.10 shows the structures of the species investigated in the subsequent chapters, alongside the example system described above, phenol. Throughout the course of this thesis we hope to answer the following questions: how does modification of a molecule's structure affect the relaxation mechanisms exhibited by

phenolic species following photoexcitation *and* are we then able to relate the observed timescales to the intrinsic pohotostabilities of larger species which contain the biologically relevant chromophores under investigation?

Chapter 2 details the experimental set-up employed in order to investigate heteroaromatic species in the isolated gas phase. Now, with the experiment in mind, Chapter 3 explores the disubstituted benzene molecule, resorcinol (Figure 1.10). In this chapter we seek to investigate the effect that an additional functional group (*meta*- to the initial O–H) has on the excited state landscape, and hence dynamics, compared to phenol. This leads nicely into Chapter 4, which explores early-time vibrational wavepacket motion on the excited state of catechol, another dihydroxy-substituted benzene, where the additional hydroxy- group is now positioned *ortho*-to the first. While this seemingly simple rearrangement may not seem like a significant increase in molecular complexity, it is shown that the presence of an intramolecular hydrogen bond (formed between the two O–H groups) has a profound effect on the excited state relaxation dynamics. Finally, Chapter 5 extends the work done on catechol, investigating the effect of further functionalisation (the addition of one or two methoxy- groups) by monitoring the early time vibrational motions in guaiacol and syringol, two chromophore subunits of the important bio-polymer, lignin. Once again, it is shown that the presence of an intramolecular hydrogen bond between adjacent functional groups has a significant impact on the dynamics displayed by these closely related species.

References

1. Crespo-Hernandez, C. E., Cohen, B., Hare, P. M., and Kohler, B. *Chem. Rev.* **104**(4), 1977–2019 (2004).

2. Middleton, C. T., de La Harpe, K., Su, C., Law, Y. K., Crespo-Hernandez, C. E., and Kohler, B. *Annu. Rev. Phys. Chem.* **60**, 217–239 (2009).

3. Schreier, W. J., Schrader, T. E., Koller, F. O., Gilch, P., Crespo-Hernandez, C. E., Swaminathan, V. N., Carell, T., Zinth, W., and Kohler, B. *Science* **315**(5812), 625–629 (2007).

4. Pfeifer, G. P., You, Y. H., and Besaratinia, A. *Mutat. Res.-Fund. Mol. M.* **571**(1-2), 19–31 (2005).

5. Keller, U. *Nature* **424**(6950), 831–838 (2003).

6. Shank, C. V. and Ippen, E. P. *Appl. Phys. Lett.* **24**(8), 373–375 (1974).

7. Zewail, A. H. *Angew. Chem., Int. Edit.* **39**(15), 2587–2631 (2000).

8. Zewail, A. H. *J. Phys. Chem.* **100**(31), 12701–12724 (1996).

9. Dantus, M., Rosker, M. J., and Zewail, A. H. *J. Chem. Phys.* **89**(10), 6128–6140 (1988).

10. Rose, T. S., Rosker, M. J., and Zewail, A. H. *J. Chem. Phys.* **91**(12), 7415–7436 (1989).

11. Dantus, M., Bowman, R. M., Gruebele, M., and Zewail, A. H. *J. Chem. Phys.* **91**(12), 7437–7450 (1989).

12. Baumert, T., Herek, J. L., and Zewail, A. H. *J. Chem. Phys.* **99**(6), 4430–4440 (1993).

13. Herek, J. L., Pedersen, S., Banares, L., and Zewail, A. H. *J. Chem. Phys.* **97**(12), 9046–9061 (1992).

14. Janssen, M. H. M., Dantus, M., Guo, H., and Zewail, A. H. *Chem. Phys. Lett.* **214**(3-4), 281–289 (1993).

15. Pedersen, S., Baumert, T., and Zewail, A. H. *J. Phys. Chem.* **97**(48), 12460–12465 (1993).

16. Staniforth, M. and Stavros, V. G. *Proc. R. Soc. A* **469**(2159), 20130458 (2013).

17. Young, A. R. *Phys. Med. Biol.* **42**(5), 789–802 (1997).

18. Iqbal, A. and Stavros, V. G. *J. Chem. Phys. Lett* **1**(15), 2274–2278 (2010).

19. Belshaw, L., Calegari, F., Duffy, M. J., Trabattoni, A., Poletto, L., Nisoli, M., and Greenwood, J. B. *J. Chem. Phys. Lett* **3**(24), 3751–3754 (2012).

20. Kang, H., Jouvet, C., Dedonder-Lardeux, C., Martrenchard, S., Gregoire, G., Desfrancois, C., Schermann, J. P., Barat, M., and Fayeton, J. A. *Phys. Chem. Chem. Phys.* **7**(2), 394–398 (2005).

21. Kang, H., Dedonder-Lardeux, C., Jouvet, C., Gregoire, G., Desfrancois, C., Schermann, J. P., Barat, M., and Fayeton, J. A. *J. Phys. Chem. A* **109**(11), 2417–2420 (2005).

22. Nolting, D., Schultz, T., Hertel, I. V., and Weinkauf, R. *Phys. Chem. Chem. Phys.* **8**(44), 5247–5254 (2006).

23. Barbatti, M., Aquino, A. J. A., Szymczak, J. J., Nachtigallova, D., Hobza, P., and Lischka, H. *Proc. Natl. Acad. Sci. U. S. A.* **107**(50), 21453–21458 (2010).

24. Evans, N. L. and Ullrich, S. *J. Phys. Chem. A* **114**(42), 11225–11230 (2010).

25. Wells, K. L., Hadden, D. J., Nix, M. G. D., and Stavros, V. G. *J. Chem. Phys. Lett* **1**(6), 993–996 (2010).

26. Barbatti, M., Szymczak, J. J., Aquino, A. J. A., Nachtigallova, D., and Lischka, H. *J. Chem. Phys.* **134**(1), 014304 (2011).

27. Ullrich, S., Schultz, T., Zgierski, M. Z., and Stolow, A. *Phys. Chem. Chem. Phys.* **6**(10), 2796–2801 (2004).

28. Canuel, C., Mons, M., Piuzzi, F., Tardivel, B., Dimicoli, I., and Elhanine, M. *J. Chem. Phys.* **122**(7), 074316 (2005).

29. Chatterley, A. S., Johns, A. S., Stavros, V. G., and Verlet, J. R. R. *J. Phys. Chem. A* **117**(25), 5299–5305 (2013).

30. Chatterley, A. S., West, C. W., Roberts, G. M., Stavros, V. G., and Verlet, J. R. R. *J. Chem. Phys. Lett* **5**(5), 843–848 (2014).

31. Kang, H., Lee, K. T., Jung, B., Ko, Y. J., and Kim, S. K. *J. Am. Chem. Soc.* **124**(44), 12958–12959 (2002).

32. Meredith, P. and Riesz, J. *Photochem. Photobiol.* **79**(2), 211–216 (2004).

33. Meredith, P., Powell, B. J., Riesz, J., Nighswander-Rempel, S. P., Pederson, M. R., and Moore, E. G. *Soft Matter* **2**(1), 37–44 (2006).

34. Meredith, P. and Sarna, T. *Pigment Cell Res.* **19**(6), 572–594 (2006).

35. Huijser, A., Pezzella, A., Hannestad, J. K., Panzella, L., Napolitano, A., d'Ischia, M., and Sundstrom, V. *ChemPhysChem* **11**(11), 2424–2431 (2010).

36. Huijser, A., Pezzella, A., and Sundstrom, V. *Phys. Chem. Chem. Phys.* **13**(20), 9119–9127 (2011).

37. Kopas-lane, L. M. and Warthesen, J. J. *J. Food Sci.* **60**(4), 773–776 (1995).

38. Delgado-Vargas, F., Jimenez, A. R., and Paredes-Lopez, O. *Crit. Rev. Food Sci. Nutr.* **40**(3), 173–289 (2000).

39. Sundstrom, V. *Annu. Rev. Phys. Chem.* **59**, 53–77 (2008).

40. Hilborn, R. C. *Am. J. Phys.* **50**, 982 (1982).

41. Lakowicz, J. R. *Principles of Fluorescence Spectroscopy.* (2009).

42. Kinsey, J. L. *Annu. Rev. Phys. Chem.* **28**(1), 349–372 (1977).

43. Atkins, P. and de Paula, J. *Physical Chemistry, 8th Edition.* Oxford University Press, (2006).

44. Boyall, D. and Reid, K. L. *Chem. Soc. Rev.* **26**, 223–232 (1997).

45. Reid, K. L. *Int. Rev. Phys. Chem.* **27**(4), 607–628 (2008).

46. Fermi, E. *Nuclear Physics.* University of Chicago Press, (1950).

47. Stokes, G. G. *Phil. Trans. R. Soc. A* **142**, 463–562 (1852).

48. Beddard, G., Fleming, G., Gijzeman, O., and Porter, G. *Chem. Phys. Lett.* **18**(4), 481–487 (1973).

49. Englman, R. and Jortner, J. *Mol. Phys.* **18**(2), 145–164 (1970).

50. Atkins, P. and Friedman, R. *Molecular Quantum Mechanics: 5th Edition.* Oxford University Press, (2011).

51. Born, M. and Oppenheimer, R. *Annalen der Physik* **389**(20), 457–484 (1927).

52. Eckart, C. *Phys. Rev.* **46**(5), 383– (1934).

53. Hollas, J. M. *Modern Spectroscopy.* John Wiley & Sons, (2004).

54. Matsika, S. and Krause, P. *Annu. Rev. Phys. Chem.* **62**, 621–643 (2011).

55. Yarkony, D. R. *Rev. Mod. Phys.* **68**(4), 985–1013 (1996).

56. Hertel, I. V. and Radloff, W. *Reports on Progress in Physics* **69**(6), 1897 (2006).

57. Kuhlman, T. S., Sauer, S. P. A., Slling, T. I., and Mller, K. B. *The Journal of Chemical Physics* **137**(22) (2012).

58. Nix, M. G. D., Devine, A. L., Cronin, B., Dixon, R. N., and Ashfold, M. N. R. *J. Chem. Phys.* **125**(13), 133318 (2006).

59. Roberts, G. M., Chatterley, A. S., Young, J. D., and Stavros, V. G. *J. Chem. Phys. Lett* **3**(3), 348–352 (2012).

60. Manners, J. *Quantum physics: an introduction.* CRC Press, (2000).

61. Heisenberg, W. *Zeitschrift fur Physik* **43**(3-4), 172–198 (1927).

62. Robertson, H. P. *Phys. Rev.* **34**(1), 163–164 July (1929).

63. Wu, G., Hockett, P., and Stolow, A. *Phys. Chem. Chem. Phys.* **13**(41), 18447–18467 (2011).

64. Heller, E. J. *J. Chem. Phys.* **62**(4), 1544–1555 (1975).

65. Kobayashi, T. and Kida, Y. *Phys. Chem. Chem. Phys.* **14**(18), 6200–6210 (2012).

66. Farmanara, P., Ritze, H.-H., Stert, V., and Radloff, W. *Chem. Phys. Lett.* **307**(12), 1 – 7 (1999).

67. Vrakking, M. J. J., Villeneuve, D. M., and Stolow, A. *Phys. Rev. A* **54**, R37–R40 Jul (1996).

68. Fischer, I., Vrakking, M. J. J., Villeneuve, D. M., and Stolow, A. *Chem. Phys.* **207**(2-3), 331–354 (1996).

69. Verlet, J. R. R., Stavros, V. G., Minns, R. S., and Fielding, H. H. *J. Phys. B-At. Mol. Opt.* **36**(17) (2003).

70. Wals, J., Fielding, H. H., Christian, J. F., Snoek, L. C., Van Der Zande, W. J., and Van Linden Van Den Heuvell, H. B. *Phys. Rev. Lett.* **72**, 3783–3786 Jun (1994).

71. LeRoy, R. J. and Liu, W. K. *J. Chem. Phys.* **69**(8), 3622–3631 (1978).

72. Bell, R. P. *The tunnel effect in chemistry.* Springer, (2013).

73. Kohen, A. and Klinman, J. P. *Chemistry & Biology* **6**(7), R191–R198 (1999).

74. Kohen, A., Cannio, R., Bartolucci, S., and Klinman, J. P. *Nature* **399**(6735), 496–499 (1999).

75. Reece, S. Y., Hodgkiss, J. M., Stubbe, J., and Nocera, D. G. *Phil. Trans. R. Soc. B* **361**(1472), 1351–1364 (2006).

76. Roberts, G. M. and Stavros, V. G. *Chem. Sci.* **5**(5), 1698–1722 (2014).

77. Lin, S. H., Fujimura, Y., Neusser, H. J., and Schlag, E. W. *Multiphoton spectroscopy of molecules.* Elsevier, (2012).

78. Dean, J. C., Navotnaya, P., Parobek, A. P., Clayton, R. M., and Zwier, T. S. *J. Chem. Phys.* **139**(14), 144313 (2013).

79. King, G. A., Oliver, T. A. A., Dixon, R. N., and Ashfold, M. N. R. *Phys. Chem. Chem. Phys.* **14**(10), 3338–3345 (2012).

80. Hertz, H. *Annalen der Physik* **267**(8), 983–1000 (1887).

81. Einstein, A. *Annalen der Physik* **4**, – (1905).

82. Stolow, A., Bragg, A. E., and Neumark, D. M. *Chem. Rev.* **104**(4), 1719–1757 (2004).

83. Seel, M. and Domcke, W. *Chem. Phys.* **151**(1), 59–72 (1991).

84. Seel, M. and Domcke, W. *J. Chem. Phys.* **95**(11), 7806–7822 (1991).

85. Moore, J. H., Davis, C. C., Coplan, M. A., and Greer, S. C. *Building scientific apparatus.* Cambridge University Press, (2009).

86. Neumark, D. M. *Annu. Rev. Phys. Chem.* **52**(1), 255–277 (2001).

87. Stolow, A. *Faraday Discuss.* **163**, 9–32 (2013).

88. Suzuki, T. *Annu. Rev. Phys. Chem.* **57**, 555–592 (2006).

89. Verlet, J. R. R. *Chem. Soc. Rev.* **37**(3), 505–517 (2008).

90. Blanchet, V., Zgierski, M. Z., Seideman, T., and Stolow, A. *Nature* **401**(6748), 52–54 (1999).

91. Wiley, W. and McLaren, I. H. *Rev. Sci. Instrum.* **26**(12), 1150–1157 (1955).

92. Vallance, C. *Phil. Trans. R. Soc. A* **362**(1825), 2591–2609 (2004).

93. Ashfold, M. N. R., Nahler, N. H., Orr-Ewing, A. J., Vieuxmaire, O. P. J., Toomes, R. L., Kitsopoulos, T. N., Garcia, I. A., Chestakov, D. A., Wu, S. M., and Parker, D. H. *Phys. Chem. Chem. Phys.* **8**(1), 26–53 (2006).

94. Eppink, A. T. J. B. and Parker, D. H. *Rev. Sci. Instrum.* **68**(9), 3477–3484 (1997).

95. Chandler, D. W. and Houston, P. L. *J. Chem. Phys.* **87**(2), 1445–1447 (1987).

96. Eppink, A. T. J. B., Wu, S. M., and Whitaker, B. J. *Imaging in molecular dynamics: technology and applications.* Cambridge university press, (2003).

97. Garcia, G. A., Nahon, L., and Powis, I. *Rev. Sci. Instrum.* **75**(11), 4989–4996 (2004).

98. Roberts, G. M., Nixon, J. L., Lecointre, J., Wrede, E., and Verlet, J. R. R. *Rev. Sci. Instrum.* **80**(5), 053104 (2009).

99. Domcke, W. *Phys. Chem. Chem. Phys.* **12**, 4897–4898 (2010).

100. Webb, A. R. and Steven, M. D. *Quarterly Journal of the Royal Meteorological Society* **113**(475), 393–400 (1987).

101. Sobolewski, A. L. and Domcke, W. *ChemPhysChem* **8**(5), 756–762 (2007).

102. Baker, L. A., Horbury, M. D., Greenough, S. E., Coulter, P. M., Karsili, T. N., Roberts, G. M., Orr-Ewing, A. J., Ashfold, M. N., and Stavros, V. G. *J Phys. Chem. Lett.* **6**(8), 1363–1368 (2015).

103. Baker, L. A., Horbury, M. D., Greenough, S. E., Ashfold, M. N., and Stavros, V. G. *Photochem. Photobiol. Sci.* **14**(10), 1814–1820 (2015).

104. Stavros, V. G. *Nat. Chem.* **6**(11), 955–956 (2014).

105. Zhao, Y., Roberts, G. M., Greenough, S. E., Farrer, N. J., Paterson, M. J., Powell, W. H., Stavros, V. G., and Sadler, P. J. *Angewandte Chemie* **124**(45), 11425–11428 (2012).

106. Dougherty, T. J., Gomer, C. J., Henderson, B. W., Jori, G., Kessel, D., Korbelik, M., Moan, J., and Peng, Q. *J. Natl. Cancer Inst.* **90**(12), 889–905 (1998).

107. Dolmans, D. E., Fukumura, D., and Jain, R. K. *Nat. Rev. Cancer* **3**(5), 380–387 (2003).

108. De Brito, M. A., Sampaio, L. P., Junior, L. G., and Canesin, C. In *Power Electronics Conference (COBEP)*, 531–537. IEEE, (2011).

109. Kazmerski, L. L. *Renew. Sust. Energ. Rev.* **1**(1), 71–170 (1997).

110. Sobolewski, A. L., Domcke, W., Dedonder-Lardeux, C., and Jouvet, C. *Phys. Chem. Chem. Phys.* **4**(7), 1093–1100 (2002).

111. Ashfold, M. N. R., Cronin, B., Devine, A. L., Dixon, R. N., and Nix, M. G. D. *Science* **312**(5780), 1637–1640 (2006).

112. Ashfold, M. N. R., King, G. A., Murdock, D., Nix, M. G. D., Oliver, T. A. A., and Sage, A. G. *Phys. Chem. Chem. Phys.* **12**(6), 1218–1238 (2010).

113. Sobolewski, A. L. and Domcke, W. *J. Phys. Chem. A* **105**(40), 9275–9283 (2001).

114. Lan, Z. G., Domcke, W., Vallet, V., Sobolewski, A. L., and Mahapatra, S. *J. Chem. Phys.* **122**(22), 224315 (2005).

115. Abe, M., Ohtsuki, Y., Fujimura, Y., Lan, Z., and Domcke, W. *J. Chem. Phys.* **124**(22), 224316 (2006).

116. Nix, M. G. D., Devine, A. L., Dixon, R. N., and Ashfold, M. N. R. *Chem. Phys. Lett.* **463**(4-6), 305–308 (2008).

117. Tseng, C. M., Lee, Y. T., and Ni, C. K. *J. Chem. Phys.* **121**(6), 2459–2461 (2004).

118. Tseng, C.-M., Lee, Y. T., Lin, M.-F., Ni, C.-K., Liu, S.-Y., Lee, Y.-P., Xu, Z. F., and Lin, M. C. *J. Phys. Chem. A* **111**(38), 9463–9470 (2007).

119. Iqbal, A., Pegg, L.-J., and Stavros, V. G. *J. Phys. Chem. A* **112**(39), 9531–9534 (2008).

120. Iqbal, A., Cheung, M. S. Y., Nix, M. G. D., and Stavros, V. G. *J. Phys. Chem. A* **113**(29), 8157–8163 (2009).

121. Ashfold, M. N. R., Devine, A. L., Dixon, R. N., King, G. A., Nix, M. G. D., and Oliver, T. A. A. *Proc. Natl. Acad. Sci. U. S. A.* **105**(35), 12701–12706 (2008).

122. Hause, M. L., Yoon, Y. H., Case, A. S., and Crim, F. F. *J. Chem. Phys.* **128**(10), 104307 (2008).

123. Dixon, R. N., Oliver, T. A. A., and Ashfold, M. N. R. *J. Chem. Phys.* **134**(19), 194303 (2011).

124. Livingstone, R. A., Thompson, J. O. F., Iljina, M., Donaldson, R. J., Sussman, B. J., Paterson, M. J., and Townsend, D. *J. Chem. Phys.* **137**(18), 184304 (2012).

125. Wilson, E. B. *Phys. Rev.* **45**, 706–714 May (1934).

34

Chapter 2

Experimental

2.1   Introduction

In the following chapter the experimental set-up that was utilised for acquiring the reported results is described in detail. The experiment can be separated into two sections. The first explores the details of the femtosecond laser source, focusing in particular on how the Ti:sapphire oscillator and regenerative amplifier operate. We then explore the pump and probe lasers and their generation through the use of non-linear optical effects, such as sum frequency generation and optical parametric amplification. The latter half of the chapter describes the vacuum chamber and the components contained therein: the molecular beam and pulsed solenoid valve used to create it; the ion optic set up; and a summary of the time-of-flight and velocity map imaging spectrometer and calibration.

It should be noted from the outset that in this section we are primarily exploring the fundamental operation behind each step in the experimental process. Specific experimental details for each investigation are outlined within the appropriate chapter and a more in depth description of the chamber design is available in the thesis of Dr Adam Chatterley.[1]

2.2   Femtosecond Laser System

2.2.1   Summary

Figure 2.1 shows a schematic of the optical table that houses the laser system. Femtosecond pulses are derived from a commercially available Ti:sapphire ($Ti:Al_2O_3$) oscillator and regenerative amplifier system (Spectra-Physics; Tsunami and Spitfire XP, respectively).[2] The Ti:sapphire oscillator, pumped by a 5 W frequency-doubled continuous wave $Nd:YVO_4$ laser (Spectra-Physics, Millenia), produces a pulse train consisting of < 100 fs pulses, ~4 nJ/pulse, at a repetition rate of 75 MHz. The wavelength is centered at 800 nm and has a bandwidth (full width at half maximum
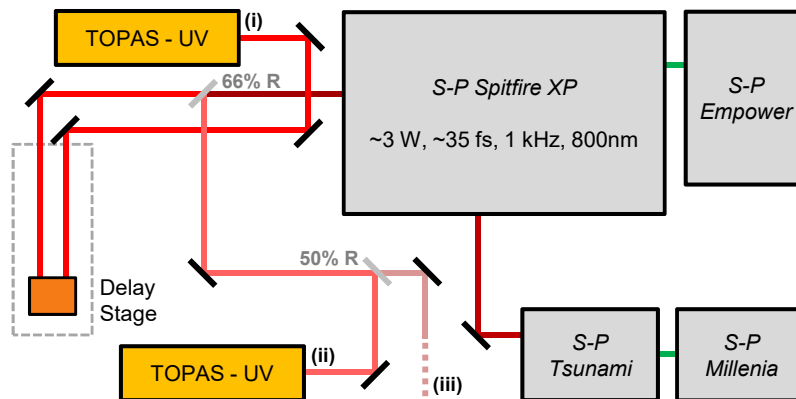
Figure 2.1: Schematic of the laser table containing the laser system and two OPAs.
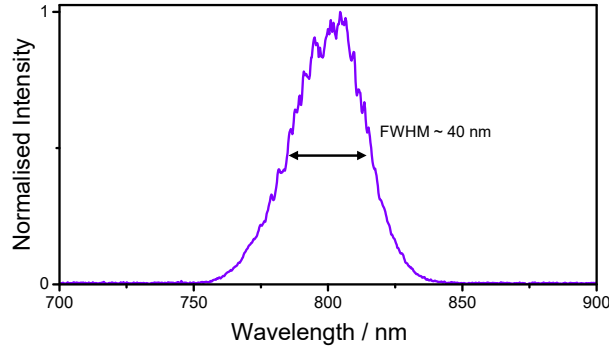
Figure 2.2: Spectrum of the output from the Tsunami Ti:sapphire oscillator. The pulse is Gaussian in shape centred at 800 nm with a FWHM of ∼40 nm.

- FWHM) of ∼40 nm, as shown in Figure 2.2.

The regenerative amplifier takes the output from the oscillator and selects pulses at a 1 kHz repetition rate. These "seed" pulses are first temporally expanded using a diffraction grating, creating pulses on the order of picoseconds, before being amplified in a second Ti:sapphire cavity which is pumped by a pulsed ∼15 W Nd:YLF laser (Spectra-Physics, Empower). The amplified pulses are switched out by a high voltage Pockels cell and recompressed by a second grating. This yields our fundamental 800 nm beam, operating at a 1 kHz repetition rate, with pulse energies of 3 mJ/pulse or a power of 3 W. Each laser pulse has a Gaussian pulse envelope with a duration of ∼35 fs.

The 3 W fundamental is then divided into three equal parts. Firstly, it is passed through a 66% reflective dichroic mirror yielding a 1 mJ transmitted beam (labelled (i) in Figure 2.1) and a 2 mJ reflected beam. The reflected portion is then sent through a 50% partially reflective optic, splitting the 2 mJ beam into two equal 1 mJ beams (labelled (ii) and (iii)). The first portion (i) is directed onto the motorised delay stage (Physik Instrumente), which creates a maximum temporal delay (Δt) of 1.2 ns between the pump and probe pulses, before pumping an optical parametric amplifier (Light Conversion, TOPAS-C). The second portion (ii) pumps another TOPAS-C, and the third (iii) is used in a separate setup (not discussed in the present thesis).[3]

What follows is a more in depth discussion of how the ultrafast laser pulses utilised throughout this thesis are generated.

2.2.2 Generation of Femtosecond Pulses

2.2.3 Ti:sapphire Oscillator

Generally, the construction of a fs oscillator is straight forward and consists of the same elements as any laser: a resonator cavity with (partially) reflecting end mirrors and a gain medium, in this instance Ti:sapphire. The key difference in comparison with continuous wave (cw) lasers or long pulsed lasers is (aside from the lasing media) the presence of a dispersive element (*i.e.* a pair of prisms or

chirped mirrors) in the cavity to control the spectral dispersion (see Section 2.2.4). This element allows one to compensate for the dispersion introduced by the gain medium and other optical components.

Typically, an oscillator is pumped by a cw laser. The pumping beam is focused into the active medium, ensuring that the beam is collinear with the cavity mode, in order to produce light *via* stimulated emission (see Section 1.2.2). The output radiation field is then the sum over all fields in the oscillating modes. Importantly, if there is no constant phase relation between the modes, the intensity of the output radiation fluctuates randomly as a function of time without any regular structure (see Figure 2.3 (b)). *Mode-locking*, see below, locks all longitudinal modes in phase with each other and the subsequent constructive interference between the phase-locked modes generates pulses which oscillate within the cavity. Each time the newly generated pulse reflects from the partly transmitting cavity mirror, a fs pulse leaves the cavity.

Mode locking

The term mode-locking originates from a description of phase matching in the frequency domain: a short pulse can be formed within the laser resonator only when a fixed phase relationship is achieved between the longitudinal modes present
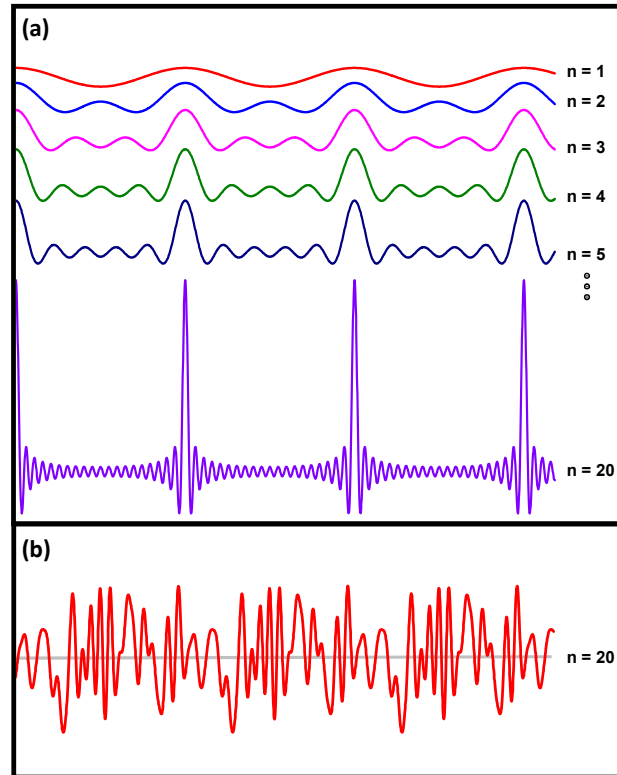
Figure 2.3: (a) Demonstration of how a coherent, or mode locked, sum of cosine waves results in localised regions of high amplitude. Each curve is a sum of the n in-phase harmonics of a cosine wave; as n increases, the sum tends towards a train of localised pulses. (b) Example of a mismatched phase relationship between the n cosine waves.

within the cavity. However, the basic mechanism that leads to mode-locking can more easily understood with reference to the time domain.

It is reasonably simple to visualise the process by consideration of a periodic pulse train formed from the superposition of multiple sinusoidal oscillations. Figure 2.3 (a) shows a series of summations of cosine waves, of the form:

$$f(x) = \sum_{k=1}^{n} \cos(kx + \phi) \tag{2.1}$$

for $1 \leq n \leq 20$ (only $n = 1-5$ and $n = 20$ are plotted for clarity), where ϕ represents the phase. As $f(x)$ tends to higher values of n it is clear that the constructive interference leads to the formation of a train of short pulses. An important aspect is that there *must* be a fixed phase relationship between these modes. This is illustrated by Figure 2.3 (b): the red curve shows the same 20 components as in (a) but this time ϕ for each wave is assigned a random value, leading to a mismatched phase relationship, and hence no constructive interference.

2.2.4   Ti:sapphire Amplifier

As mentioned previously, typical values of the pulse energy delivered by the Ti:sapphire oscillator are on the order of 4 nJ. Amplification of these pulses, to increase their pulse energy into the mJ regime, is extremely difficult owing to the high peak power, which would cause irreparable damage to any gain medium. It is possible to get around this problem, however, by stretching the pulse in time by a factor of $\sim 10^4$ (creating pulses on the order of picoseconds). The pulses, now with significantly lower peak powers, can then be safely amplified by the gain medium. Following amplification the pulses can be recompressed in order to return to the initial pulse duration (femtoseconds). These concepts are briefly outlined in the following sections.

Group Velocity Dispersion

Group velocity dispersion (GVD) describes how different frequency components of light propagate though a dispersive medium, *i.e.* short wavelengths versus long wavelengths. This is due to the wavelength-dependent refractive index of dispersive materials. GVD causes variation in the *temporal* profile of the laser pulse, while the frequency spectrum remains unaltered. It is said that the initial short pulse will become positively chirped (or upchirped) after propagating through a medium with "normal" dispersion (*e.g.* silica glass). This corresponds to the situation when higher frequencies travel slower than lower frequencies (blue slower than red). The opposite situation, where the pulse travels through a medium with "anomalous" dispersion, leads to a negative chirp (or downchirp). Here the higher frequencies propagate faster than the lower frequencies. The majority of optics utilised in ultrafast spectroscopy will contribute some amount of chirp to the initially generated
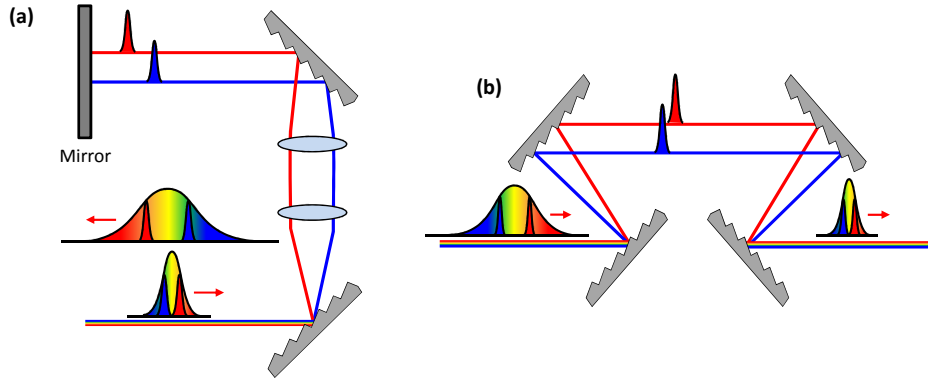
Figure 2.4: Schematic showing the general operation of (a) the stretcher (b) the compression stage. The stretcher setup extends the temporal duration of the laser pulse (lowering the peak power), whereas the grating arrangement in the compressor will compress the time duration of the pulse (increasing peak power).

fs pulse. It is the often the case now that an extra compression stage is included before the laser enters any interaction chamber in order to counteract any dispersion effects.

Stretcher-Compressor

By using dispersive optics (combination of gratings or prisms), the individual frequencies within a fs pulse can be separated from each other with respect to time (see Figure 2.4 (a)) prior to amplification. This technique is known as *chirped pulse amplification* (CPA). The duration of the incoming fs pulse is stretched (chirped) up to 10^4 times (fs $\rightarrow$ ps) in order to reduce the pulse peak intensity. The pulse is now ready to be amplified, since its amplification gain is lower than the damage threshold of the Ti:sapphire crystal. After amplification the pulse is recompressed to its original duration by a conjugate dispersion line (with opposite GVD). The recompression stage takes place in the compressor (see Figure 2.4 (b)). The main problem the compressor has to deal with is that it must recover not only the duration and quality of the initial pulse, but it has to compensate the dispersion introduced by the amplification stage itself. To overcome this problem, the distance between gratings in the compressor has to be larger than in the stretcher. This will cancel overall second-order dispersion and help in producing relatively short pulses, but also introduces higher-order dispersion terms, which will reflect in pre-pulses and/or wings.

Regenerative Amplification

The regenerative amplification technique involves trapping of the pulse to be amplified in a laser cavity, see Figure 2.5. Here, unlike multipass amplification, the number of passes is not important, the pulse remains in the resonator until all the energy stored in the amplification crystal is transferred to the input pulse. Trapping and dumping the pulse in and out of the resonator is done using a Pockels
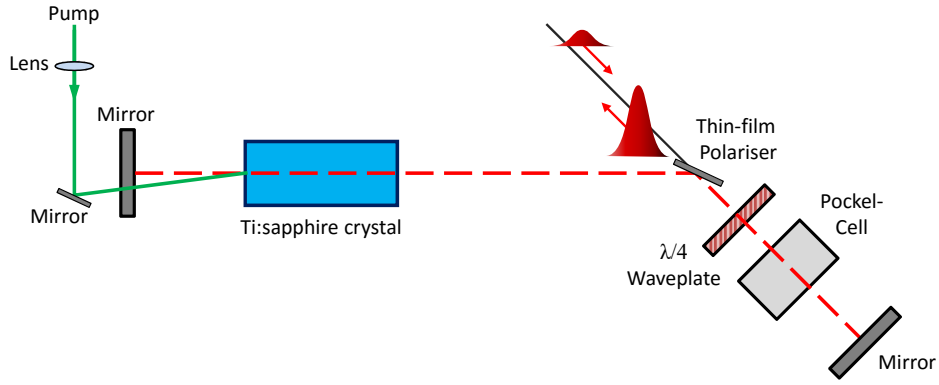
Figure 2.5: Schematic of the regenerative amplifier showing the Pockels cell and the Ti:sapphire gain medium.

cell and a broadband polariser. The Pockels cell consists of a birefringent crystal, that can change the polarisation of a travelling laser field following application of a high voltage. In the regenerative amplifier the Pockels cell is initially working like a quarterwave ($\lambda/4$) plate. When the pulse is sent to the resonator, the voltage on the Pockels cell is switched on and becomes the equivalent of a halfwave ($\lambda/4$) plate. In this way the pulse is kept in the cavity until it reaches saturation. Then a second voltage is applied and the now amplified pulse (~ 3 mJ) is extracted from the resonator.

2.2.5 Frequency Conversion

The energy required to excite a population to the first excited state in heteroaromatic systems, *i.e.* $\pi^* \leftarrow \pi$, is typically in the near-UV region, < 340 nm. As a result frequency up-conversion of the fundamental 800 nm beam to shorter wavelengths (higher energy) is required. Generation of femtosecond laser pulses in the near UV region relies on the use of non-linear optical effects; sum frequency generation (SFG), including second-harmonic generation (SHG), or optical parametric generation (OPG). These non-linear processes are achieved using a combination of non-centrosymmetric media, namely β-Barium Borate (BBO) crystals, and an optical parametric amplifier (OPA).

Nonlinear Optical Transformations

When an electromagnetic wave is incident on a transparent material, the electric field component of the wave causes the particles to be displaced. As we mentioned previously the relative displacement of charges within a system creates a dipole moment. The dipole moment per unit volume describes the polarisation, P, of the medium. In a linear material we can write:

$$P = \varepsilon_0 \chi E \tag{2.2}$$

where ε_0 is the permittivity of free space, χ is the linear susceptibility and E is
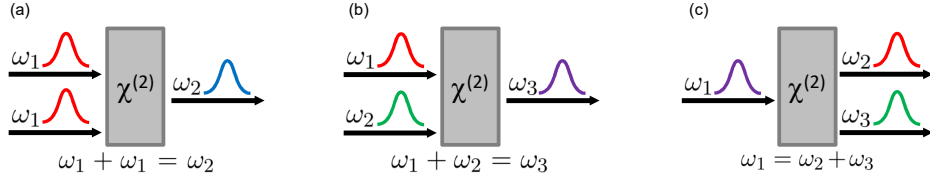
Figure 2.6: Schematic highlighting the various non-linear processes utilised in the generation of the different wavelengths employed as pump and probe pulses throughout this thesis. (a) SHG, (b) SFG and (c) OPG.

the electric field. This is a simplification, however, that only holds at low field strengths. When the magnitude of the electric field is large, as is the case when discussing high intensity pulsed lasers, the induced polarisation can be expressed as a power series with respect to the electric field:[4,5]

$$P = \varepsilon_0 \left(\chi^1 E^1 + \chi^2 E^2 + ... \chi^n E^n \right) = \left(P^1 + P^2 + ... P^n \right) \tag{2.3}$$

where χ^n is the nth order susceptibility and P^n is the nth order polarization. In the above equation, the optical processes pertinent to this thesis may be demonstrated by considering a simple electric field of the form:

$$E \propto \cos(\omega t) \tag{2.4}$$

with each of the E^n terms containing different frequency components of the electric field.

Sum Frequency Generation

In order to explore what the above means for the photons incident on transparent media, let us consider second-harmonic generation (SHG), the schematic of which is shown in Figure 2.6 (a). Given Equation 2.2 and the above proportionality, in a linear material P is proportional to $\cos(\omega t)$. It follows then that, interaction with an electromagnetic wave causes charges within the medium to oscillate with angular frequency ω and produce electromagnetic waves with the same angular frequency, ω.[6–8]

In nonlinear materials, which have non-zero second-order susceptibilities χ^2, P also contains non-negligible terms that are proportional to E^2. Thus, P^2 is proportional to $\cos^2(\omega t) = \left(\dfrac{1}{2} \right) (1 + \cos(2\omega t))$. Hence for the electric field E oscillating with frequency ω, the molecules in the media oscillate at the second harmonic, 2ω. More simply, the medium is able to radiate photons that are twice the frequency of the incident light, effectively producing a photon that is the summation of two incident photons, *i.e.* $\omega_1 + \omega_1 = \omega_2$. SHG is a subset of SFG which can be more broadly expressed as $\omega_1 + \omega_2 = \omega_3$ (Figure 2.6 (b)).[9] These non-linear processes are easily demonstrated with reference to the schematic shown in Figure 2.6.

In the experiments described in the subsequent chapters, SHG and SFG are

employed to generate photons at 200 nm, by utilising a series of three BBO crystals. First, SHG of the fundamental yields 400 nm light. The generated 400 nm beam is then combined with the residual fundamental 800 nm beam to give 267 nm (SFG yielding the third harmonic). Finally SFG between the 267 nm beam and the residual 800 nm photon gives the fourth harmonic, at 200 nm. Given the current experimental setup it is possible to use the 200 nm beam as either the pump or the probe step, however, in the example studies herein, the 200 nm beam is only used to pump HBr/MeOH for calibration of the VMI detector, see Section 2.3.4.

Optical Parametric Generation

OPG can be thought of as the opposite of SFG and is often utilised as a tunable method for frequency conversion. OPG employs non-centrosymmetric crystals (BBOs) similar to the SHG/SFG processes outlined above, however in place of producing one photon from two incident photons; two photons are produced from one incident photon.[8] The sum of the resulting photon's frequencies then equals the frequency of the initial photon, *i.e.* $\omega_1 = \omega_2 + \omega_3$. A representation of this process is shown in Figure 2.6 (c). As one might expect, the output beams can take a huge selection of frequencies, provided that the above summation is adhered to, *i.e.* energy is conserved. This means that some degree of control is required to produce beams of a specific wavelength.[i] Selection of specific values for $\omega_2 + \omega_3$ can be achieved through the use of a second incident photon ω_2 which induces stimulated emission at this frequency, this process is known as optical parametric amplification (the ω_2 output is amplified by ω_1). In our set-up, OPA is performed by the TOPAS-C amplifier.

Operation of the TOPAS-C uses a combination of the non-linear processes outlined above in order to produce a highly tunable output that can range from IR all the way through to UV. Firstly, a white light continuum[ii] is created by focussing a small portion of the 800 nm fundamental into a sapphire plate. A portion of this white light continuum is then amplified through OPG, utilising the remaining fundamental as the pump. This gives two tunable outputs, known as the signal and the idler, (perpendicularly polarised relative to the laser table), in the near IR region (1150 – 2600 nm). Subsequent SFG or SHG (with 800 nm) of this IR beam allows for generation of wavelengths from ~235 nm to 2600 nm. The power output from the OPA varies greatly with wavelength; typical values are on the order of μJs for the wavelengths utilised in the subsequent experiments.

---

[i]This becomes particularly relevant when we wish to pump specific regions of a molecule's excited state.

[ii]The generation of a white light continuum is another non-linear process that relies on high photon densities to induce spectral broadening of fs pulses through higher order non-linear effects.
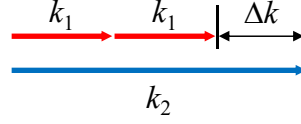
Figure 2.7: Diagrammatic representation of phase mismatch for SHG. The closer Δk is to zero, the more efficient the non-linear process.

Type I collinear   Type II collinear
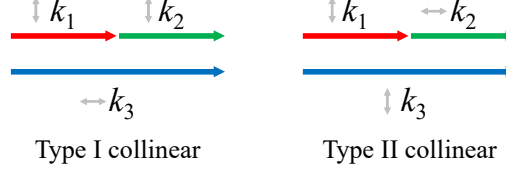
Figure 2.8: The two common phase matching schemes utilised in this thesis.

Phase Matching

An important consideration that has been neglected thus far is the necessity for *phase matching*. In order for the above non-linear optical effects to be efficient there must be a proper phase relationship between the interacting waves (input and output) along the propagation direction, that endures for the entirety of the non-linear process. In other words, any phase *mismatch* should be close to zero in order to obtain an effective non-linear interaction. For example, for phase matching of SHG, the mismatch (Δk) is given by the following:

$$\Delta k = k_2 - 2k_1 \tag{2.5}$$

where k_1 and k_2 are the wavenumbers of the fundamental and second-harmonic beam, respectively. The smaller the value of Δk in an optical process, the more efficient that process will be. Experimentally this is crucial for producing intense, good quality, stable beams. The OPA produces tunable outputs by phase matching different parts of a white light continuum with an amplification beam.

Phase matching can be achieved in many different ways. The usual technique for achieving phase matching in non-linear crystals is birefringent phase matching, where one exploits birefringence (*e.g.* BBO crystals) to counteract the phase mismatch. This technique comes in many variations, however the two types used in this thesis are *type I* and *type II*, as shown in Figure 2.8, where the light grey arrows represent that wave polarisation. Type I phase matching means that, for example, in SFG, the two fundamental beams have the same polarization, perpendicular to that of the sum frequency wave. Conversely, in type II phase matching, the two fundamental beams have different polarization directions. The distinction between type I and type II similarly applies to frequency doubling, and to processes such as parametric amplification.
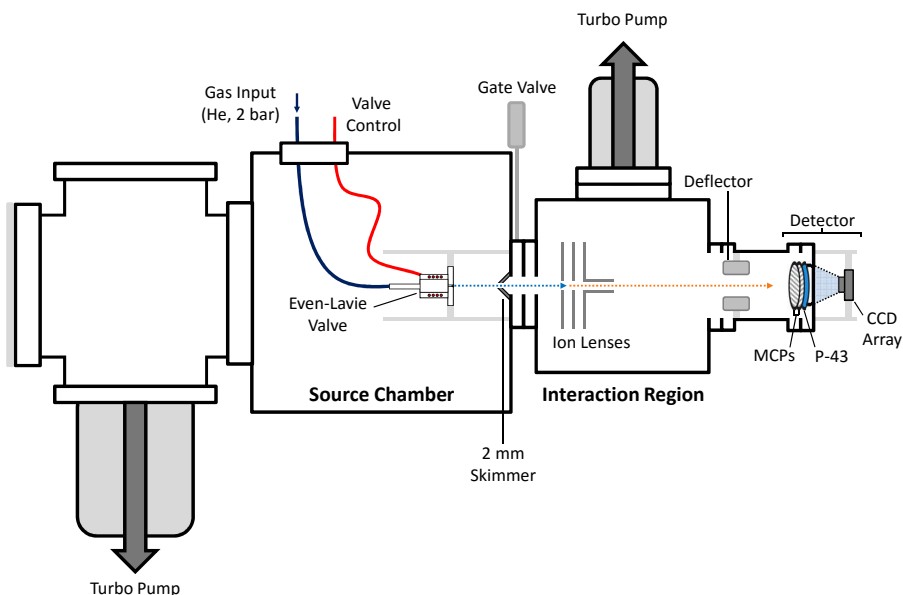
Figure 2.9: A diagram showing the layout of the vacuum chambers, and the components contained within, utilised in these experiments. The left most chamber serves to house the large turbo pump for the source. The middle cube is the source chamber where the pulsed valve is mounted and the right cube contains the electrostatic lens apparatus and the VMI detector.

2.3   Vacuum Chamber Setup

As we progressed through the introduction to this thesis we made reference to studying molecules in the gas phase as a means of isolating the systems from external perturbations. This is often achieved through the use of seeded molecular beams in a high vacuum environment. The supersonic expansion of a molecule into a region of very low pressure not only ensures the limited interaction with background gas, which could interfere with the experiments, but also yields "cold" gas phase molecules. This simplifies the spectroscopy greatly since only the lowest ro-vibrational eigenstates within the molecule are populated. The subsequent paragraphs detail first the design of the vacuum chamber, followed by the operation of the solenoid pulsed valve used for the generation of molecular beams.

Vacuum Chamber

The vacuum enclosures employed in these studies are shown schematically in Figure 2.9 and can be split into two important regions, the source and interaction chambers. The former, the middle cube in Figure 2.9, houses the pulsed solenoid valve, an Even-Lavie valve,[10] used to generate the cold molecular beam of target molecules (see below). During valve operation, the pressure in this region is normally on the order of 10^{-6} mbar, maintained by a 2200 Ls^{-1} turbo pump (Oerlikon Leybold Mag W 2200).

The interaction region, which is separated from the source chamber by a 2 mm stainless steel skimmer, is composed of a custom cube to house the ion optics and a
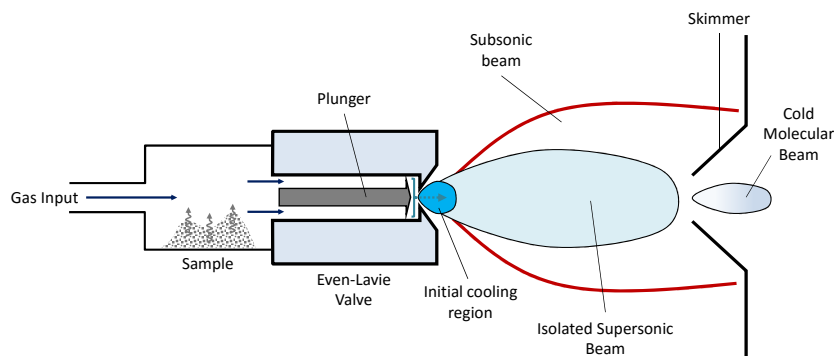
Figure 2.10: Schematic of the Even-Lavie pulsed solenoid valve. The diagram shows the supersonic jet expansion and how skimming the beam leaves the coldest (lowest internal energy) portion of the beam to be interrogated by the pump and probe pulses.

short TOF tube onto which the detection apparatus is mounted (Section 2.3.3 describes the VMI detector in more detail). On either side of the interaction chamber is a CaF_2 window which allows alignment of the lasers through the centre of the electrostatic lens arrangement where they perpendicularly intersect the skimmed molecular beam. The pressure in this region is controlled by a 700 Ls^{-1} turbo-molecular pump (Oerlikon Leybold Turbovac Mag W 700). Typically, the pressure is $\sim 7 \times 10^{-9}$ mbar when the valve is off, and $\sim 10^{-7}$ mbar during experiments.

2.3.1 Molecular Beams

The fundamental approach for the production of a molecular beam is to seed the target molecule into an inert gas such as helium or argon, before expanding the gas mixture into a vacuum through a cylindrically symmetric aperture. The large pressure difference between the nozzle and the vacuum chamber causes expansion of the gas, leading to collisional cooling of the sample at the early stages of beam generation, *i.e.* transfer of the molecules internal energy (E_{int}) into translational energy (E_{trans}) through inelastic collisions with the seed gas. Provided the pressure differential is large enough, the molecular beam will exceed the local speed of sound meaning that, after the initial cooling, no more collisions take place and the result is an energetically cold, isolated molecular beam. The physics governing the production of molecular beams is extensive and will not be discussed in detail here, however a rigorous description is given in Reference 11. Figure 2.10 shows the supersonic expansion of gas into vacuum schematically. As is highlighted, the coldest part of the molecular beam is at the centre of the expansion and so a skimmer is utilised in order to remove the hotter, subsonic part of the beam.

The choice of seed gas can have a profound effect on the properties of the molecular beam. For an ideal monoatomic gas, the terminal velocity v_0 of the molecular beam is described by the following relationship:[11,12]

$$v_0 = \sqrt{\frac{5k_BT}{m}} \tag{2.6}$$

where k_B is the Boltzmann constant, T is the temperature of the gas prior to expansion[iii] and m is the mass of the seed gas. It follows that a heavier seed gas will drastically reduce the beam velocity, which in turn allows for more significant cooling to take place following the initial expansion. The result of this cooler molecular beam is the formation of higher numbers of Van der Waals clusters.[11,12] In the case of the experiments here, helium is selected as the seed gas in order to reduce clustering. For a typical experiment, where the sample is heated to $\sim$100 °C, molecular beams with terminal velocities on the order of 2000 ms^{-1} can be routinely generated.

In principle, it is possible to create a continuous molecular beam for use in experiments, however, in practice, this can be problematic. The large throughput of gas required to maintain a supersonic expansion necessitates the incorporation of large turbo pumps to hold the high vacuum conditions, coupled with the large volume of sample required, meaning a continuous beam would be very costly. A far more effective method for the creation of molecular beams is to use a pulsed valve that is synchronised with the laser system. In this way, a small "packet" of cold molecules is released when the nozzle is temporarily opened. This eliminates the need for high gas loads and, as a convenient advantage, allows for detection of the front edge of the beam where the coldest molecules (*i.e.* molecules with lowest E_{int}) can be found.

In the experiments reported here, an Even-Lavie pulsed solenoid valve, backed by helium at a pressure of 2 bar and operating at 125 Hz,[iv] is used to generate our molecular beam of target molecules. Detailed insight into the operation of the Even-Lavie valve can be found in Reference 10, briefly however, the valve works by retracting a spring loaded magnetic plunger for a short time allowing analyte, which can be heated in an internal cartridge, and seed gas to expand into the vacuum. Exact operating conditions (opening times and valve temperatures) are outlined for each specific system in the relevant chapter, however typical opening times for the Even-Lavie valve are between $12 - 15$ μs. While we cannot directly measure the temperature of the beam itself, the Even-Lavie valve has been shown to produce rotational temperatures $\sim 5 - 10$ K.[10]

2.3.2 Time-resolved Ion Yield

We briefly introduced the concept of TR-IY in Section 1.5.4. operates in general, with experimental details of how this enables the collection of a TR-IY transient.

In an ideal system, all ions to be investigated will be initially positioned in the

---

[iii]For demonstrative purposes this can be approximated to be equal to the valve temperature.

[iv]This corresponds to the valve synchronising with 1 in 8 laser pulses.

same plane relative to the detector, between two plate electrodes known as the repeller (V_r) and the ground (V_g), as shown in Figure 2.11 (a). At a pre-defined time, known as time-zero (t_0), an equal amount of KE is imparted to each ion by the repeller electrode, which is set behind the interaction region. Mathematically this is expressed as follows:

$$qE_r = \frac{1}{2}mv^2 \tag{2.7}$$

The electric field, E_r, from the repeller electrode, injects the ions into a field free drift tube of length L, where they travel down the flight tube before impacting on the detector. For this simplified system, the TOF for a particular charged particle of mass m is given by the following equation:

$$TOF = L\sqrt{\frac{m}{2qE_r}} \tag{2.8}$$

where q is the ionic charge.

However, in a more realistic system, the ions created by a photolysis experiment will not exist in the same plane and there will be a much wider spatial distribution of ions as they recoil from the point of interaction with the dissociation laser. Wiley and McLaren demonstrated that inclusion of a second charged electrode, the extractor plate (V_e), introduces another acceleration region which can help counteract the initial spread of ions. The Wiley-Mclaren TOF set-up can be seen in Figure 2.11 (b). The first region (V_r/V_e) compensates for the differences in energy and position, while the second region (V_e/V_g) focuses them independently of these factors. The detailed mathematical description for flight times in the more complex, multi-electrode system is described in Wiley and McLaren's original publication.[13]

Acquiring a complete TOF spectrum (for all fragments) can be performed simply by recording the current output from the phosphor screen (used as part of the VMI setup-see below), relative to the laser pulse trigger, through an oscilloscope (LeCroy Waverunner LT372). For TR-IY of a particular fragment, a specific m/z value can be selected (from the TOF spectrum) post-ionisation (see below) and the fragment yield measured as a function of the pump-probe time delay, producing a
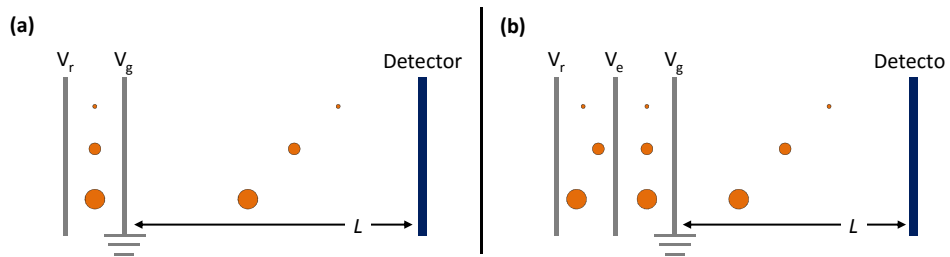
Figure 2.11: Schematic for a TOF mass spectrometer with (a) a single acceleration region (V_r/V_g), and (b) two acceleration regions $(V_r/V_e$ and $V_e/V_g)$ as in a Wiley-McLaren setup. Shown are the ion optics as well as representative positions for three ions of different masses.
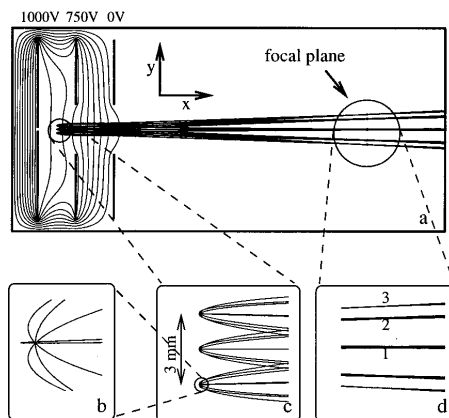
Figure 2.12: Ion trajectory simulation demonstrating velocity map imaging. The electrostatic lens shown in (a) results in conditions whereby particles with different initial positions (c) are mapped to a final position dependant only on their velocity (d). The particles all have equal speeds, but are ejected from the interaction point at varying angles; 1, 2 and 3 correspond to ejection angles $0/180°$ (x direction), $45/135°$ and $90°$ (y direction), respectively. Reproduced from Reference 14.

transient for that particular fragment mass. In this thesis, TR-IY is utilised to provide information on the excited state lifetime of the photoexcited parent molecule. If a molecule that exhibits no time-resolved dynamics (such as MeOH or Xenon) is introduced to the gas phase we can use TR-IY of the parent to determine the cross-correlation of the laser pulses, this in turn yields the instrument response function (IRF-see Section 2.3.4).

2.3.3   Velocity Map Imaging

We discussed in the Introduction that VMI is an incredibly powerful technique, and since its implementation it has revolutionised the field of chemical dynamics. By providing both angular and energetic information from a single image, far more accurate tracking of electronic state population transfer has been achieved.

Imaging the products of photoinduced fragmentation reactions, utilising the gridded form of the Wiley-McLaron type electrodes,[13] was first performed by Chandler and Houston during the 80's,[15]. In these experiments resolution was limited owing to the interaction of the generated ions with the grids covering the plate apertures. It was Eppink and Parker that realised removal of the mesh grid of the accelerator and ground electrodes, leaving behind a simple plate electrode with a hole, created an electrostatic lens which possesses the ability to map the velocity of recoiling fragments onto specific regions of the detector array. Provided the ratio of voltages between the repeller and extractor (V_r/V_e) is kept at a value of ~ 0.7, the velocity mapping conditions were irrespective of the initial particle position and vastly improved spatial, and hence energetic, resolution was reported.[14] Figure 2.12 shows the original Simion simulations from Eppink and Parker; elegantly illustrating how mapping trajectories are consistent regardless of the initial ion
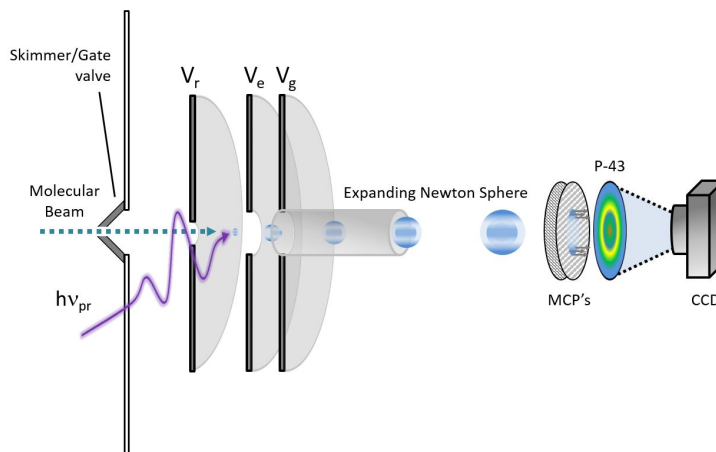
Figure 2.13: Schematic of the VMI setup including the electrostatic lenses (left) and the detector consisting of two MCPs, P-43 screen and CCD array. The laser pulses ($h\nu_{\mathrm{pu}}$ and $h\nu_{\mathrm{pr}}$- only $h\nu_{\mathrm{pr}}$ is shown for clarity) have an electric field polarised parallel to the detector.

position.

The VMI apparatus used in the present experiments is shown in Figure 2.13 and resembles the original design of Eppink and Parker.[14] The left of the schematic shows the electrostatic lens arrangement while the right side highlights the VMI detector. The first two electrodes, (V_r and V_e), are based on a pair of grid-less Wiley-McLaren TOF electrodes. The third plate is simply a grounded plate that serves to protect against stray electrical fields and prevent distortion of the final image. Usual operating voltages for the two plates are approximately 3500 V and 2500 V for V_r and V_e, respectively, in line with V_r/V_e ratio of ~0.7 outlined by Eppink and Parker.[14] As can be seen from the schematic, the electrostatic plates are positioned such that the molecular beam (oriented in-line with the VMI stack) and the laser beam (propagating perpendicular to the detector) intersect in the centre of the electrostatic lens.[v] Thus, following a photolysis event, the created Newton Sphere is focused down the TOF tube onto the position sensitive detector.

The VMI detector is comprised of two micro-channel plates (MCPs) in a chevron formation. A MCP, for all intents and purposes, is an electron multiplier which, due to the plate possessing many channels for electron multiplication, also provides spatial resolution. Behind the second MCP is mounted a P-43 phosphor screen (Photek) which luminesces following electron impact. The emitted light is captured by a charge couple device (CCD) camera (Basler, A312f) which links to a custom recording program built in the LabVIEW platform. While running imaging

---

[v]It should be noted that experiments performed on resorcinol were collected using a slightly modified experimental setup.[1,16] The main difference between the two systems being the position of the detector array, which was perpendicular relative to the molecular beam path for resorcinol. This required the laser polarisation, ε_{pu}, to be rotated 90° (parallel with the plane of the laser table) in order to retain the cylindrical symmetry of the generated Newton sphere, see Section 2.3.3. Additionally, typical operating voltages for these experiments were on the order of 5000 V and 3570 V for V_r and V_e, respectively.

experiments a potential difference of between 600 – 800 V is applied across each MCP, with the phosphor screen held at 5 kV. While running ion yield measurements (or measuring a TOF-MS), we extract current from the front end of the phosphor screen; this enables us to record the ion signal on an oscilloscope. As such, the setup can operate both as a TOF-mass spectrometer and VMI spectrometer.

Given the fact that we have a combined mass and VMI spectrometer, it is often necessary to gate onto an ion with a particular m/z value. Selection of a specific mass channel is achieved through two methods. First, a pair of deflector plates, mounted in front of the MCPs, deflect ions of a higher mass than the target species, using a purpose built delay generator and high voltage switch. Second, we manipulate the gain potential of the rear MCP. The voltage across the rear MCP is switched from higher voltage (usually ∼1400 – 1600 V is used to detect the ions of interest) to 600 – 800 V, *i.e.* the same voltage as applied across the front MCP resulting in a considerably reduced gain in ion signal. Switching the potential difference this way is carried out using another high voltage switch (Behlke GHTS 60) and purpose-built delay generator. During operation, if large numbers of charged species are incident on the detector at a specific position (*i.e.* we are creating a considerable population of species with similar velocities) then desensitisation of the phosphor screen can occur. As such, deflecting ions as described above also has the added benefit of limiting damage by reducing the total number of charged species impacting on the detector.

Angular Distributions

We have mentioned on numerous occasions throughout this thesis that VMI provides angular information in coincidence with energetic information, *i.e.* not only can we ascertain the KE of a photofragment, we can also determine the *direction* the particles leave relative to the electric field vector of the pump laser (ε_{pu}). This is a direct consequence of the interaction of the polarised laser pulse with the target molecules' TDM, which we discussed in Section 1.2.4. The result of this interaction is that molecules whose TDM is aligned parallel to ε_{pu} are preferentially excited by the pump pulse. Knowledge of the molecules' TDM allows information on the alignment of the molecules prior to photodissociation to be inferred, providing details on the excited states that are populated by the initial pump pulse.

In order to quantitatively describe the angular distribution, $I(\theta)$, where θ is the angle between the dissociating fragments velocity vector ($\boldsymbol{v}$) and ε_{pu}, of the dissociated photofragments we use the following expression:[17]

$$I(\theta) = \frac{\sigma}{4\pi}\left[1 + \sum_n \beta_n P_n(\cos\theta)\right] \tag{2.9}$$

where σ describes the total cross-section $P_n(\cos\theta)$ is the nth order Legendre polynomial, and β_n is the associated anisotropy parameter.[17] In general, $I(\theta)$ can be described completely by even values of n, up to a value equal to twice the number of
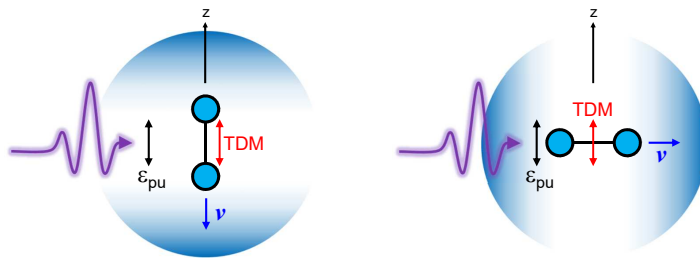
Figure 2.14: Simple example demonstrating the origins of angular distributions in VMI. If the TDM lies along the bond dissociation axis (v), the departing fragments will be parallel to both this axis and the laser polarisation axis (ε_{pu}), $\beta_2 = +2$. The converse is true if the TDM is perpendicular to the bond dissociation axis, $\beta_2 = -1$.

photons required for the dissociation mechanism. Thus, for a one photon process, only the first even term in the expansion (P_2 and corresponding β_2) is necessary.[vi] Given this and noting that the second order Legendre polynomial is:

$$P_2(\cos\,\theta) = \frac{(3\cos^2\theta - 1)}{2}, \tag{2.10}$$

allows $I(\theta)$ to be modelled by the following:

$$I(\theta) = \frac{\sigma}{4\pi}\left[1 + \beta_2\frac{1}{2}(3\cos^2\theta - 1)\right] \tag{2.11}$$

The β_2 parameter has limiting values of -1 and +2, where -1 represents a transition in which the TDM is aligned perpendicular to the bond dissociation axis and +2 indicates a case where the TDM is oriented parallel to this axis. The two limiting cases are shown in Figure 2.14. It is important to note that the value that β_2 takes is indicative of the angular relationship between the TDM and $I(\theta)$.[17] If the TDM for the relevant electronic excited states are calculated (from first principles or using computational methods), it is possible to distinguish which state (or states) are populated prior to dissociation.

A β_2 value that approaches 0, *i.e.* a near isotropic distribution, can also be obtained. This is indicative of three possible scenarios: (i) if the TDM lies at the *magic angle* (54.7^o) with respect to the dissociating bond; (ii) if photoexcitation to multiple excited states, with TDMs that cancel each other out, takes place simultaneously; or (iii) the dissociation event takes place on a timescale that is much slower than the rotational period of the parent molecule bringing about a rotational dephasing of the initial "alignment" created as a result of ε_{pu}. Coupled with theoretical calculations, an isotropic distribution can often prove useful for identifying the origins of certain signals obtained within a VMI image.[17–21]

[vi]Higher order even terms of the Legendre polynomial, and the relevant beta parameters ($\beta_4, \beta_6...$), are required to describe $I(\theta)$ completely when considering multiphoton processes such as those often utilised in photoelectron spectroscopy.
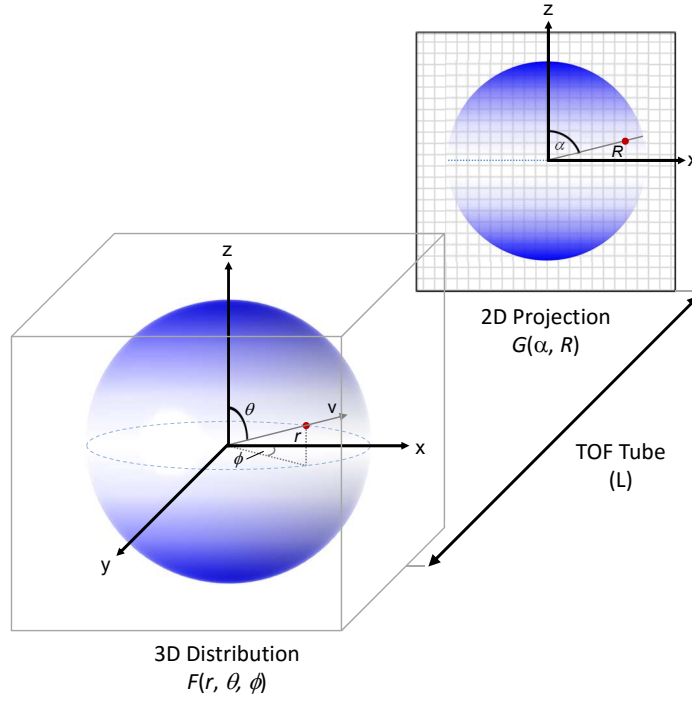
Figure 2.15: Velocity mapping of a 3D Newton Sphere distribution of charged particles with velocity (v), which can be described in polar coordinates as the function $F(r, \theta, \phi)$. This cylindrically symmetric (about the z-axis) distribution is then projected along the TOF tube, L, and mapped as a 2D distribution in terms of a radius (R) and angle (α).

Image Reconstruction

We have discussed that a photolysis event causes recoil of photofragments creating a 3D distribution, known as a Newton Sphere, which contains the velocity (and angular) information that we desire. It is possible to integrate this 3D distribution over all θ and ϕ, which are the zenith and azimuthal angles, respectively, to produce the associated 1D velocity spectrum, $I(v)$:

$$I(v) \propto \int\limits_0^{2\pi} \int\limits_0^{\pi} F(r, \theta, \phi) r^2 sin\theta \, d\theta \, d\phi \qquad (2.12)$$

where v is proportional to the radius, r.

However, in our VMI arrangement the detector is a 2D array and so, when the Newton Sphere is projected along the TOF tube onto the detector, there is an apparent loss of dimensionality: the original 3D distribution, $F(r, \theta, \phi)$ is compressed into a 2D projection, $G(R, \alpha)$ where R is the circle radius and α is the angle, causing the ϕ component to become convoluted into $G(R, \alpha)$. This is shown schematically in Figure 2.15. In order to extract $I(v)$ (or $I(r)$) we must utilise a method that extracts the original 3D image from the convoluted 2D data.

The reconstruction of the 3D image can be done physically or through the use of numerous deconvolution algorithms. The physical extraction of the 3D distribution can be performed by direct current slice imaging, a method where a pulsed detector

2D Projection
$G(\alpha, R)$

Slice
$F(r_{max}, \theta, \phi = 0)$

Reconstructed 3D distribution
$$\int_0^{2\pi} F(r_{max}, \theta, \phi = 0) \, d\theta \, \sqrt{r} \, \sin\theta$$

Radial spectrum
$I(r)$
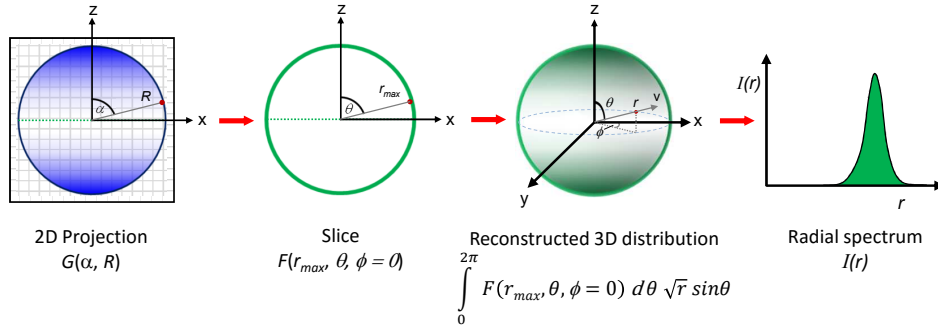
Figure 2.16: Schematic of the steps involved in image deconvolution. From a 2D image, an effective slice at $\phi = 0$ is taken and then the 3D distribution is reconstructed using the POP algorithm. The full reconstructed 3D distribution is then converted to a 1D radial spectrum by integration over all angles. See main text for further details.

samples a central 'slice' from the sphere while the remaining signal is discarded.[22–24] The more common technique utilises mathematical algorithms in order to reproduce the original 3D distribution, again by obtaining a slice through the centre of the 3D sphere. There are many approaches to deconvolution, however, in this thesis, the Polar Onion Peeling (POP) algorithm is employed. POP is an attractive method for deconvolution because it is fast and can be done "on the fly", but is also very intuitive. Full details can be found in the thesis of Dr Gareth Roberts[25] and the original POP publication;[18] but, in the interest of completeness, a brief introduction is presented here.

For photodissociation and photoionisation experiments the original Newton Sphere possesses cylindrical symmetry, induced by the polarisation vector of ε_{pu}, which in this instance is about the z-axis in Figure 2.15. It should be noted that in order to retain the cylindrical symmetry the plane of the laser polarisation must be parallel to the detector, else all signals will appear isotropic and any angular information is irrecoverable. As mentioned above, the fundamental aim of deconvolution methods (and indeed slice imaging techniques) is to acquire a central 'slice' from the 3D distribution which corresponds to $\phi = 0$ ($F(r, \theta, \phi = 0)$). Due to the inherent cylindrical symmetry of the Newton Sphere, this slice can then be used to extract (or rather, simulate) $F(r, \theta, \phi)$ allowing us to obtain $I(r)$.

Guided by the schematic in Figure 2.16, the image deconvolution process begins with the 2D image data (the output from the P-43 screen which is recorded by the CCD array). Starting at the outer most radius, which is described by the function $h(r_{max}, \theta)$, the data is fit with the angular distribution (*vide supra*):[19,26]

$$I(\theta) = N(r) \sum_n \beta_n(r) P_n(\cos\theta) \tag{2.13}$$

yielding the intensity factor, $N(r)$, and the anisotropy parameters, $\beta_n(r)$. These values are then used, by comparison with pre-generated basis functions, in order to generate a simulated slice $g_{fit}(r_{max}; R, \alpha)$. This is then subtracted from $G(R, \alpha)$ to

remove the ϕ-contribution associated with r_{max}:

$$G^*(R, \alpha) = G(R, \alpha) - g_{fit}(r_{max}; R, \alpha) \tag{2.14}$$

This subtraction process is then repeated until the centre of the image is reached $(r = 0)$, effectively removing the ϕ-component of each radius. By retaining $h(r_{max}, \theta)$ obtained at each stage in the subtraction process in a separate matrix, the desired 2D slice, $F(r, \theta, \phi = 0)$, can be generated. Access to $F(r, \theta, \phi = 0)$, means the full 3D distribution, which is reconstructed using a $\sqrt{r}\, sin\, \theta$ scaling factor, can ultimately be integrated over all values of θ:

$$I(r) = \int\limits_{0}^{2\pi} F(r, \theta, \phi = 0)\, \sqrt{r}\, sin\, \theta\, d\theta \tag{2.15}$$

to yield the desired 1D radial spectrum. By conversion with a known calibration factor (see Section 2.3.4) $I(r)$ can be used to generate a spectrum which shows the KE of the photofragments released following photolysis.

2.3.4   Calibration

VMI Calibration

Following the deconvolution of a VMI image, the recorded 2D image is subject to the appropriate Jacobian transformation ($r^2 \propto$ KE) which yields a 1D intensity spectrum as a function of pixel radius (r) such as that shown in Figure 2.17 (a). In order to retroactively assign which electronic state our photofragments originate from, we must know the KE of the dissociated fragments. This requires calibration of the VMI detector with a known reference, from this we can calculate a calibration factor that allows us to relate r to the total kinetic energy release (TKER).

In our experiments the calibration is performed using the elimination of H atoms from HBr following photolysis with a 200 nm pump laser. HBr has been very well characterised by previous investigations, making calibration straightforward.[27,28] The bond dissociation energy (BDE) for the H–Br bond has been reported to be 30210 ± 40 cm^{-1}. Following interaction with the photolysis pulse, elimination of the H atom yields bromine in both spin-orbit ground and spin-orbit excited states ($^2P_{3/2}$ and $^2P_{1/2}$, respectively). Both states have very narrow linewidths, and are separated by a well-known value (3685.24 cm^{-1}) due to spin-orbit coupling.[27] The *total* kinetic energy released (TKER) for this process is determined according to:[21]

$$\text{TKER} = h\nu_{\text{pu}} - BDE_{(HBr)} - E_{(elec)} - E_{(vib)} \tag{2.16}$$

where $E_{(vib)} = 0$ for HBr dissociation and $E_{(elec)}$ comprises the two spin orbit states described above. One factor that is neglected in the above equation is the conservation of momentum for the two photofragments following dissociation. This allows the recorded H atom KER (H-KER) to be converted into TKER *via* the

following:

$$\text{TKER} = \text{H-KER} \left(\frac{m_p}{m_p - m_H} \right) \tag{2.17}$$

where m_H and m_p are the masses of the H and the parent molecule, respectively.[21]

A representative example of the 1D spectrum obtained from HBr following excitation with 200 nm and probing with 243 nm, plotted as a function of r, is shown in Figure 2.17 (a). The four peaks present in the spectrum are assigned as follows: the two peaks at large r correspond to ground and excited state Br formed from photolysis with the 200 nm pulse, while the two peaks at smaller radii are from pumping and probing within the duration of the 243 nm pulse (a multiphoton event). Calibration can be performed with both pairs of peaks. By plotting the H-KER against the square of the pixel radius (r^2) and utilising the equations above, the calibration factor, 0.4404 cm^{-1} pixel^{-2}, is obtained.
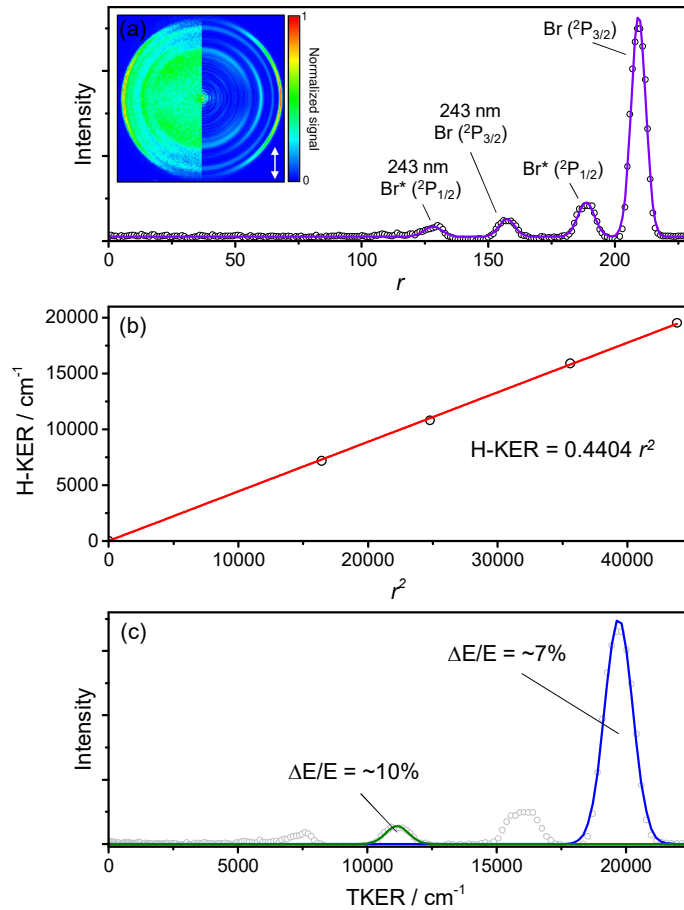
Figure 2.17: VMI calibration for H atom dissociation from HBr: (a) the 1D spectrum in terms of r, showing the four peaks corresponding to the four different bromine dissociation channels (see main text for details). Inset: H$^+$ velocity map image from which the TKER spectra is derived (left half) together with the reconstructed slice of the original 3D ion distribution (right half); (b) a plot of the assigned H-KER for each feature against pixel radius squared (r^2); (c) TKER for the same HBr spectrum with associated peak resolution.

The TKER spectrum for HBr is shown in Figure 2.17 (c). It is also possible to obtain the instrument resolution ($\Delta E/E$) from the peak linewidths in the calibration image, and a resolution of $\sim$7% is obtained. This seemingly poor resolution is caused by the broad bandwidth of the laser pulses ($\sim$500 cm^{-1}).

TOF Calibration

The TOF must also be calibrated to ensure the masses we are investigating are indeed the fragments of interest. The calibration is similar to the calibration of the VMI; the mass of a particular fragment, m_A, can be determined by its arrival time, t_A by comparing to the arrival time of a known reference mass, t_{ref} and m_{ref}, respectively, through the following:

$$
t_A = \left[\sqrt{\frac{m_A}{m_{ref}}} \times (t_{ref} - t_L) \right] + t_L
$$
$$
m_A = \left(\frac{t_A - t_L}{t_{ref} - t_L} \right)^2 \times m_{ref}
$$

(2.18)

where t_L is the delay between the oscilloscope trigger and the arrival of the laser pulse, which is typically on the order of 300 ns.

Cross-correlation and Time Zero

The temporal resolution of the experiments (the instrument response function (IRF)) in this thesis is obtained from the *cross correlation* of the pump and probe pulses. In order to acquire the cross correlation, the parent ion signal of methanol (MeOH$^+$) or xenon is measured as a function of the pump probe delay (Δt) before being fit with a Gaussian function. These two species are chosen because they are both trivial to introduce into the pulsed valve and also because both exhibit no excited state dynamics at the wavelengths utilised ($\geq$ 200 nm). The lack of dynamics is crucial in obtaining a precise value for the FWHM (equates to the IRF) and
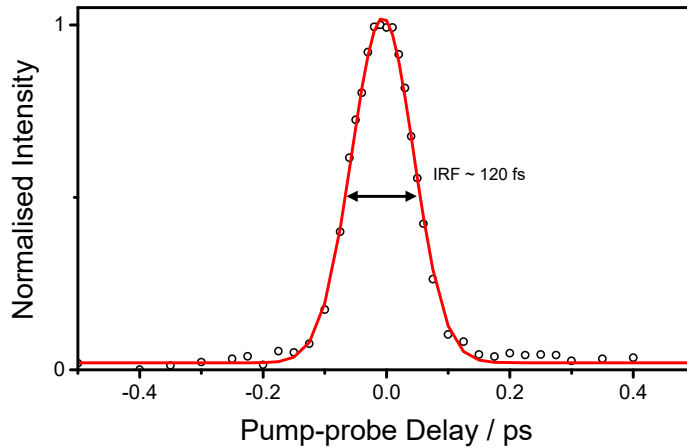
Figure 2.18: Cross correlation of xenon following excitation and subsequent probing with 301 nm and 243 nm, respectively.

centre (time zero - t_0) of the Gaussian laser pulses. An example cross correlation measurement of xenon can be seen in Figure 2.18. A typical value for the IRF when using the TOPAS-C's for both pump and probe pulses is ∼120 fs FWHM.

References

1. Chatterley, A. *Ph.D. Thesis.* University of Warwick/University of Durham, (2014).

2. Moulton, P. F. *J. Opt. Soc. Am. B* **3**(1), 125–133 (1986).

3. Greenough, S. *Ph.D. Thesis.* University of Warwick, (2015).

4. Parker, S. P. *McGraw-Hill Encyclopedia Of Physics.* McGraw-Hill Book Company, New York, NY, (1983).

5. Griffiths, D. J. and College, R. *Introduction to electrodynamics.* prentice Hall Upper Saddle River, NJ, (1999).

6. Wilson, J. and Hawkes, J. F. B. *Optoelectronics: An Introduction 3rd Ed.* Prentice Hall, (1997).

7. Hecht, E. *Optics 4th Ed.* Addison Wesley, (2003).

8. Paschotta, R. *Encyclopedia of laser physics and technology.* Wiley-VCH Berlin, (2008).

9. Franken, P. A., Hill, A. E., Peters, C. W., and Weinreich, G. *Phys. Rev. Lett.* **7**, 118–119 Aug (1961).

10. Even, U., Jortner, J., Noy, D., Lavie, N., and Cossart-Magos, C. *J. Chem. Phys.* **112**(18), 8068–8071 (2000).

11. Scoles, G., Bassi, D., Buck, U., and Lain, D. *Atomic and molecular beam methods.* Oxford university press New York, (1988).

12. Christen, W. and Rademann, K. *Phys. Rev. A* **77**, 012702 Jan (2008).

13. Wiley, W. and McLaren, I. H. *Rev. Sci. Instrum.* **26**(12), 1150–1157 (1955).

14. Eppink, A. T. J. B. and Parker, D. H. *Rev. Sci. Instrum.* **68**(9), 3477–3484 (1997).

15. Chandler, D. W. and Houston, P. L. *J. Chem. Phys.* **87**(2), 1445–1447 (1987).

16. Iqbal, A., Pegg, L.-J., and Stavros, V. G. *J. Phys. Chem. A* **112**(39), 9531–9534 (2008).

17. Eppink, A. T. J. B., Wu, S. M., and Whitaker, B. J. *Imaging in molecular dynamics: technology and applications.* Cambridge university press, (2003).

18. Roberts, G. M., Nixon, J. L., Lecointre, J., Wrede, E., and Verlet, J. R. R. *Rev. Sci. Instrum.* **80**(5), 053104 (2009).

19. Zare, R. N. *Angular momentum: understanding spatial aspects in chemistry and physics.* Wiley-Interscience, (1988).

20. Ashfold, M. N. R., Nahler, N. H., Orr-Ewing, A. J., Vieuxmaire, O. P. J., Toomes, R. L., Kitsopoulos, T. N., Garcia, I. A., Chestakov, D. A., Wu, S. M., and Parker, D. H. *Phys. Chem. Chem. Phys.* **8**(1), 26–53 (2006).

21. Roberts, G. M. and Stavros, V. G. *Chem. Sci.* **5**(5), 1698–1722 (2014).

22. Townsend, D., Minitti, M. P., and Suits, A. G. *Rev. Sci. Instrum.* **74**(4), 2530–2539 (2003).

23. Gebhardt, C. R., Rakitzis, T. P., Samartzis, P. C., Ladopoulos, V., and Kitsopoulos, T. N. *Rev. Sci. Instrum.* **72**(10), 3848–3853 (2001).

24. Lin, S. H., Fujimura, Y., Neusser, H. J., and Schlag, E. W. *Multiphoton spectroscopy of molecules.* Elsevier, (2012).

25. Roberts, G. M. *Ph.D. Thesis.* University of Durham, (2010).

26. Reid, K. L. *Annu. Rev. Phys. Chem.* **54**(1), 397–424 (2003).

27. Regan, P. M., Langford, S. R., Orr-Ewing, A. J., and Ashfold, M. N. R. *J. Chem. Phys.* **110**(1), 281–288 (1999).

28. Sansonetti, J. E., Martin, W., and Young, S. *J. Phys. Chem. Ref. Data* **34**, 1559 (2005).

Chapter 3

Relaxation Dynamics of Photoexcited Resorcinol

Internal Conversion versus H atom Tunnelling
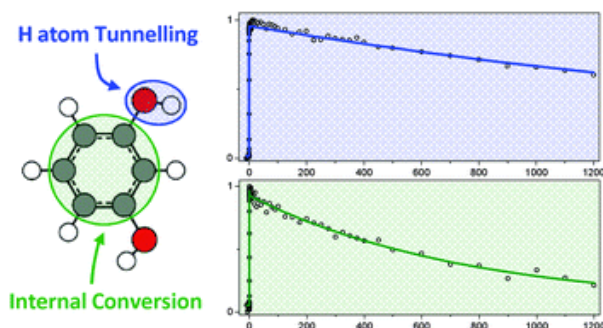
This chapter is based on the following publication:

3.1   Introduction

In the following chapter we explore the deactivation mechanisms occurring upon UV excitation of resorcinol (1,3-dihydroxybenzene, structure shown inset in Figure 3.1) using a combination of ultrafast time-resolved velocity map imaging (TR-VMI) and time-resolved ion yield (TR-IY) experiments, in conjunction with high level *ab initio* calculations. Resorcinol is closely related to the prototypical system phenol, which we discussed in Section 1.6, and possesses a very similar excited state landscape. The reader is referred back to the introduction, and to Figure 3.2, for an overview of the states accessed following UV excitation in such systems.

When compared to phenol itself, there are relatively few investigations reporting the excited state dynamics of its hydroxy-substituted derivatives: catechol (1,2-dihydroxybenzene), hydroquinone (1,4-dihydroxybenzene) and resorcinol. Only very recently have more detailed investigations been performed to understand the excited state dynamics in these species, of which catechol has received the most attention.[1–3] The studies on catechol were particularly notable, as although the dynamics observed in TR-VMI, TR-IY and time-resolved photoelectron imaging (TR-PEI) experiments could be qualitatively rationalised through a comparison with phenol, the tunnelling rate under the $1^1\pi\pi^*/^1\pi\sigma^*$ conical intersection (CI) was found to be $\sim$2 orders of magnitude greater (5 – 12 ps lifetime, *cf.* >1 ns in phenol[4]), despite a similar barrier height to phenol along $R_{\text{O–H}}$. Such an observation was proposed to be a direct consequence of the non-planar $1^1\pi\pi^*$ minimum energy geometry in catechol, yielding relaxed symmetry constraints for $1^1\pi\pi^* \rightarrow {}^1\pi\sigma^*$ coupling and a highly *'vibrationally-enhanced'* tunnelling process.[2] Conversely, the minima of the $1^1\pi\pi^*$ states in hydroquinone and resorcinol are both planar, and the recent TR-PEI experiments by Livingstone *et al.* (after excitation at 267 nm) found that both species exhibited relaxation dynamics more akin to phenol, identi-
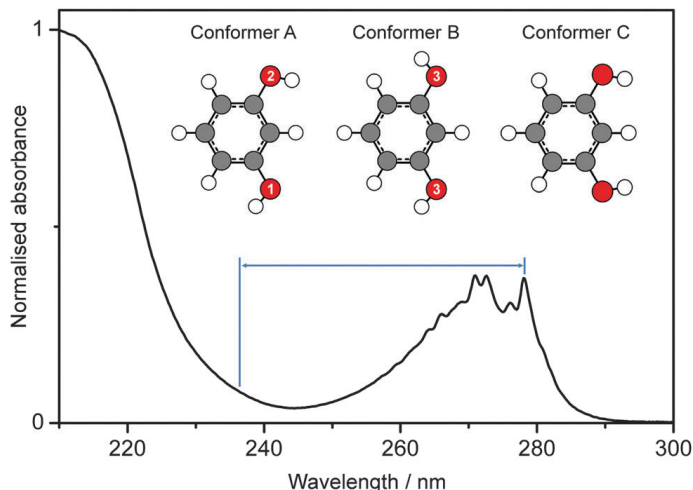
Figure 3.1: Vapour-phase absorption spectrum of resorcinol between 300 - 210 nm, indicating the excitation wavelength range ($h\nu_{\text{pu}}$) investigated in this study. Molecular structures of the three conformers (A, B and C) are shown inset.

fying two time constants; a long time component, occurring on a timescale ≥ 430 ps, and a shorter sub-picosecond component.[1] The long time dynamics observed were assigned to population decaying out of the $1^1\pi\pi^*$ state, driven (at least in part) by tunnelling beneath the $1^1\pi\pi^*/^1\pi\sigma^*$ CI, while the latter rapid sub-picosecond component was ascribed to ultrafast intramolecular vibrational redistribution (IVR) mediated by 'doorway' states on the $1^1\pi\pi^*$ surface. In the specific case of resorcinol, the lifetime of the $1^1\pi\pi^*$ state extracted from the time-resolved photoelectron spectrum at 267 nm was given as >1 ns and the authors noted that they could not make a more reliable estimate for the lifetime due the temporal limits of their experimental setup.

As well as the above study in the time-domain, high resolution microwave and electronic spectroscopy, coupled with *ab initio* calculations, have also been performed on resorcinol.[1,5–7] It has been proposed that resorcinol may exist in three possible conformations (labelled A–C in Figure 3.1), brought about by variation in the orientations of the OH groups (labelled 1–3 in Figure 3.1), although only two of these have been spectroscopically observed in the gas phase under jet expansion conditions. These two conformers, labelled A and B in Figure 3.1, are nearly iso-energetic, separated only by ~ 10 cm^{-1}.[7] Using spectral-hole burning, Gerhards *et al.* were able to identify two transitions at 35944 cm^{-1} (278.2 nm) and 36196 cm^{-1} (276.3 nm), and assigned them to the $1^1\pi\pi^* \leftarrow S_0$ origin bands for the A and B conformers, respectively.[7] Further high resolution dispersed fluorescence spectroscopy studies on isotopically substituted resorcinol, its cations and the molecule itself have yielded a greater understanding of the structure and vibrations in the S_0, $1^1\pi\pi^*$ and cation electronic states.[5–7]

With the exception of the TR-PEI work conducted by Livingstone *et al.* at 267 nm,[1] there have been no other studies investigating the dynamics that take place within photoexcited resorcinol in the time-domain. To this end, this chapter presents a comprehensive study of the relaxation dynamics of resorcinol after photoexcitation at a number of wavelengths across the range 278 – 237 nm, using a combination of TR-VMI and TR-IY experiments, in conjunction with detailed theoretical calculations using the complete-active space self-consistent field (CASSCF) method together with its second order perturbation theory extension (CASPT2).

3.2 Methods

3.2.1 Experimental

The experiment was described in greater detail in Chapter 2, and as such only a brief overview, including exact experimental details, is given here. Laser pulses from the commercial laser system were used to seed the two OPAs in order to generate the pump ($h\nu_{pu}$) and probe ($h\nu_{pr}$) pulses. In this instance $h\nu_{pu}$ was tuned in the range 278 – 255 nm ($\sim 2.5 - 5$ μJ/pulse) and the $h\nu_{pr}$ fixed at 243 nm (~ 6 μJ/pulse) in line with the two photon allowed $2s \leftarrow 1s$ transition in H. The pump

and probe pulses were temporally delayed with respect to each other by reflecting the probe beam off the hollow gold retroreflector mounted on the motorised delay stage, allowing a maximum temporal delay (Δt) of 1.2 ns.

The molecular beam was produced by seeding resorcinol (Sigma-Aldrich, 99%), heated to 100°C, into helium and introducing into vacuum through the Even-Lavie pulsed solenoid valve[8] operating at a 125 Hz repetition rate with a typical opening time of 14 μs. Studies were also carried out on resorcinol-d_2, which was synthesised by dissolving resorcinol in D_2O, stirring and then evaporating the excess heavy water using a rotary evaporator. Non-resonant multiphoton ionisation of methanol was used to measure the delay position corresponding to temporal overlap of $h\nu_{pu}$ and $h\nu_{pr}$ pulses ($\Delta t = 0$), see Section 2.3.4 for further details.

At the point of intersection, following photolysis by $h\nu_{pu}$, the resulting H atoms were probed using VMI as described in Section 2.3.3. To recap briefly however, firstly, the H atoms are ionised by the $h\nu_{pr}$ pulses forming H^+. The 3D velocity distribution of H^+ is then focused using the ion optics, onto the position sensitive detector. The rear MCP is gated using a timed voltage pulse in order to detect only H^+ (1 amu). The photoemission from the phosphor screen is then captured using the CCD camera and the 3D distribution, once reconstructed using the polar onion peeling (POP) algorithm, is used to produce a total kinetic energy release (TKER) spectrum.

In addition to the TR-VMI measurements, we recorded TR-IY measurements of the resorcinol parent cation (resorcinol$^+$). Additionally, the gas phase absorption spectrum of resorcinol in Figure 3.1 was recorded over the range 210 – 300 nm using a commercially available UV-visible spectrometer (Perkin-Elmer, Lambda 25, 0.2 nm resolution). The spectrum was recorded by placing a small mass of resorcinol into a fused silica sample cell and heating to $\sim$ 80°C in order to obtain sufficient vapour pressure.

3.2.2 Theoretical Methods

Vertical excitation energies were calculated using both Gaussian[9,10] and Molpro computational suites.[11] Density functional theory (DFT) was used to perform all geometry optimisations with the PBE0[12] functional, together with the aug-cc-pVTZ basis set. For geometry optimised structures of conformers A and B (see Figure 3.1), both equation-of-motion coupled cluster with single and double excitations (EOM-CCSD[13]) and time-dependent density functional theory with the PBE0 functional (TD-PBE0) were then used to calculate vertical excitation energies (ΔE_{vert}) of the $1^1\pi\pi^*$, $2^1\pi\pi^*$ and $^1\pi\sigma^*_{O^n-H}$ states. The aug-cc-pVDZ and aug-cc-pVTZ basis sets were used for the EOM-CCSD and TD-PBE0 calculations, respectively. Torsional barriers to interconversion between conformers A/B and A/C were determined at the PBE0/aug-cc-pVTZ level in the S_0 ground state. At each torsional angle (θ), θ was held fixed and the remaining nuclear coordinates were allowed to 'relax'. Insight into the torsional barriers in the $1^1\pi\pi^*$ state are

determined by calculating the vertical excitation energies at the TD-PBE0/aug-cc-pVTZ level for each point along the 'relaxed' torsional coordinates in the S_0 state. Bond dissociation energies (BDEs) were computed by performing ground state geometry optimisations on the two conformers as well as the two possible radical products produced following dissociation of the O^n–H bond. The PBE0 functional was used with an aug-cc-pVTZ basis set. Zero point energy corrections were applied in all cases, extracted from frequency calculations performed to the same level of theory. The PBE0 functional has been selected since a recent survey of functionals for performing TD-DFT, by Leang et al.,[14] has indicated the PBE0 functional provides the most balanced description of both valence and Rydberg excited electronic states (both of which are important here in resorcinol), when benchmarked against experimental measurements. All TD-DFT and EOM-CCSD calculations were performed using the Gaussian09 computational suite.[10]

Minimum energy crossing point (MECPs) structures and two-dimensional branching spaces for CIs in resorcinol were calculated using the CASSCF method with the 6-31G* basis set. For CIs involving excited $^1\pi\sigma^*_{O^n-H}$ surfaces, a 12 electrons in 10 orbitals (12,10) active space was used consisting of the three π bonding orbitals, the two $n\pi$ non-bonding orbitals associated with the O atoms (conjugated into ring π-system), the three π^* anti-bonding orbitals and the corresponding σ bonding and σ^* anti-bonding orbitals associated with the given O^n–H bond coordinate of interest. A smaller (10,8) active space, excluding the σ and σ^* orbitals associated with the O^n–H bond, was used to isolate MECPs for CIs between $1^1\pi\pi^*/S_0$ and $2^1\pi\pi^*/1^1\pi\pi^*$ electronic states. Analytical gradient driven techniques were used to locate all MECPs of the CI seams, using the method described by Robb and co-workers,[15] as implemented in Gaussian03. Solutions to the coupled-perturbed multi-configurational self-consistent field (CP-MCSCF) equations in state-averaged CI optimisations were approximated by neglecting orbital rotation derivatives.

Molpro calculations were performed using CASPT2 theory[16,17] with a 12 electrons in 12 orbitals (12,12) active space and the aug-cc-pVTZ basis set. Further geometry optimisation was performed using CASSCF(12,12) theory[18,19] as implemented in Gaussian03 with the same basis. In addition to the orbitals described above for the (12,10) active space, the two lowest lying 3s Rydberg orbitals associated with the O atoms were included in the larger (12,12) active space. The Rydberg orbitals were identified by looking for a large 3s component (smallest exponent on s-type basis function centred on oxygen) in the original Hartree-Fock ground state trial orbitals.

The PECs of the excited and ground electronic states of the two active conformers of resorcinol were calculated using CASPT2 performed with Molpro. As before, geometry optimisation was first performed using CASSCF with a (12,12) active space and the aug-cc-pVTZ basis set. PECs were produced along all three O–H coordinates (two coordinates in the A conformer and a single coordinate in B due to symmetry considerations - see structures in Figure 3.1). The bond was

extended from the ground state equilibrium position to a distance of 4 Å (at which point the surfaces become asymptotic) then stepped back to 0.6 Å at varying intervals of internuclear separation, $\boldsymbol{R}$. Energies for each of the levels, S_0, $1^1\pi\pi^*$, $^1\pi\sigma^*$, and the lowest Rydberg state were then calculated for each step. At each point, only the O–H bond length was altered, all other geometric parameters being held constant, resulting in unrelaxed PECs.

3.3   Results and Analysis

3.3.1   *Ab initio* Calculations

a. Vertical excitation energies and torsional barriers

Table 3.1 collates the vertical excitation energies, resulting from TD-PBE0, EOM-CCSD and CASPT2 calculations, as well as the oscillator strengths (f) from the TD-PBE0 and EOM-CCSD. An experimental value for the $1^1\pi\pi^*$ origin is also included for comparison. Reasonable agreement can be seen between the TD-PBE0 and EOM-CCSD calculations, with the EOM-CCSD vertical excitation values more closely matching experiment, although still over estimating the $1^1\pi\pi^*$ origin by $\sim$0.53 eV. The vertical excitation value for the first excited state as extracted *via* CASPT2 calculations follow the experimental values much more closely, giving a difference of <0.01 eV for conformer A and $\sim$0.06 eV for conformer B. Table 1 also shows the bond dissociation energies (BDEs) for each of the three possible O–H coordinates across the two conformers (A and B) present in the molecular beam. The O^1–H coordinate has the lowest BDE value, followed by the O^2–H and finally the O^3–H coordinate (see Figure 3.1 for O–H coordinate labels), calculated at the PBE0/aug-cc-pVTZ level of theory. Further TD-PBE0/aug-cc-pVTZ calculations were also performed to determined the torsional barriers to interconversion between conformers A/B and A/C in the excited $1^1\pi\pi^*$ state, returning barrier heights of 2126 cm^{-1} and 1980 cm^{-1} (relative to the $1^1\pi\pi^*$ origin) for switching between conformers A/B and A/C, respectively (not presented in Table 3.1).

b. Potential energy cuts and conical intersections

The PECs for the three pertinent O–H coordinates ($R_{O^n–H}$) are shown in Figure 3.2. These cuts demonstrate the dissociative nature of the $^1\pi\sigma^*$ state(s) with characteristics similar to those seen in other phenol derivatives.[4,20] In all three O–H stretch coordinates, a barrier is formed *via* a CI between the $1^1\pi\pi^*$ and $^1\pi\sigma^*$ states which must be overcome, or tunnelled through, for dissociation to occur. This barrier height is lowest along the O^1–H coordinate, having a value of 5330 cm^{-1}. The barrier heights to H atom tunnelling along the O^2–H and O^3–H coordinates are 6590 cm^{-1} and 6017 cm^{-1}, respectively. Calculations for tunnelling probabilities were performed based on the CASPT2 PECs using the Wentzel-Kramers-Broullian (WKB) method,[21] producing values of 1.2×10^{-3}, 1.9×10^{-5} and 2.1×10^{-4},

Table 3.1: Calculated vertical excitation energies (ΔE_{vert}) and oscillator strengths (f) for resorcinol at the TD-PBE0/aug-cc-pVTZ, EOM-CCSD/ aug-cc-pVDZ and CASPT2/aug-cc-pVTZ. Bond dissociation energies, BDEs, calculated at the PBE0/aug-cc-pVTZ level are also provided. The experimental value for the first excited state of conformers A and B is also presented for comparison. O^n–H labels from Figure 3.1

ΔE_{vert} / eV (f)				
State	TD-PBE0	EOM-CCSD	CASPT2	Expt[a]
Conf. A				
$1^1\pi\pi^*$	5.08 (0.0339)	4.99 (0.0255)	4.45	4.46
$1^1\pi\sigma^*$	5.23 (0.0004)	5.43 (0.0003)	5.46	
$2^1\pi\sigma^*$	5.48 (0.0000)	5.72 (0.0001)	—	
$2^1\pi\pi^*$	5.81 (0.0091)	6.12 (0.0200)	5.64	
Conf. B				
$1^1\pi\pi^*$	5.11 (0.0252)	4.99 (0.0179)	4.43	4.49
$1^1\pi\sigma^*$	5.23 (0.0000)	5.41 (0.0000)	5.50	
$2^1\pi\sigma^*$	5.49 (0.0011)	5.70 (0.0006)		
$2^1\pi\pi^*$	5.78 (0.0068)	6.08 (0.0202)		

BDE / cm^{-1}	
Co-ord	PBE0
O^1-H	28930
O^2-H	29340
O^3-H	29360

[a] Reference 7

respectively. We return to discuss the potential significance of these tunnelling probabilities in Section 3.4.

Continuing to follow increasing O–H bond lengths, once through the barrier a second CI is formed between the $^1\pi\sigma^*$ and S_0 states which allows dissociation through either adiabatic (in the $\tilde{A}$ state of the $C_6H_5O_2$ radical, plus an H atom) or non-adiabatic (to the ground $\tilde{X}$ state in the $C_6H_5O_2$ radical, plus an H atom) pathways. Internal conversion (IC) can also occur at the CI back to higher lying vibrational modes in the ground state (S_0*) of the parent molecule, in which case dissociation can take place through statistical unimolecular decay.[22] It should be noted that the O^2–H and O^3–H coordinates should converge to the same radical states. However, this is not the case here and is attributed to the unrelaxed nature of the calculations performed. This has been verified by performing geometry optimisations, at the TD-PBE0/aug-cc-pVTZ level, on the two radical products which do indeed optimise to the same asymptote.

Also presented in Figure 3.2 are the calculated gradient difference (GD) and derivative coupling (DC) branching space motions associated with the MECPs of the CIs (See Section 1.3.3). Interestingly, unlike phenol, which conforms to a non-rigid G_4 (isomorphous with C_{2v}) symmetry due to torsional tunnelling,[23,24] such
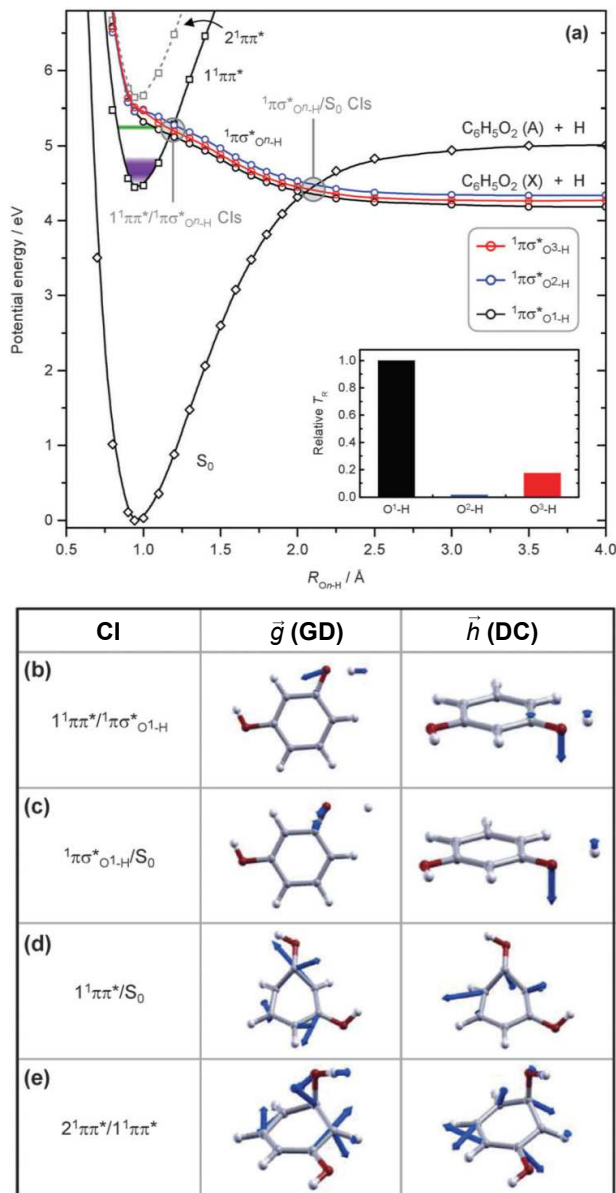
Figure 3.2: (a) Calculated 1D potential energy cuts of the S_0, $1^1\pi\pi^*$ and $^1\pi\sigma^*$ electronic states along the O^1–H (black circles), O^2–H (blue circles) and O^3–H (red circles) bond dissociation coordinates (R_{O^n-H}) in resorcinol (see Figure 3.1). Cuts are calculated at the CASPT2(12,12)/aug-cc-pVTZ level. Shaded areas indicate the excitation regions for the range 278 – 255 nm (purple) and 237 nm (green). Also included is the $2^1\pi\pi^*$ (grey squares) which is based upon the calculated profile for the $1^1\pi\pi^*$ and corrected to the CASPT2 vertical excitation energy value for conformer A (see Table 3.1). Inset: relative tunnelling probabilities, T_R, for the three O^n–H coordinates as calculated using the WKB method. Right are shown calculated gradient difference (GD) and derivative coupling (DC) branching space motions associated with the CI geometries for the minimum energy crossing points between (b) $1^1\pi\pi^*/^1\pi\sigma^*_{O^1-H}$, (c) $^1\pi\sigma^*_{O^1-H}/S_0$, (d) $1^1\pi\pi^*/S_0$ and (e) $2^1\pi\pi^*/1^1\pi\pi^*$.

symmetry constraints are not applicable in resorcinol, an observation that has also been noted in a recent study on 4-substituted phenols.[25] As a result, the lower C_s symmetry of both conformers A and B at extended O–H distances means that non-adiabatic coupling is driven by O–H torsional motion (rather than the ν_{16a}

vibration, as posited in phenol[20,25]), as evidenced in the branching space motions for both the $1^1\pi\pi^*/^1\pi\sigma^*$ and $^1\pi\sigma^*/S_0$ CIs along O^1–H in Figure 3.2(b) and (c), respectively. A similar branching space is observed for these CIs along the O^2–H and O^3–H coordinates.

In addition to the CIs involving the $^1\pi\sigma^*$ states, CASSCF calculations with a smaller (10,8) active space also reveal CIs between the $2^1\pi\pi^*$, $1^1\pi\pi^*$ and S_0 surfaces, which lie along coordinates orthogonal to O–H stretch coordinates presented in Figure 3.2(a). In Figure 3.2(d) the MECP of a prefulvenic-type CI, which links the $1^1\pi\pi^*$ and S_0 states, is presented. The calculated branching spaces are akin to those previously determined for the prefulvene CI in benzene, which is responsible for the so-called 'channel 3' decay pathway.[26] The CI structure presented in Figure 3.2 is the lowest energy of a number of prefulvenic-type CIs that we have identified in resorcinol (varying in the location of the characteristic 'C–H kink' on the phenyl ring and the relative orientations of the O–H groups), all of which lie between $\sim$7000 – 8000 cm^{-1} above the $1^1\pi\pi^*$ origin at the CASSCF(10,8)/6-31G* level. For comparison, the prefulvene CI in phenol was previously calculated to lie $\sim$6400 cm^{-1} above the $1^1\pi\pi^*$ origin at the MRCI/aug-cc-pVDZ level.[27] Finally, Figure 3.2(e) presents the MECP of a CI between the $2^1\pi\pi^*$ and $1^1\pi\pi^*$ states. The structure of this MECP and associated branching space motions are similar to a $2^1\pi\pi^*/1^1\pi\pi^*$ CI identified in another heteroaromatic species, aniline (aminobenzene),[28] and as in that case, may offer a pathway for rapid population transfer from $2^1\pi\pi^*$ to $1^1\pi\pi^*$.

3.3.2   Time-resolved Ion Yield: $\lambda = 278 - 255$ nm

a. Resorcinol

TR-IY experiments provide insight into the dynamics that take place in the excited state following excitation with UV radiation. By probing the parent resorcinol$^+$ ion as a function of Δt, we are able to observe the $1^1\pi\pi^*$ population decay (from FC$_{vert}$) through all available relaxation pathways (*e.g.* fluorescence, IC, tunnelling, *etc.*) and, with reference to the above theoretical work, provisionally assign the origins of the measured lifetimes.

The left column of Figure 3.3(a-f) shows the resorcinol$^+$ signal transients obtained from TR-IY experiments (open circles). Upon cursory inspection it can be seen that each of the transients possess an initial sharp rise followed by an exponential decay. Where the temporal limit of the experiment has been sufficient to span the entire $1^1\pi\pi^*$ lifetime, the decay returns asymptotically to the baseline. In order to extract time constants for the $1^1\pi\pi^*$ lifetime from each transient, a kinetic fit was performed (blue line), consisting of an exponential decay function convoluted with our Gaussian IRF ($\sim$120 fs FWHM). Further information regarding our fitting procedures can be found in Appendix A. It can be seen from the fits that the transients are mono-exponential, with the exception of the 264 and 260 nm transients (Figure 3.3(d) and (e)), providing us with a time-constant for

the lifetime of the $1^1\pi\pi^*$ state (τ_1). The transients at pump wavelengths 264 and 260 nm required a bi-exponential decay in order to be fit accurately, producing two time-constants within the kinetic fit, τ_1 and τ_2, the origins of which we discuss in further detail below.

Simply by analogy with previous work,[1,20,29] one would be inclined to assign τ_1 to correspond to population decay *via* a tunnelling mechanism following the $1^1\pi\pi^*$ $\rightarrow {}^1\pi\sigma^* \rightarrow C_6H_5O_2(\tilde{X}) + H$ pathway. At $1^1\pi\pi^*$ ($\nu=0$), we observe a timescale of $\tau_1 \approx 2.7$ ns which is certainly within the timescales one would expect when compared with the tunnelling timescale determined experimentally for phenol ($\sim$2.4 ns from Reference 30). However, were tunnelling the only process by which population could be removed from $1^1\pi\pi^*$, we might expect τ_1 to remain independent of excitation energy (see Section 3.3.3a below).[4] Contrary to this however, as the excess energy imparted into the system increases (increasing $h\nu_{pu}$), we see a concurrent decrease in the $1^1\pi\pi^*$ lifetime by approximately one order of magnitude as the pump wavelength decreases from 278 – 255 nm. Behaviour akin to this was also observed in TR-IY experiments performed on parent phenol$^+$ and was assigned to a process wherein population was transferred back to the vibrationally excited ground state, termed S_0^*, by IC.[4] The fact that we see a decrease in τ_1 with decreasing wavelength is consistent with an IVR driven IC process following a Fermi's
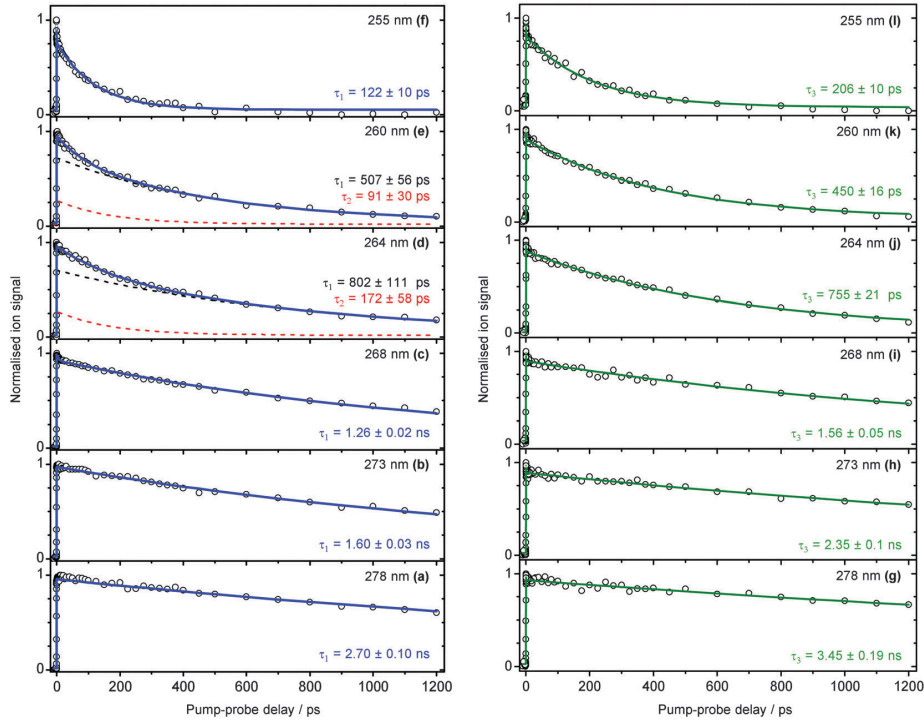
Figure 3.3: (a-f) Parent ion (resorcinol$^+$) and (g-l) deuterated parent ion ([resorcinol-d_2]$^+$) signal transients. Transients were recorded using [1+1'] REMPI following excitation at a range of pump wavelengths between 278 – 255 nm and probing at 243.1 nm. Solid lines correspond to kinetic fits. In (d) and (e), dashed red and black lines show components of bi-exponential fits. Extracted timescales are displayed next to the relevant parent ion trace.

golden rule like argument (See Chapter 1, Section 1.2.3).[31] We return to discuss this latter point in Section 3.4 below.

b. Resorcinol-d_2

As well as the TR-IY data collected for resorcinol, we also performed complementary investigations on the doubly deuterated species, resorcinol-d_2. Figure 3.3(g-l) shows the 243 nm probed [resorcinol-d_2]$^+$ parent ion as a function of Δt for the same range of wavelengths as those studied in non-deuterated resorcinol. It can be seen that the curves display the same basic behaviour as was observed in non-deuterated resorcinol; an initial sharp rise ($\Delta t = 0$) which then decays exponentially with some lifetime, τ_3, which decreases with increasing energy. Values were extracted for τ_3 *via* the application of kinetic fits as described previously (Section 3.3.2a).

For all wavelengths investigated, τ_3 is slower than, or comparable to, τ_1 within the error of the fits. This behaviour is consistent with the $1^1\pi\pi^*$ state in non-deuterated resorcinol decaying *via* competing mechanisms including tunnelling; the increased mass of the D atom significantly reduces the tunnelling probability (*cf.* phenol[4,20]) compared to H atom tunnelling, effectively deactivating this relaxation channel from the $1^1\pi\pi^*$ state. At higher excitation energies the values for τ_3 in general become more comparable to the τ_1 value for the equivalent wavelength as, at these energies, the rate of IC is significantly greater than that of tunnelling and so the $1^1\pi\pi^*$ lifetime is relatively unaffected by the deactivation of the tunnelling pathway.

Perhaps the most striking difference brought about by deuteration is that every transient is now mono-exponential in nature, requiring only one time constant in order to fit the long decay accurately. This allows us to suggest that whatever process is responsible for τ_2 is made orders of magnitude slower, or turned off entirely, by deuteration of the sample, possibly suggesting a second tunnelling mechanism is accessible at these energies. We return to discuss the origins of each of the discussed time constants in further detail in Section 3.4.

3.3.3 Time-resolved H$^+$ Velocity Map Imaging: $\lambda = 278 - 255$ nm

a. TKER spectra

Figure 3.4 shows the TKER data collected over a probe wavelength range of 278 - 255 nm (filled circles), as derived from H$^+$ images such as the 273 nm example shown inset, following excitation to the $1^1\pi\pi^*$ state. All spectra and images were recorded at $\Delta t = 1.2$ ns. In order to remove unwanted one colour contributions, an image collected at negative time, corresponding to the pump alone and probe alone signals, is subtracted from each image. The left half of the example image shows the raw image, while the right half shows the same image after deconvolution with the POP algorithm. From the deconvoluted image we can see the dominant contribution is a single, high intensity ring at large radii which is isotropic with respect
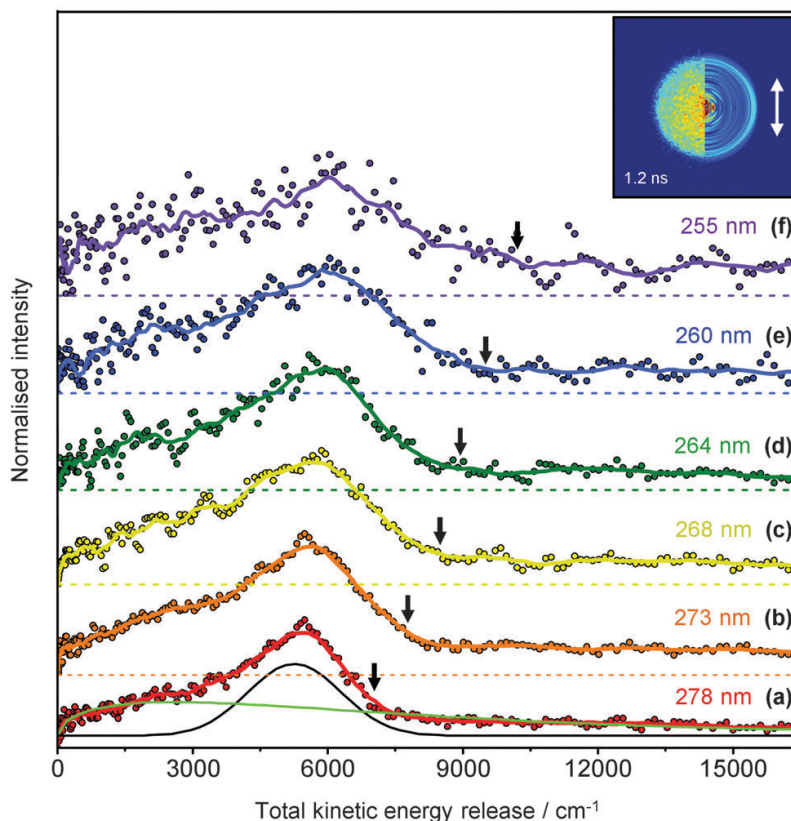
Figure 3.4: H atom TKER spectra collected over a pump wavelength range of 278 – 255 nm, (a-f) respectively. Vertical black arrows indicate the predicted TKER$_{max}$ for $^1\pi\sigma^*$ mediated dynamics. Inset: example H$^+$ velocity map image from which the TKER spectra are derived (left half) together with a reconstructed slice through the centre of the original 3D ion distribution (right half). The vertical white arrow indicates the electric field polarisation of the pump pulse, ε_{pu}. Spectrum (a) has been fit to a Boltzmann background signal (green solid line) and a Gaussian peak (black solid line) corresponding to C$_6$H$_5$O$_2$ radical production.

to the pump laser polarisation (ε), as shown by the white arrow. The isotropic nature of this feature is suggestive of H atom elimination occurring on a timescale slower than the time required for rotational dephasing. As mentioned above, from the collected H$^+$ images we can extract corresponding TKER spectra, as plotted in Figure 3.4(a-f). Each spectrum exhibits two distinct features - a low TKER, 'Boltzmann like' distribution and a higher energy Gaussian signal. These two features are highlighted by the fits applied to the 278 nm spectrum: the green line represents the Boltzmann background and the black line is the Gaussian contribution. The lower lying signal has been assigned previously in related heteroaromatic species to statistical or multiphoton processes.[4,22] This feature is not the focus of this work and as such shall not be discussed further in this chapter. We turn our attention instead to the signal at high ($\sim$5000 cm^{-1}) TKER. A well-defined Gaussian signal such as this is characteristic of H atoms produced by $^1\pi\sigma^*$ mediated processes, as has been observed in previous experiments.[32–35] By analogy with phenol and cate-

71

chol, we provisionally assign the appearance of this signal to dissociation along the $^1\pi\sigma^*$ state preceded by tunnelling beneath the $1^1\pi\pi^*/^1\pi\sigma^*$ CI.

In order to further elucidate as to whether this feature is indeed related to dissociation along the $R_{\text{O–H}}$ coordinate, we can consider the energetics of the dissociation process. Due to the presence of the two separate conformers, it is possible that all 3 O^n–H coordinates are able to dissociate in order to produce H atoms. By taking the O^1–H coordinate value for BDE,[i] as calculated using the PBE0 functional ($\sim$28930 cm^{-1}), we are able to calculate a value for the theoretical maximum kinetic energy (TKER$_{max}$) for H atoms born through an $R_{\text{O–H}}$ dissociation process. For each of the pump wavelengths, the calculated TKER$_{max}$ is shown by the small black arrow above the spectra. At the $1^1\pi\pi^*$ origin (278 nm) a photon energy, $h\nu_{\text{pu}}$, of 35971 cm^{-1} yields an estimated TKER$_{max}$ of $\sim$7000 cm^{-1} in line with the observed TKER cut-off point. As the amount of excess energy imparted into the system increases, we might expect that the TKER$_{max}$ increases in the same manner, however, we see very little difference in the spectra. There is only a very slight shift ($\sim$500 cm^{-1}) in the TKER of maximum intensity between 278 and 255 nm. Similar behaviour was observed in phenol and catechol, and was ascribed to a mechanism wherein tunnelling occurs solely from the zero-point energy of the $1^1\pi\pi^*$ state, while the majority of the excess energy occupies vibrational "spectator" modes, orthogonal to the $R_{\text{O–H}}$ coordinate.[4,29] The above evidence leads us to assign the origins of this high TKER signal to the appearance of H atoms born *via* tunnelling beneath the $1^1\pi\pi^*/^1\pi\sigma^*$ CI as concluded by Livingston *et al.* in their earlier TR-PEI experiments.[1]

It is also worth noting that as a function of increasing $h\nu_{\text{pu}}$, we see a large decrease in signal to noise ratio of the recorded images. It is likely that this decrease in H atom signal is a result of a corresponding decrease in the quantum yield for H atoms born through dissociative processes at shorter wavelengths, coupled with a decreasing photoabsorption cross-section. We believe this is another possible indication that the process by which O–H bond rupture occurs is in direct competition with a non-dissociative process, such as IC, that is capable of removing population from $1^1\pi\pi^*$ before tunnelling onto S_2 can take place. This complements the conclusions drawn from the TR-IY experiments in Section 3.3.2, showing that IC is in fact an important relaxation process that is in direct competition with the tunnelling mechanism.

b. H$^+$ Signal Transients

By collecting a series of TKER spectra as a function of Δt between -1 ps and 1.2 ns and integrating over the relevant TKER range, we are able to produce time-resolved plots for the appearance of a particular feature. Figure 3.5 shows normalised H$^+$

---

[i]O^1–H is selected as it has the lowest value for the BDE and will therefore yield the highest value TKER$_{max}$.
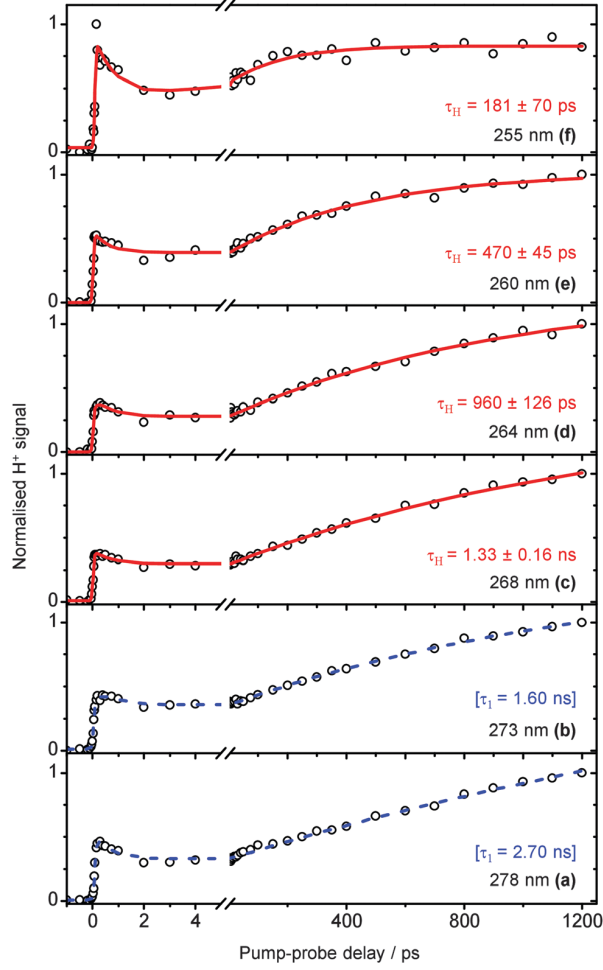
Figure 3.5: (a-f) Normalised H^+ signal transients for the high TKER (Gaussian) feature at each pump wavelength obtained by integrating the signal between 3000 – 8000 cm^{-1} in TKER spectra recorded at many Δt. A kinetic fit to the trace is shown by the solid red line with extracted time constant (τ_H) displayed beneath. For panels (a) and (b), the transients are fit with the time constant extracted from the resorcinol$^+$ transient (τ_1, dashed blue line), see text for more details.

signal transients generated by integrating the TKER signal over the range 3000 – 8000 cm^{-1} (open circles) for all wavelengths studied. As described above, the image at each Δt has a negative time image subtracted before deconvolution, to remove unwanted one-colour signal. Each transient has the same basic structure; before $\Delta t = 0$ the probe beam precedes the pump beam and we observe very little H^+ signal, in line with the fact that the pump is unable to resonantly ionise any released H atoms. At $\Delta t = 0$ we see a sharp rise and decay ($<$1 ps) corresponding to the appearance of the small multiphoton background signal and finally, a slow ($>$100 ps) exponential rise at long times, assigned to the appearance of the high TKER H atoms formed through a $1^1\pi\pi^* \rightarrow {}^1\pi\sigma^* \rightarrow C_6H_5O_2(\tilde{X})$ + H pathway *via* tunnelling below the $1^1\pi\pi^*/^1\pi\sigma^*$ CI.

Again, we can apply kinetic fits to the recorded data in order to acquire values for the timescale of the ensuing H atom dynamics. In this case each fit consists of two exponential rise functions and one exponential decay function. The sharp

rise and decay functions correspond to the faster multiphoton signal. The slow rise function corresponds to the appearance of high KE H atoms. All functions are convolved with our IRF. It is worth noting that, for the two longest wavelengths recorded, 278 and 273 nm, the dynamics are incomplete within the temporal limit of our experiments ($\sim$1.2 ns) and so, in order to provide an approximate value for the lifetime, these transients have restricted fits applied to them (blue, dotted line) using the decay timescale acquired from the parent ion at these wavelengths (see Figure 3.3). The remaining wavelengths, 268 – 255 nm, plateau, or begin to, inside the experimental temporal window and as such are entirely free fit (red, solid line).

The time constant (τ_H) for the high TKER component extracted from the kinetic fits is shown in red next to the relevant transient. The decrease in lifetime of O–H bond scission, evident from these results, agrees favourably with the decrease in τ_1 seen in the TR-IY experiments (Section 3.3.2). This increased rate of H atom production, in conjunction with the decrease in quantum yield witnessed in the TKER spectra, further supports our proposal that we are observing competing deactivation mechanisms. In previous studies on phenol, such a correlation between TR-IY measurements of the phenol$^+$ transient and the rate of H atom production was not evident. Indeed, H$^+$ transients modelled by a constant value for the rate of H atom production resulted in a reasonable (within signal-to-noise) fit, irrespective of increasing excitation energy. The phenol$^+$ transients, however, displayed a decreasing time constant as expected. Retrospectively, we attribute this to combined effects: (1) the poor signal to noise of our H$^+$ transients, especially at the shorter excitation wavelengths where the absorption cross-section falls considerably in contrast to the much improved signal-to-noise attained in resorcinol; (2) the fact that none of the H$^+$ transients in phenol were showing any conclusive evidence of H$^+$ signal plateauing within the temporal window of the experiment, whereas this is only apparent for the two lowest energy transients in resorcinol; (3) the reduced rate of increase in density of states (see Section 3.4) in phenol within the excitation wavelength range. Both (1) and (2) have enabled us to extract more reliable time constants, τ_H, from resorcinol, which follows τ_1 whilst (3) may tentatively suggest why the decreasing time constants extracted from phenol$^+$ transients are not as pronounced as in resorcinol$^+$ transients to strongly influence the associated H$^+$ transients. Combined, the H$^+$ transients in phenol do not show as marked a change in the H atom production with increasing excitation energy.

3.3.4   Time-resolved H$^+$ Velocity Map Imaging: $\lambda = 237$ nm

Following excitation at 237 nm (5.23 eV) we see a new relaxation pathway become accessible. As can be seen from Figure 3.1, at these energies, a new absorption feature begins to appear, likely corresponding to the onset of the $2^1\pi\pi^*$ state (see Table 3.1). While we calculate the vertical excitation energy of this state to be 5.64 eV at the CASPT2 level, the $2^1\pi\pi^*$ state will likely have a significantly different minimum energy geometry to that of the S_0 state, resulting in some minimal ab-
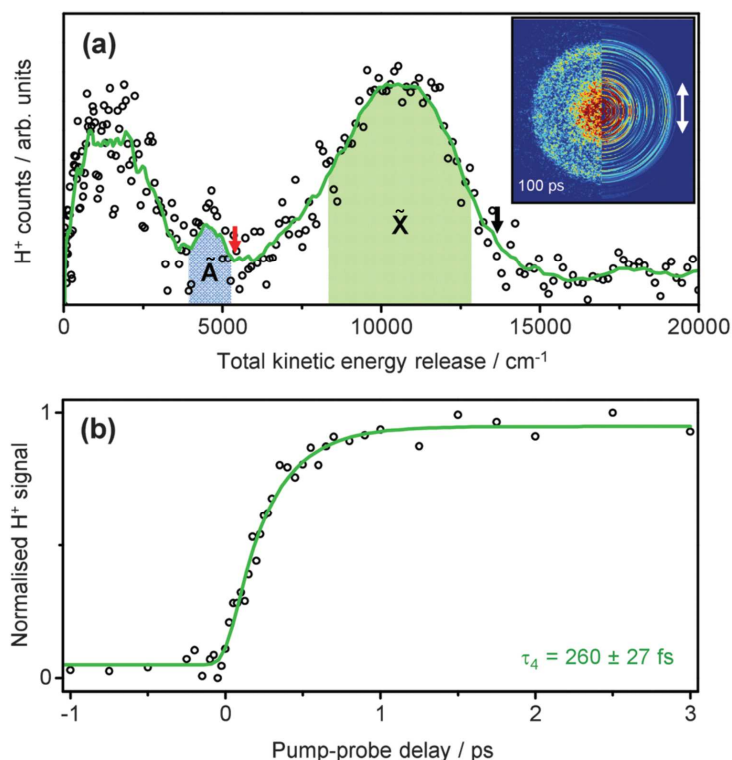
Figure 3.6: (a) H atom TKER spectrum obtained following excitation at 237 nm, showing a peak at $\sim$11000 cm^{-1} corresponding to production of $\tilde{X}$ state resorcinoxyl radicals (shaded green) and one at $\sim$4000 cm^{-1} corresponding to $\tilde{A}$ state radical production (shaded blue). Predicted TKER$_{max}$ values for dissociation into the $\tilde{X}$ and $\tilde{A}$ state product channels are shown by the vertical black and red arrows, respectively. Inset: H$^+$ velocity map image from which the TKER spectrum is derived (left half) together with a reconstructed slice through the centre of the original 3D ion distribution (right half). (b) H$^+$ signal transient following excitation with 237 nm light (circles), obtained by integrating the signal between 8000 – 14000 cm^{-1} in TKER spectra recorded at various Δt. An overall kinetic fit to the trace is shown by the solid green line with the extracted time constant (τ_4) below.

sorption cross-section extending into longer wavelengths (*cf.* findings from previous studies on para-methoxyphenol[32] and aniline[28]). Figure 3.6 shows an H$^+$ image (inset (a)) and TKER spectrum (a) collected at $\Delta t = 100$ ps following photoexcitation with $h\nu_{\mathrm{pu}} = 237$ nm. As with images and spectra collected at longer wavelengths, both have had a background image subtracted in order to remove any unwanted one-colour signal. The image is much the same as seen previously, consisting of a "noisy" central signal and a higher intensity ring at larger radii. The key difference at this wavelength is that the high intensity ring appears at a larger radius than observed previously. This implies that H atoms are being generated with higher KE compared to excitation below the $1^1\pi\pi^*/^1\pi\sigma^*$ CI, allowing us to preliminarily suggest that O–H bond dissociation occurs from a higher lying excited state.

The structure of the spectrum is qualitatively similar to that seen for the lower excitation energies; a broad Boltzmann-like background, extending across the entire spectrum, and a higher lying Gaussian signal at $\sim$11000 cm^{-1}. Similarly to previous

arguments, the presence of a broad symmetric Gaussian signal at high TKER is often indicative of H atoms formed through $^1\pi\sigma^*$ driven processes. To verify this we must refer once again to the PECs in Section 3.3.1b.

On energetic grounds, when exciting with 237 nm light ($\sim$6200 cm^{-1} above the $1^1\pi\pi^*$ origin), the PECs indicate that we are exciting to the region close to the dissociative $^1\pi\sigma^*$ state ($\sim$8000 cm^{-1} above the $1^1\pi\pi^*$ origin). As before, we can calculate the theoretical TKER$_{max}$ for a feature arising from this point on the potential curve. Following excitation with $h\nu_{\mathrm{pu}} = 42194$ cm^{-1}, the calculation yields a TKER$_{max}$ value of $\sim$13500 cm^{-1} which is in excellent agreement with the TKER cut off point for the high TKER feature.

The H$^+$ signal transient for this feature, integrated over 8000 – 14000 cm^{-1}, is shown in Figure 3.6(b). An extracted timescale of 260 fs indicates the presence of an ultrafast process such as direct dissociation from the $^1\pi\sigma^*$ state or ultrafast coupling between the $1^1\pi\pi^*$ (or higher lying $2^1\pi\pi^*$ state) and $^1\pi\sigma^*$ state followed by dissociation, mediated by the appropriate CIs shown in Figure 3.2. This compares very favourably with the results for excitation above the $1^1\pi\pi^*/^1\pi\sigma^*$ CI witnessed in catechol.[29]

Interestingly, another feature observed in the TKER spectrum is a second, much less intense Gaussian signal centred at $\sim$4200 cm^{-1}. It is tentatively suggested that this feature corresponds to H atoms formed in conjunction with excited $\tilde{A}$ state resorcinoxyl radicals (see Figure 3.2). This conclusion is supported by consideration of the energetics for this dissociation channel. The experimentally measured splitting between the $\tilde{A}$ and $\tilde{X}$ states of the resorcinoxyl radical is 8100 cm^{-1},[36] returning a predicted TKER$_{max}$ of $\sim$5200 cm^{-1} for the $\tilde{A}$ state channel (vertical red arrow in Figure 3.6), in excellent agreement with the location of the smaller Gaussian feature. Unfortunately we were unable to extract a transient from this peak due to both the poor signal-to-noise and the overlapping Boltzmann and Gaussian feature arising from the $\tilde{X}$ state radical.

3.4 Discussion

3.4.1 Competing Dynamics

It was seen in the TR-IY experiments that the rate of population transfer from the $1^1\pi\pi^*$ excited state is highly dependent on the excitation energy. As mentioned previously, this is as we might expect for an IVR driven IC process following a Fermi's golden rule-like argument. In terms of the system in question, the density of states (DOS) in the final S_0^* state in the IC process (as would normally be the case in Fermi's golden rule), will be relatively constant across our excitation window (278 – 255 nm) and have little impact on the rate of IC. Instead, we consider the DOS in the excited $1^1\pi\pi^*$ state (presented in Figure 3.7). As $h\nu_{\mathrm{pu}}$ increases, the DOS accessed in $1^1\pi\pi^*$ grows, resulting in a greater propensity for IVR into out-of-plane vibrational modes which can more efficiently promote IC back to S_0^* and

reduce the overall $1^1\pi\pi^*$ lifetime.This appears to be akin to the well-known 'channel 3' decay mechanism in benzene, $\sim$3000 cm^{-1} above its $1^1\pi\pi^*$ state origin.[37–40] Indeed, the decreased lifetime at $h\nu_{\mathrm{pu}} = 255$ nm ($\sim$3200 cm^{-1} excess internal energy in $1^1\pi\pi^*$) here in resorcinol may be due to an analogous 'channel 3'-like decay process, which drives population towards a prefulvenic $1^1\pi\pi^*/S_0$ CI, such as that presented in Figure 3.2(d). However, it should be noted that time-resolved studies in benzene have shown that this mechanism generally manifests itself with lifetimes on the order of picoseconds or sub-picoseconds,[41–44] whereas the excited $1^1\pi\pi^*$ state lifetime observed in these studies is never less than hundreds of picoseconds - orders of magnitude slower than in benzene, thus leading us to discount this hypothesis. It is perhaps also worthwhile noting that an IVR driven IC process such as that described above, is likely to be a highly entropically favoured pathway. Given that the system is able to couple to a significantly increased number of states in S_0*, it is possible that the vibrational energy can be distributed over a much larger number of states, therefore greatly increasing the entropy of the system. Thus, from these arguments we can tentatively assign τ_1 to a $1^1\pi\pi^*$ decay process involving competing dynamics between H atom tunnelling and IVR driven IC.

In an attempt to verify this argument, Figure 3.7 shows a comparison plot of the DOS in the $1^1\pi\pi^*$ state for resorcinol and the rate of $1^1\pi\pi^*$ depopulation as a function of excess internal energy in $1^1\pi\pi^*$ (E_{vib}). The DOS in the $1^1\pi\pi^*$ state was derived from the calculated CASSCF harmonic frequencies in $1^1\pi\pi^*$ using an extended Beyer-Swinehart method described in Reference 45. k_x represents the rate of depopulation through the different identified pathways; $1/\tau_1$ (blue circles), $1/\tau_2$ (black diamonds) and $1/\tau_H$ (red squares). As stated previously τ_1 and τ_H compare very well and, for the most part, there is a reasonable correlation between both k_1 and k_H and the calculated DOS for either conformer (shown by the solid grey and red lines). This leads us to assume that we are observing a DOS driven process which, in this specific case, is most likely to be IVR driven IC back to the electronic ground state. The above evidence, coupled with our arguments made in Section 3.3.3, further supports our postulate that τ_1 is a combination of IC, in direct competition with H atom tunnelling.

Figure 3.7 also presents the DOS calculated for phenol in $1^1\pi\pi^*$ (grey dashed line). The rate of increase of DOS with increasing excess energy is greatly reduced compared to that of either resorcinol conformer. As such, the increase in the rate of IC is likely to be less pronounced in phenol, which accords well with our observation of longer excited state lifetimes extracted from TR-IY measurements of the parent phenol$^+$ transient.[4] As such, the $1^1\pi\pi^*$ lifetime would appear to remain constant within our excitation wavelength range, in contrast to the behaviour observed in resorcinol.
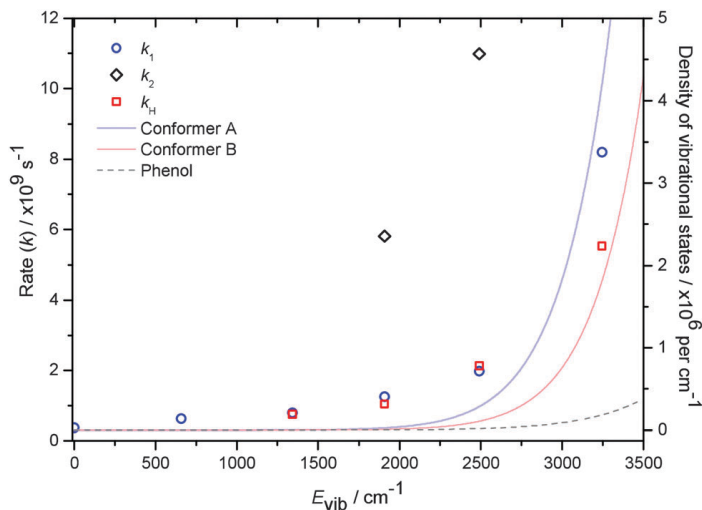
Figure 3.7: Calculated density of vibrational states in the $1^1\pi\pi^*$ state of resorcinol for conformers A (grey line) and B (red line), and phenol (grey dashed line). Also shown are the measured rates of decay of the $1^1\pi\pi^*$ state, k_1 (blue circles) and k_2 (black diamonds) - and of H atom appearance, k_H (red squares) - in resorcinol, plotted as a function of excess vibrational energy in the $1^1\pi\pi^*$ state, E_{vib}.

3.4.2 Origins of τ_2

In contrast to τ_1, the origins of τ_2 are more difficult to assign. We first look to collate the evidence involving τ_2 and then attempt to resolve its origins. From the [resorcinol-d_2]$^+$ TR-IY transients it can be seen that, following deuteration, τ_2 is no longer an accessible pathway. This therefore implies that the process responsible for τ_2 is likely to be barriered in some way since deuteration will greatly reduce the probability of tunnelling through this barrier. This proposal is also supported by the extracted lifetimes for τ_2 (see Figure 3.3(d-e)), which are typical of a non-ballistic (non-ultrafast) process. It should also be noted that, while the resorcinol$^+$ transient collected at 255 nm probe wavelength displays mono- rather than a bi-exponential character, the time constant extracted at this wavelength is similar to the values for τ_2 extracted at 264 and 260 nm. As such, it is very difficult to ascertain whether there is truly only a single relaxation process being probed at 255 nm or if two processes of a similar rate are occurring simultaneously.

From the above arguments, several conclusions can be drawn. First of all, as a single exponential fit alone is necessary for all τ_H which correlates with τ_1, it is unlikely that the mechanism that results in τ_2 is in direct competition with H atom tunnelling / IC. This would make IVR seem the most straightforward explanation. However the timescales involved cast doubt over this conclusion. IVR generally onsets when the density of states accessed is $\sim$100 per cm^{-1},[46] which, from our DOS calculations, occurs in resorcinol at $\sim$800 cm^{-1} excess energy. Above this threshold, the rate of IVR is expected to increase with increasing energy, following a similar density of states argument as presented for IC above. This limit is greatly exceeded at the energies at which τ_2 onsets. Given that our observed timescales are

on the order of tens to hundreds of ps and that this time component activates ∼1900 cm^{-1} above the $1^1\pi\pi^*$ origin, it is unlikely that such an IVR process is responsible for the bi-exponential decay observed here. In addition, whilst we concede that timescales for IVR on the order of a hundred picoseconds have been observed in benzene previously,[47] the enhanced DOS through additional functional groups in resorcinol will likely result in an increased rate of IVR.

We can also rule out a mechanism associated with a prefulvenic CI within resorcinol. Prefulvenic CIs in phenol are known to exist ∼6400 cm^{-1} above the $1^1\pi\pi^*$ origin[27] and, given the similarities between phenol and resorcinol, it is reasonable to assume the prefulvenic CIs will reside in approximately the same energetic location (see Figure 3.2(d)). Taking this assumption into account, it is unlikely that prefulvenic CIs are responsible for τ_2, as the onset occurs at ≥264 nm (∼1900 cm^{-1} excess energy).

Given that the deuterated data show no τ_2 component, any alternative suggestions must point towards a barriered process. Armed with this knowledge, we provide two suggestions for the origins of τ_2:

(1) a keto-enol tautomerisation (KET) mechanism, involving either one or both OH groups. Such a process would likely need to overcome, or tunnel through a barrier before tautomerisation could occur.[48,49] Previous experiments have placed the vibrational modes that would likely mediate the KET mechanism, which include the O–H bend, at ∼1300 cm^{-1} in the ground state of resorcinol.[5,7] A similar excess energy would be expected for the O–H bend in the $1^1\pi\pi^*$ excited state which is in fairly good agreement with the onset of τ_2 (>1900 cm^{-1}). To verify this proposed mechanism, appropriate methylation at carbon positions adjacent to C–OH, would prevent KET. Assuming that methylation does not influence the electronic structure significantly, this may assist in validating such a KET mechanism.

(2) The second explanation derives from consideration that conformer C (inset Figure 3.1) may be participating in the excited state dynamics. While conformer C has not been spectroscopically observed in previous experiments, τ_2 is observed when exciting with sufficient energy (>1900 cm^{-1}) for conformer A or B to potentially overcome the torsional barrier for interconversion from conformer A or B into C. Our calculations have indeed shown that the torsional barrier in switching between various conformers in the $1^1\pi\pi^*$ state corresponds to ∼2100 cm^{-1}, in very good agreement with this experimental onset. Once in conformer C, relaxation involving a barriered pathway may explain how deuteration effectively 'switches off' conformer C-driven dynamics resulting in τ_2, as evidenced by our results presented in Figure 3.3.

We end this section by considering the role of conformer specific dynamics further. As noted above, calculations for tunnelling probabilities were performed based on the PECs yielding tunnelling probabilities of 1.2×10^{-3}, 1.9×10^{-5} and 2.1×10^{-4} for H atom tunnelling along the O^1-H, O^2-H and O^3-H coordinates, respectively. Based on this simplified approach, one would anticipate that τ_H is attributed pri-

marily to H atom tunnelling in conformer A along the O^1-H coordinate. This presents us with the tantalising prospect of demonstrating conformer specific tunnelling dynamics. To validate this conundrum, high resolution H(Rydberg) atom photofragment translational spectroscopy measurements (such as those described in detail in Reference 33) could potentially enable one to glean information on whether tunnelling mediated dynamics in resorcinol are indeed conformer specific. Similarly, a more expansive theoretical approach would be required to assess the potential role of conformer specific tunnelling. In the first instance, PECs wherein the geometry is relaxed at each point along O–H would certainly be advantageous, although fully multi-dimensional potential energy surfaces would invariably enable us to learn more information regarding this and the tunneling arguments, involving interconversion between conformers, put forth in the preceding paragraphs.

3.5   Conclusions

The excited state dynamics of resorcinol following UV excitation at a range of pump wavelengths, 278 - 255 nm, have been investigated using a combination of ultrafast time-resolved ion yield measurements and time-resolved velocity map ion imaging coupled with complementary *ab initio* calculations.

Following excitation to the $1^1\pi\pi^*$ state below the $1^1\pi\pi^*/^1\pi\sigma^*$ CI, we extract a timescale for excited state relaxation, τ_1, that decreases as a function of excitation energy from 2.70 ns to $\sim$120 ps. This is ascribed to a competition between two relaxation mechanisms; H atom tunnelling beneath the CI, followed by coupling onto a dissociative $^1\pi\sigma^*$ state, yielding H atoms with high KE ($\sim$5000 cm^{-1}); and an IVR driven IC process that is able to transfer population from the photoexcited $1^1\pi\pi^*$ state back to a vibrationally excited ground state, S_0^*. We assign the increase in the rate of decay of the $1^1\pi\pi^*$ state to an enhancement in the density of vibrational states with increasing pump energy. This leads to a more efficient IVR process in out-of-plane modes which can promote IC onto S_0^*, eventually resulting in IC becoming the kinetically dominant decay pathway. Complete depopulation of the $1^1\pi\pi^*$ state occurs in $\sim$120 ps following excitation at 255 nm.

When exciting between 264 – 260 nm a bi-exponential decay is observed in the TR-IY transients. This time constant, τ_2, is still somewhat difficult to interpret. At this time we put forth two possible explanations as to the origins of τ_2; keto-enol tautomerisation or conformer specific dynamics. The deuterated results (τ_D) show no evidence of τ_2, suggesting that this process is barriered in some way. To confirm the validity of these explanations, however, requires further experimental and theoretical work, which we suggest may be the focus of a follow-up study.

Excitation above the $1^1\pi\pi^*/^1\pi\sigma^*$ CI yields H atoms produced on an ultrafast timescale as observed in previous investigations.[4,29] Following UV excitation with 237 nm light, high KE H atoms ($\sim$11000 cm^{-1}) are produced in $\sim$260 fs in line with a mechanism involving direct dissociation from the $^1\pi\sigma^*$ state or ultrafast coupling between the $1^1\pi\pi^*$ (or $2^1\pi\pi^*$) and $^1\pi\sigma^*$ state followed by dissociation.

The results presented above provide insight into the deactivation processes that are prevalent in systems possessing dissociative state. When compared to previous experiments, these results highlight the profound effect the presence of additional functional groups, and more specifically the precise location of the functional groups, can have on the excited state dynamics of model heteroaromatic systems following UV excitation. This leads us nicely onto the next chapter, wherein we increase the molecular complexity of the heteroaromatic species' under investigation in order to explore the excited state dynamics of the related phenolic species, catechol. As was discussed briefly in Section 1.7, when the two hydroxy- groups are placed *ortho-* to each other we introduce an intramolecular H bond to the system. This H bond brings about drastic changes to the excited state geometry allowing for the elegant investigation of vibrational motions that take place at the early stages of excited state relaxation.

References

1. Livingstone, R. A., Thompson, J. O. F., Iljina, M., Donaldson, R. J., Sussman, B. J., Paterson, M. J., and Townsend, D. *J. Chem. Phys.* **137**(18), 184304 (2012).

2. Chatterley, A. S., Johns, A. S., Stavros, V. G., and Verlet, J. R. R. *J. Phys. Chem. A* **117**(25), 5299–5305 (2013).

3. King, G. A., Oliver, T. A. A., Dixon, R. N., and Ashfold, M. N. R. *Phys. Chem. Chem. Phys.* **14**(10), 3338–3345 (2012).

4. Roberts, G. M., Chatterley, A. S., Young, J. D., and Stavros, V. G. *J. Chem. Phys. Lett* **3**(3), 348–352 (2012).

5. Myszkiewicz, G., Meerts, W. L., Ratzer, C., and Schmitt, M. *ChemPhysChem* **6**(10), 2129–2136 (2005).

6. Gerhards, M., Unterberg, C., and Schumm, S. *J. Chem. Phys.* **111**(17), 7966–7975 (1999).

7. Gerhards, M., Perl, W., and Kleinermanns, K. *Chem. Phys. Lett.* **240**(5-6), 506–512 (1995).

8. Even, U., Jortner, J., Noy, D., Lavie, N., and Cossart-Magos, C. *J. Chem. Phys.* **112**(18), 8068–8071 (2000).

9. Frisch, M. J., Trucks, G. W., Schlegel, H. B., Scuseria, G. E., Robb, M. A., Cheeseman, J. R., Montgomery, Jr., J. A., Vreven, T., Kudin, K. N., Burant, J. C., Millam, J. M., Iyengar, S. S., Tomasi, J., Barone, V., Mennucci, B., Cossi, M., Scalmani, G., Rega, N., Petersson, G. A., Nakatsuji, H., Hada, M., Ehara, M., Toyota, K., Fukuda, R., Hasegawa, J., Ishida, M., Nakajima, T., Honda,

Y., Kitao, O., Nakai, H., Klene, M., Li, X., Knox, J. E., Hratchian, H. P., Cross, J. B., Bakken, V., Adamo, C., Jaramillo, J., Gomperts, R., Stratmann, R. E., Yazyev, O., Austin, A. J., Cammi, R., Pomelli, C., Ochterski, J. W., Ayala, P. Y., Morokuma, K., Voth, G. A., Salvador, P., Dannenberg, J. J., Zakrzewski, V. G., Dapprich, S., Daniels, A. D., Strain, M. C., Farkas, O., Malick, D. K., Rabuck, A. D., Raghavachari, K., Foresman, J. B., Ortiz, J. V., Cui, Q., Baboul, A. G., Clifford, S., Cioslowski, J., Stefanov, B. B., Liu, G., Liashenko, A., Piskorz, P., Komaromi, I., Martin, R. L., Fox, D. J., Keith, T., Al-Laham, M. A., Peng, C. Y., Nanayakkara, A., Challacombe, M., Gill, P. M. W., Johnson, B., Chen, W., Wong, M. W., Gonzalez, C., and Pople, J. A. *Gaussian 03, Revision D.01*. Gaussian, Inc., Wallingford, CT, (2004).

10. Frisch, M. J., Trucks, G. W., Schlegel, H. B., Scuseria, G. E., Robb, M. A., Cheeseman, J. R., Scalmani, G., Barone, V., Mennucci, B., Petersson, G. A., Nakatsuji, H., Caricato, M., Li, X., Hratchian, H. P., Izmaylov, A. F., Bloino, J., Zheng, G., Sonnenberg, J. L., Hada, M., Ehara, M., Toyota, K., Fukuda, R., Hasegawa, J., Ishida, M., Nakajima, T., Honda, Y., Kitao, O., Nakai, H., Vreven, T., Montgomery, Jr., J. A., Peralta, J. E., Ogliaro, F., Bearpark, M., Heyd, J. J., Brothers, E., Kudin, K. N., Staroverov, V. N., Kobayashi, R., Normand, J., Raghavachari, K., Rendell, A., Burant, J. C., Iyengar, S. S., Tomasi, J., Cossi, M., Rega, N., Millam, J. M., Klene, M., Knox, J. E., Cross, J. B., Bakken, V., Adamo, C., Jaramillo, J., Gomperts, R., Stratmann, R. E., Yazyev, O., Austin, A. J., Cammi, R., Pomelli, C., Ochterski, J. W., Martin, R. L., Morokuma, K., Zakrzewski, V. G., Voth, G. A., Salvador, P., Dannenberg, J. J., Dapprich, S., Daniels, A. D., Farkas, ., Foresman, J. B., Ortiz, J. V., Cioslowski, J., and Fox, D. J. *Gaussian 09 Revision D.01*. Gaussian Inc Wallingford CT, (2009).

11. Werner, H. J., Knowles, P. J., Knizia, G., Manby, F. R., Schutz, M., Celani, P., Korona, T., Lindh, R., Mitrushenkov, A., Rauhut, G., Shamasundar, K. R., Adler, T. B., Amos, R. D., Bernhardsson, A., Berning, A., Cooper, D. L., Deegan, M. J. O., Dobbyn, A. J., Eckert, F., Goll, E., Hampel, C., Hesselmann, A., Hetzer, G., Hrenar, T., Jansen, G., Koppl, C., Liu, Y., Lloyd, A. W., Mata, R. A., May, A. J., McNicholas, S. J., Meyer, W., Mura, M. E., Nicklass, A., ONeill, D. P., Palmieri, P., Peng, D., Pfluger, K., Pitzer, R., Reiher, M., Shiozaki, T., Stoll, H., Stone, A. J., Tarroni, R., Thorsteinsson, T., and Wang, M. *MOLPRO, version 2012.1, a package of ab initio programs.* see http://www.molpro.net.

12. Adamo, C. and Barone, V. *J. Chem. Phys.* **110**(13), 6158–6170 (1999).

13. Stanton, J. F. and Bartlett, R. J. *J. Chem. Phys.* **98**(9), 7029–7039 (1993).

14. Leang, S. S., Zahariev, F., and Gordon, M. S. *J. Chem. Phys.* **136**(10), 104101 (2012).

15. Bearpark, M. J., Robb, M. A., and Schlegel, H. B. *Chem. Phys. Lett.* **223**(3), 269–274 (1994).

16. Celani, P. and Werner, H. J. *J. Chem. Phys.* **112**(13), 5546–5557 (2000).

17. Werner, H. J. *Mol. Phys.* **89**(2), 645–661 (1996).

18. Siegbahn, P. E. M. *Chem. Phys. Lett.* **109**(5), 417–423 (1984).

19. Klene, M., Robb, M. A., Frisch, M. J., and Celani, P. *J. Chem. Phys.* **113**(14) (2000).

20. Dixon, R. N., Oliver, T. A. A., and Ashfold, M. N. R. *J. Chem. Phys.* **134**(19), 194303 (2011).

21. Huang, Z. H., Feuchtwang, T. E., Cutler, P. H., and Kazes, E. *Phys. Rev. A* **41**(1), 32–41 (1990).

22. Roberts, G. M., Williams, C. A., Yu, H., Chatterley, A. S., Young, J. D., Ullrich, S., and Stavros, V. G. *Faraday Discuss.* **163**, 95–116 (2013).

23. Bist, H., Brand, J., and Williams, D. *J. Mol. Spectrosc.* **24**(1-4), 413 – 467 (1967).

24. Berden, G., Meerts, W. L., Schmitt, M., and Kleinermanns, K. *J. Chem. Phys.* **104**(3), 972–982 (1996).

25. Karsili, T. N. V., Wenge, A. M., Harris, S. J., Murdock, D., Harvey, J. N., Dixon, R. N., and Ashfold, M. N. R. *Chem. Sci.* **4**(6), 2434–2446 (2013).

26. Palmer, I. J., Ragazos, I. N., Bernardi, F., Olivucci, M., and Robb, M. A. *J. Am. Chem. Soc.* **115**(2), 673–682 (1993).

27. Vieuxmaire, O. P. J., Lan, Z., Sobolewski, A. L., and Domcke, W. *J. Chem. Phys.* **129**(22), 224307 (2008).

28. Roberts, G. M., Williams, C. A., Young, J. D., Ullrich, S., Paterson, M. J., and Stavros, V. G. *J. Am. Chem. Soc.* **134**(30), 12578–12589 (2012).

29. Chatterley, A. S., Young, J. D., Townsend, D., Zurek, J. M., Paterson, M. J., Roberts, G. M., and Stavros, V. G. *Phys. Chem. Chem. Phys.* **15**(18), 6879–6892 (2013).

30. Pino, G. A., Oldani, A. N., Marceca, E., Fujii, M., Ishiuchi, S. . I., Miyazaki, M., Broquier, M., Dedonder, C., and Jouvet, C. *J. Chem. Phys.* **133**(12), 124313 (2010).

31. Fermi, E. *Nuclear Physics.* University of Chicago Press, (1950).

32. Hadden, D. J., Roberts, G. M., Karsili, T. N. V., Ashfold, M. N. R., and Stavros, V. G. *Phys. Chem. Chem. Phys.* **14**(38), 13415–13428 (2012).

33. Ashfold, M. N. R., King, G. A., Murdock, D., Nix, M. G. D., Oliver, T. A. A., and Sage, A. G. *Phys. Chem. Chem. Phys.* **12**(6), 1218–1238 (2010).

34. Roberts, G. M., Hadden, D. J., Bergendahl, L. T., Wenge, A. M., Harris, S. J., Karsili, T. N. V., Ashfold, M. N. R., Paterson, M. J., and Stavros, V. G. *Chem. Sci.* **4**(3), 993–1001 (2013).

35. Ashfold, M. N. R., Cronin, B., Devine, A. L., Dixon, R. N., and Nix, M. G. D. *Science* **312**(5780), 1637–1640 (2006).

36. Wang, X.-B., Fu, Q., and Yang, J. *J. Phys. Chem. A* **114**(34), 9083–9089 (2010).

37. Helman, A. and Marcus, R. A. *J. Chem. Phys.* **99**(7), 5011–5029 (1993).

38. Schubert, U., Riedle, E., and Neusser, H. J. *J. Chem. Phys.* **90**(11), 5994–6007 (1989).

39. Suzuki, T. and Ito, M. *J. Chem. Phys.* **91**(8), 4564–4570 (1989).

40. Callomon, J. H., Parkin, J. E., and Lopezdel.r. *Chem. Phys. Lett.* **13**(2), 125–& (1972).

41. Minns, R. S., Parker, D. S. N., Penfold, T. J., Worth, G. A., and Fielding, H. H. *Phys. Chem. Chem. Phys.* **12**(48), 15607–15615 (2010).

42. Parker, D. S. N., Minns, R. S., Penfold, T. J., Worth, G. A., and Fielding, H. H. *Chem. Phys. Lett.* **469**(1-3), 43–47 (2009).

43. Worth, G. A., Carley, R. E., and Fielding, H. H. *Chem. Phys.* **338**(2-3), 220–227 (2007).

44. Clara, M., Hellerer, T., and Neusser, H. J. *Appl. Phys. B - Lasers O.* **71**(3), 431–437 (2000).

45. Stein, S. E. and Rabinovi, B. *J. Chem. Phys.* **58**(6), 2438–2445 (1973).

46. Reid, K. L. *Int. Rev. Phys. Chem.* **27**(4), 607–628 (2008).

47. von Benten, R. S., Liu, Y., and Abel, B. *J. Chem. Phys.* **133**(13), 134306 (2010).

48. D'Cunha, C., Morozov, A. N., and Chatfield, D. C. *J. Phys. Chem. A* **117**(35), 8437–8448 (2013).

49. Alsoufi, W., Grellmann, K. H., and Nickel, B. *J. Phys. Chem.* **95**(25), 10503–10509 (1991).

Chapter 4

Real-time Observation of Vibrational Motion in Catechol

Tracking torsional motion following UV absorption
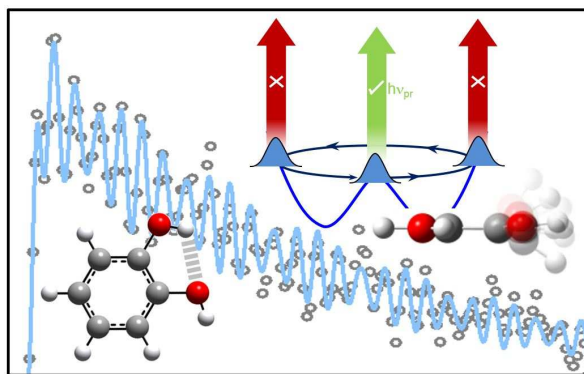
This chapter is based on the following publication:

4.1 Introduction

As an extension to the work performed in Chapter 3, we now extend our "bottom-up" approach to the study of the excited state dynamics of catechol (1,2-dihydroxy-benzene), the structure of which is shown in Figure 4.1. The catechol subunit is incorporated in a number of biologically relevant species such as eumelanin,[1–3] the brown pigment co-polymer found in human skin, which serves as a front line defence to UV radiation exposure. It was revealed in previous investigations,[4–6] and discussed in Chapter 3, that following photoexcitation from the electronic ground state (S_0) to the origin of the first excited state (S_1, $\nu' = 0$; $^1\pi\pi^* \leftarrow S_0$ transition), catechol undergoes O–H bond fission mediated *via* a tunnelling mechanism. This occurs beneath an S_1/S_2 conical intersection (CI), where the S_2 state is a $^1\pi\sigma^*$ state that is dissociative along the O–H coordinate. Importantly, with respect to this present study, our group showed that O–H fission occurred on a ps timescale,[4] orders of magnitude faster than that seen for other dihydroxybenzenes, despite a similar barrier to tunnelling.[6–8] Figure 4.2 shows a transient collected from time-resolved ion yield (TR-IY) measurements on catechol, following excitation around the S_1 origin. This serves to highlight the stark difference between phenol and resorcinol's excited state dynamics, whose excited state lifetimes around the S_1 origin are of the order of ns, compared to catechol which has a lifetime less than 10 ps.

As was mentioned at the outset of Chapter 3, the faster rate of H atom tunnelling (and hence S_1 lifetime) in catechol was rationalised by the presence of the non-planar minimum geometry in the excited electronic state. Unlike phenol, and the previously studied resorcinol, the presence of the second hydroxy-group *ortho-* to the first, leads to the formation of an intramolecular H bond between these two functional moieties. This distorts the geometry from planarity in S_1, relative to the planar ground state structure (Figure 4.3(a)).

The object of the work presented in this chapter is to study, in detail, the vi-
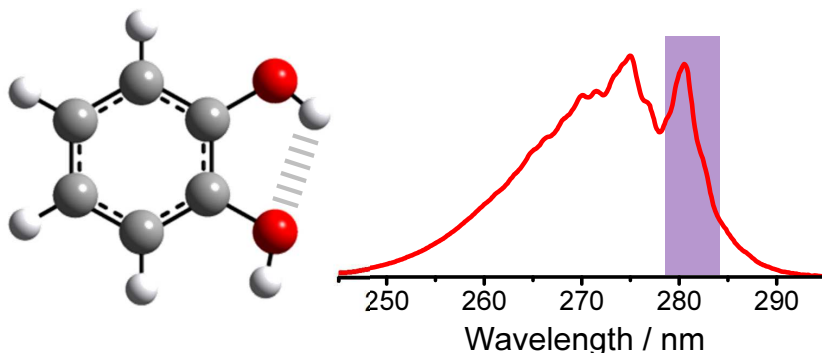
Figure 4.1: Calculated structure of catechol in the S_0 state accompanied by the vapor phase UV-Vis absorption spectrum for catechol (red line). The highlighted region indicates the excitation region for the current study.
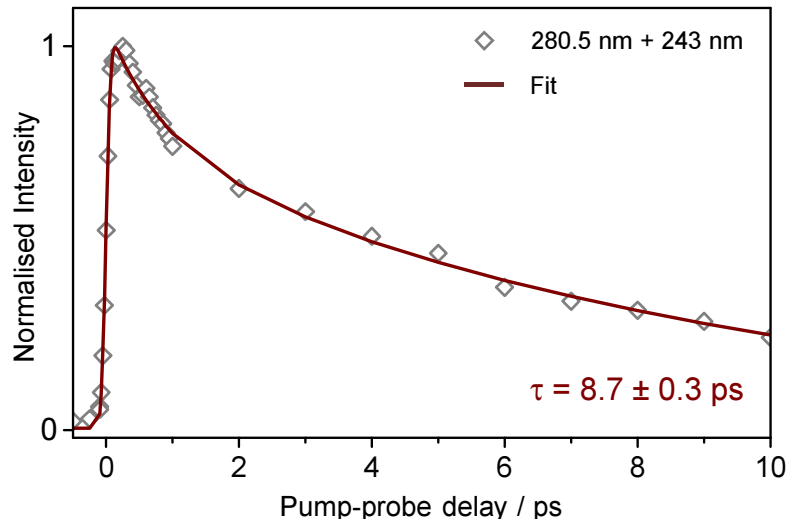
Figure 4.2: Normalised catechol$^+$ parent ion signal (grey diamonds) acquired after excitation to S_1 ($\nu' = 0$) at 280.5 nm. The kinetic fit to this transient is indicated by the solid brown line (see ESI of Reference 9 and appendix). Reproduced from Reference 9.

brational motions that occur prior to, and even during, the tunnelling process. In order to probe these atomic motions in real time, we utilise the difference in geometry between S_1 and the ground cationic state (D_0) as an effective Franck-Condon (FC) detection window. Following UV irradiation, a coherent superposition of low-lying FC-active vibrational motions is created in S_1, resulting in the formation of a localised vibrational wavepacket (see Section 1.4). The temporal evolution of the prepared superposition can then be probed by virtue of the non-planar $\rightarrow$ planar ($S_{1min} \rightarrow$ catechol$^+$) geometry change upon photoionisation (Figure 4.3(a)). The evolution of the prepared wavepacket allows us to gain important insight into the nuclear motions responsible for energy flow on S_1 at the very early stages of photodissociation in catechol. We utilise a combination of TR-IY and time-resolved velocity map imaging (TR-VMI) to directly probe these nuclear motions, with complementary theoretical calculations to illuminate the observed dynamics.

4.2   Methods

4.2.1   Experimental

Catechol is first seeded into helium ($\sim$2 bar) and expanded into vacuum ($\sim$10^{-7} mbar) using the Even-Lavie pulsed valve.[10] Following excitation of catechol using $h\nu_{pu}$, a coherent superposition of low frequency FC-active modes is prepared on the S_1 state, creating a vibrational wavepacket as described by Section 1.4. The excited wavepacket is allowed to evolve over time, and is then projected (photoionised) onto the D_0 state using the second, time-delayed (Δt) fs probe pulse ($h\nu_{pr}$). The resulting catechol$^+$ ion signal is recorded as a function of pump-probe delay using
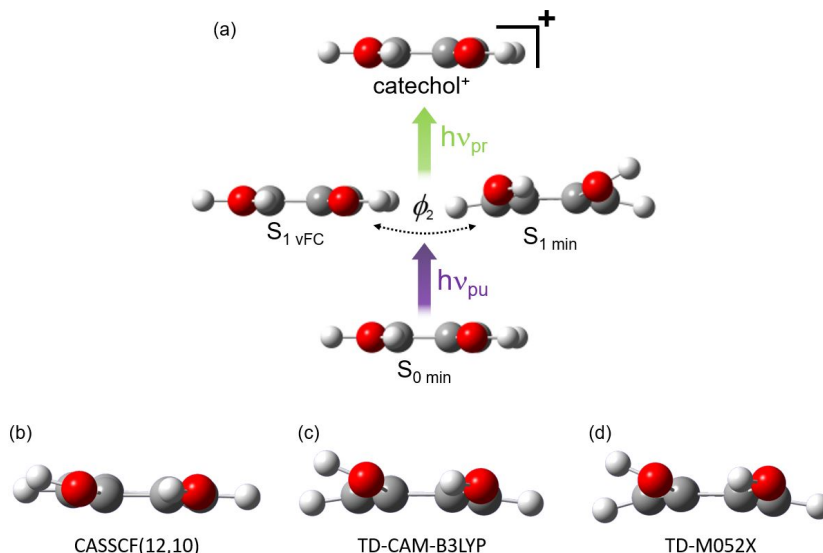
Figure 4.3: (a) Schematic representation of the pump-probe process showing the associated nuclear geometries calculated by using the CAM-B3LYP functional. Also shown are the minimum energy geometries of catechol's S_1 state (S_{1min}) at the (b) CASSCF(12,10) (c) TD-CAM-B3LYP and (d) TD-M052X levels of theory. All calculations utilised an aug-cc-pVDZ basis set.

the MCP detector coupled to the oscilloscope. The pump pulse is centred around the strongly absorbing S_1 origin band (Figure 4.1) whilst the probe pulse is selected such that the total energy, E_{tot}, is sufficient to photoionise just above the adiabatic ionisation potential (IP_{ad}), which in catechol lies at 8.17 eV.[11]

4.2.2 Theoretical Methods

To garner further insight into the excited state dynamics, we have also performed complementary calculations using the Gaussian 09[12] and Molpro 2012.1[13] computational packages in order to generate optimised ground, excited and ionic state geometries and also calculate potential energy cuts (PECs) along the O–H coordinate for both the ground and excited states.

All geometries for catechol were calculated using Gaussian 09 with the CAM-B3LYP[14] level of theory and an aug-cc-pVDZ basis set. The geometry in the S_1 state was also calculated with the M052X[15] functional, as well as multi-configurational complete active space self-consistent field (CASSCF).[16] These calculated structures are shown in Figure 4.3(b-d) and highlight the distorted structure of the first excited state.

The PECs of the ground and excited electronic states of catechol were calculated using CASPT2 with a (12,10) active space, performed with Molpro. The active space consisted of the three π bonding orbitals, the two $n\pi$ non-bonding orbitals associated with the O atoms, the three π^* anti-bonding orbitals and the corresponding σ bonding and σ^* anti-bonding orbitals associated with the 'free' O–H bond coordinate. In order to construct the cuts along $R_{O–H}$ (shown in Figure 4.7(c)), first a geometry optimisation was performed in S_0 using CAM-B3LYP and
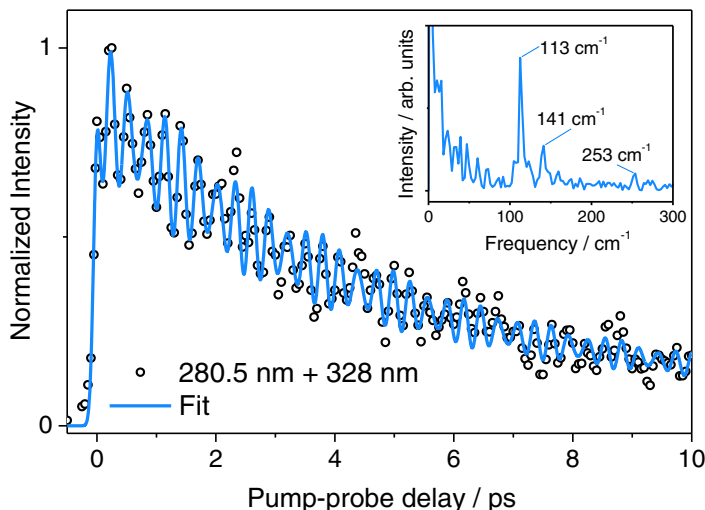
Figure 4.4: TR-IY transient collected from catechol following UV excitation at 280.5 nm and subsequent photoionisation (probing) using 328 nm. A 50 fs step size was used (as indeed elsewhere) to resolve the oscillations. The solid blue line indicates the fit as described in the main text. Inset: The FFT of the transient.

the aug-cc-pVDZ basis set. The O–H bond length was then increased from the ground state equilibrium position to a distance of 4 Å (where the surface becomes asymptotic) then stepped back to 0.6 Å at varying intervals of R_{O-H}. Energies for each of the levels, S_0 (black line), S_1 (red line) and S_2 (blue line) were then calculated for each value of R_{O-H}. For each cut, and at each O–H torsion angle (ϕ), only the O–H bond length was changed, all other geometric parameters being held constant, resulting in unrelaxed (rigid body) PECs.

In an effort to determine the effect of the torsional angle on the tunnelling rate, S_1 and S_2 PECs along R_{O-H} were also calculated at varying angles of ϕ ($\phi = 0° - 28°$). The cuts for $\phi \sim 0°$ (planar - solid lines) and $\phi \sim 14°$ (bent - dashed lines) are shown in Figure 4.7(c). As was seen in Chapter 3, and in Section 1.4.4, the tunnelling probability (T_R) can be calculated using the WKB approximation.[17] The values returned from this method across all the calculated values of ϕ are shown by the graph inset in Figure 4.7(c). We return to discuss this figure and T_R later in the chapter.

4.3 Results and Discussion

Figure 4.4 shows a typical TR-IY transient (open circles) recorded following excitation of catechol with 280.5 nm and probing with 328 nm, such that E_{tot} is only 0.03 eV above the IP_{ad}. The overall shape of the transient is as shown previously in Figure 4.2 when probing with 243 nm; a very fast rise around $\Delta t = 0$, the point of temporal overlap between pump and probe beams, which ultimately decays over a period of several ps.[4] However, unlike the previously recorded transient, in which E_{tot} far exceeded IP_{ad} (by 1.35 eV), immediately apparent now is a superimposed oscillation that appears in the transient.

By taking the fast Fourier transform (FFT) of the transient data, one can extract the frequencies of any oscillatory components in a given TR-IY transient. In all cases, zero padding of the TR-IY data was used to ensure an appropriate number of data points without artificially reducing the frequency resolution.[i] The FFT for the transient (Figure 4.4) is shown inset in the same figure, and yields two frequencies with associated energies centred at 113 cm^{-1} and 141 cm^{-1}, which correspond to wavenumber separations of vibrational eigenstates within the initially prepared wavepacket on S_1.[18] From these frequencies it is trivial to calculate the associated periods for the vibrations. Conversion of the wavenumber frequencies into Hz, then taking the inverse yields periods of 295 and 237 fs, for the 113 cm^{-1} and 141 cm^{-1} components, respectively. Comparison of these frequencies with frequency resolved spectra of the catechol S_1 state provides insight into which eigenstates are prepared within the superposition.[5] The observed frequencies are in excellent accord with the band separations in the vibrational progression of the low-lying O–H torsional mode (ϕ_2), primarily of the free (*i.e.* non-intramolecular hydrogen bonded, Figure 4.1) O–H moiety. Specifically, these frequencies correspond to wavenumber separations between (i) the S_1 origin and one quantum of excitation in ϕ_2 (S_1, $\nu' = 0$ and $\phi_2\,_0^{1+}$, respectively, $\Delta E = 115$ cm^{-1}) and (ii) one and two quanta of excitation in ϕ_2 ($\phi_2\,_0^{1+}$ and $\phi_2\,_0^{2+}$, respectively, $\Delta E = 141$ cm^{-1}).[5] Indeed, closer inspection of the FFT also reveals an additional feature, albeit much weaker, with an associated energy around 250 cm^{-1}. This frequency corresponds to the wavenumber separation between the S_1 origin and $\phi_2\,_0^{2+}$ ($\Delta E = 256$ cm^{-1}). The broadness of this peak, and to a lesser extent the peaks at 113 cm^{-1} and 141 cm^{-1}, reflects the limited time window over which these beats can be observed, due to the fast overall decay of the S_1 state.

We are able to model the TR-IY transient, using a decay function convoluted with our IRF, which serves to model the overall rise (following the excitation pulse) and decay in the transient, in combination with two cosine functions to model the quantum beats. The cosine functions are themselves superimposed with an exponential decay which serves to dampen the quantum beats (*vide infra* and appendix). The blue line in Figure 4.4 gives the resultant overall fit to the measured transient. The frequencies obtained from the fit align extremely well with those extracted *via* the FFT, giving values of 113 cm^{-1} and 140 cm^{-1} (periods of 295 fs and 239 fs, respectively), adding weight to our assignment of these beats to the progression in the free O–H torsional motion.

We now consider the origins of these quantum beats, assisted by the schematic shown in Figure 4.5(a), which is adapted from Reference 19, and the knowledge discussed in Section 1.4. After excitation from the planar S_0 ground state, a coherent

---

[i]Zero-padding is a simple concept that involves adding zeros to the end of a time-domain signal in order to increase it's length and ensure the waveforms have a power-of-two number of data points. When the time-domain length of a waveform is a power of two, the FFT algorithm, which is extremely efficient, can be used to speed up processing time.

superposition of one and two quanta in ϕ_2 creates a vibrational wavepacket along this normal mode coordinate on S_1 as the geometry relaxes towards its non-planar minimum, as shown in Figure 4.3(a), represented by $S_{1,vFC} \rightarrow S_{1,min}$ (where vFC denotes vertical Franck-Condon region). However, the final D_0 state of catechol$^+$ is planar, and the nuclear configuration is once again different, now between S_1 (non-planar) and D_0 (planar), resulting in a variable ionisation cross-section to D_0 along ϕ as the wavepacket oscillates on S_1 (Figure 4.5, red and green arrows). Provided the vibrational wavepacket is localised (*i.e.* not dephased), this results in the characteristic beat seen in Figure 4.4. The wavepacket oscillates along ϕ and can only be probed at or around $\phi = 0$, as the probe photon energy is greater than IP$_{ad}$ (green arrows); at non-planar geometries, the probe photon energy is insufficient to overcome IP$_{ad}$ (red arrows).

At this juncture, it is important to emphasise that a coherent superposition of vibrational levels can be generated irrespective of structural distortion in S_1 relative to S_0 (*cf.* phenol and resorcinol). However, to probe the temporal evolution of this prepared wavepacket and observe a quantum beat using TR-IY, one requires an adequate FC detection window which is afforded here by the structural distortion between the S_1 (non-planar) and D_0 (planar) geometries in catechol and catechol$^+$, respectively. This is absent in phenol given that S_1 and D_0 are both planar and possess similar geometries.[20,21] The situation described here can be directly likened to the classic study of vibrational wavepacket dynamics in the Cs$_2$ alkali metal dimer using energy-integrated photoelectron spectroscopy (analogous to TR-IY of the parent$^+$ cation here), where detection of the quantum beating is a sole consequence of different equilibrium nuclear separations for the excited C-state of neutral Cs$_2$ and the ground state of the Cs$_2^+$ cation.[22,23] We also stress that the FC window for quantum beat detection using TR-IY methods is very sensitive to the probe wavelength; when the combined pump and probe pulse energy far exceeds the IP$_{ad}$, the beats disappear as seen in Figure 4.2.[24] Once again, this is directly in-line with what we observe here and with previous vibrational wavepacket studies.[23]

It is possible to attribute the apparent damping in the quantum beats in Figure 4.4 to the S_1 decay or, as we shall see in Chapter 5 for guaiacol and syringol, to IVR, or both. With reference to the frequency resolved measurements,[5,26] within our excitation pulse, the only FC active vibrational modes present are from the short progression in ϕ_2, with only a limited set of these modes within the spectral bandwidth of our excitation pulse (~ 500 cm^{-1}). This means that any IVR, at first sight, is not possible around the S_1 origin. Calculations however suggest a small number of heavily mixed vibrational modes (reminiscent of those seen in guaiacol, which also has a non-planar S_1 state minimum, and undergoes Duschinsky mixing[27]), including ϕ_2, that may fall within our excitation window.[4,26] This implies that IVR, whilst highly restricted, cannot be entirely ruled out.

To explore this further, Figure 4.5(b) (blue trace) shows the fit to the transient shown in Figure 4.4. If we now scale the overall fit function with respect to the S_1
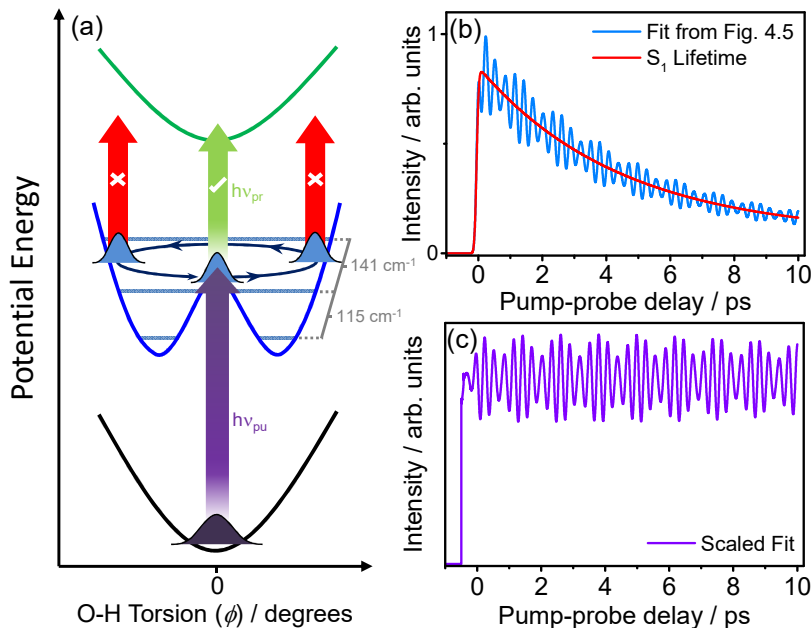
Figure 4.5: (a) Schematic depiction of the excitation mechanism adapted from References 25 and 19. (b) The fit function from Figure 4.4 (blue line) and the same fit but with the oscillatory components removed from the fit (i.e. the S_1 lifetime; red line). (c) The resulting trace following scaling of the fit from (b); further details in the main text.

decay (Figure 4.5(b), red line), this yields the trace shown in Figure 4.5(c), comprised solely of the sinusoidal quantum beats, clearly emphasising the persistence of the oscillations for the duration of the excited state lifetime. We can therefore attribute the apparent damping of the quantum beats simply through the fact that the overall S_1 population decays almost completely within our 10 ps window. The amplitude of the quantum beat oscillations therefore decreases proportionally to the population of S_1. Predictably, this suggests that there is no IVR taking place, from our excited state population, following photoexcitation to the S_1 state. We note that the S_1 decay in these measurements actually appears somewhat shorter than previous experiments around the S_1 origin ($\sim$6.6 ps *cf.* $\sim$8.7 ps from Figure 4.2).[4] This disparity is likely a result of an evident decrease in the *total* ion signal over the course of the data acquisition (many transients with very small step-sizes were accumulated to extract reliable beat frequencies) in addition to the different probe wavelength (328 nm *vs.* 243 nm). Such drifts in the ion signal are inevitable and unfortunately unavoidable given the long data acquisition time and result in an artificial shortening of the extracted lifetime.

Interestingly, the decay times we obtain here ($\sim$6.6 ps), and indeed the previously recorded values,[4] accord well with the excited state lifetimes measured by Weiler *et al.*[26] following photoexcitation at the S_1 origin (7 ps). This value is notably shorter than when exciting higher quanta of ϕ_2; $\phi_2{}_0^{1+}$ (11 ps) and $\phi_2{}_0^{2+}$ (10 ps). Figure 4.6 shows schematic vibrational wavefunctions for the torsional coordinate. The authors state that the timescale for tunnelling beneath the S_1/S_2 CI
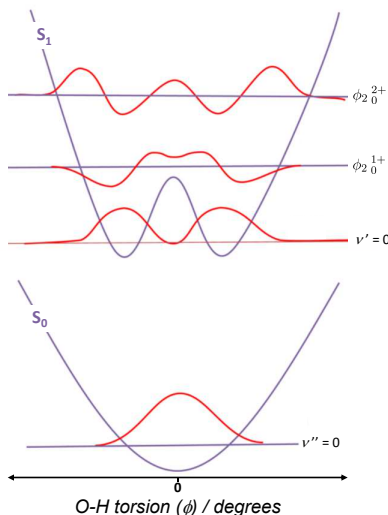
Figure 4.6: A schematic representation of the wavefunctions along the out-of-plane torsional coordinate (ϕ), adapted from Reference 26. It is clear that at $\nu' = 0$, the probability density is only non-zero at bent geometries ($\phi > 0$).

is strongly coupled to the degree of planarity of the catechol molecule; the more distorted the geometry, the stronger the coupling between S_1 and S_2 and hence a faster tunnelling time. This, once again, highlights the importance of investigating these early time vibrational motions.

Tuning the excitation pulse wavelength, allows manipulation of the contribution of one component beat over the other in our coherent superposition. By increasing the excitation wavelength to 281.5 nm and probing with 326.6 nm (total photon energy is once again 8.2 eV, 0.03 eV above IP$_{ad}$), the spectral bandwidth of our excitation pulse no longer encompasses $\phi_2{}_0^{2+}$ but only $\phi_2{}_0^{1+}$ and the S_1 origin. This is manifested as a single quantum beat in the measured transient and is shown in Figure 4.7(a) with the inset showing the FFT, which almost exclusively yields a single frequency with an associated energy of 116 cm^{-1} (*i.e.* the energy difference between S_1, $\nu' = 0$ and $\phi_2{}_0^{1+}$). The solid line is once again a fit to the measured transient although in this case only a single cosine function was required to model the single quantum beat, damped, once again, by the overall decay in S_1.

Previous work by King *et al.*[5] on the photodissociation dynamics of catechol has suggested that the initial torsional excitation can be efficiently redistributed into ring puckering and likely in-plane ring stretching vibrations as the H atom of the free O–H tunnels beneath the S_1/S_2 CI, *en route* to O–H dissociation. This is evidenced through population of these modes in the catechoxyl radical cofragment. The quantum beats observed here allow us to directly infer the extent of population transfer from the O–H torsional motion into any additional modes prior to tunnelling. The lack of IVR evidenced in these quantum beats leads us to conclude that the considerable degree of mode mixing already present within the S_1 manifold,[4,25,26] likely translates into vibrational motion in the catechoxyl radical.

We might anticipate, given the remarkably strong coherence of the initially
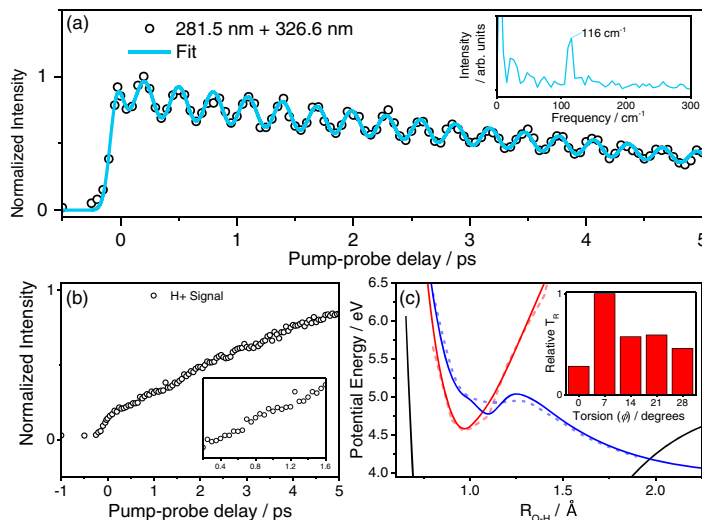
Figure 4.7: (a) The TR-IY transient collected from catechol following excitation and probing with 281.5 and 326.6 nm, respectively. The solid blue line indicates the fit as described in the main text. Inset: The FFT of the transient. (b) Representative H^+ transient recorded at the same pump wavelength as the TR-IY transient and probing with 243 nm (to resonantly ionise H atoms). Inset: Enlarged section of the transient to highlight the lack of stepwise increase in signal. (c) S_0 (black), S_1 (red), and S_2 (blue) PECs along R_{O-H} when the molecular geometry is both planar (solid lines) and bent (dashed lines). Inset: Graph showing the effect ϕ has on the tunneling probability T_R.

prepared superposition in catechol, to observe a reflection of this periodicity in any dissociated H atoms. A representative H^+ transient obtained using TR-VMI is shown in Figure 4.7(b). It is clear that within the signal to noise, we are unable to resolve any prevalent stepwise increase in the H^+ signal. In an attempt to explore this further, we undertook calculations to investigate how the S_1 state energy landscape changes as a function of the torsional coordinate of the free O–H. Figure 4.7(c) highlights the S_1 and S_2 PECs along R_{O-H} when the molecular geometry is both planar ($S_{1vFC}, \phi \sim 0°$ - solid lines) and where the free O–H lies out of the molecular plane ($S_{1min}, \phi \sim 14°$ - dashed lines).

Cursory inspection reveals that, while there is some change to the overall area of the barrier to tunnelling, the absolute effect of this change is likely too small for the present measurements to detect. This is highlighted by the graph inset which shows the relative tunnelling probability (T_R), calculated using the 1D WKB approximation explained in Section 1.4.4 as a function of ϕ.[17] Whilst T_R is lowest at planar geometry, the overall variation in T_R is insufficient (certainly within our signal-to-noise) to be mapped through onto the H^+ transient. Interestingly, the finding that T_R is lowest at planar geometry accords with the measurements of Weiler *et al.* mentioned above;[26] the more planar (*i.e.* ϕ approaches zero), the longer the lifetime measured. We must acknowledge however the over-simplicity of these calculations, given that we are effectively freezing all other nuclear coordinates and varying only ϕ and R_{O-H} of the free O–H. That being said, the results provide impetus for future calculations incorporating geometry relaxation along all

coordinates.

4.4   Conclusions

In conclusion, vibrational wavepackets were prepared in the S_1 state of the catechol chromophore. The subsequent temporal evolution of the superposition shows a strong quantum beat pattern in the parent transient, possessing frequencies in line with the progression in the heavily mixed ϕ_2 mode. The apparent dampening in the quantum beat is attributed to the S_1 decay, with no evidence of any measurable IVR taking place from the excited state population localised in this mode. Calculations were performed in an effort to characterise the excited state landscape as a function of the torsional angle. We find that, while the tunnelling probability, T_R, varies with changing ϕ, this variance is insufficient to produce resolvable evidence for a stepwise increase in the H (and thus H$^+$) photofragment.

The results presented in this chapter, serve to highlight key nuclear motions that are responsible for energy flow in this important biological chromophore. They also demonstrate the sensitivity of TR-IY spectroscopy; showing that, given careful choice of experimental parameters, in this case careful selection of probe wavelengths combined with the intrinsic molecular properties, *i.e.*, a change in nuclear geometry between electronic states, it is possible to gain exquisite insight into the concerted atomic motions of a molecule as the wavepacket evolves on the excited state surface, whilst undergoing photodissociation. We have also observed a case wherein IVR appears to be inoperative within the temporal window of the present measurements. This is in stark contrast to what we will see in the following chapter for guaiacol and syringol, where the increased density of states, brought about by the enhanced molecular complexity, promotes efficient IVR and thus irreversible dephasing of the photoprepared wavepacket.

References

1. Meredith, P., Powell, B. J., Riesz, J., Nighswander-Rempel, S. P., Pederson, M. R., and Moore, E. G. *Soft Matter* **2**(1), 37–44 (2006).

2. Sobolewski, A. L. and Domcke, W. *ChemPhysChem* **8**(5), 756–762 (2007).

3. Huijser, A., Pezzella, A., and Sundstrom, V. *Phys. Chem. Chem. Phys.* **13**(20), 9119–9127 (2011).

4. Chatterley, A. S., Johns, A. S., Stavros, V. G., and Verlet, J. R. R. *J. Phys. Chem. A* **117**(25), 5299–5305 (2013).

5. King, G. A., Oliver, T. A. A., Dixon, R. N., and Ashfold, M. N. R. *Phys. Chem. Chem. Phys.* **14**(10), 3338–3345 (2012).

6. Livingstone, R. A., Thompson, J. O. F., Iljina, M., Donaldson, R. J., Sussman, B. J., Paterson, M. J., and Townsend, D. *J. Chem. Phys.* **137**(18), 184304 (2012).

7. Staniforth, M., Chatterley, A. S., Young, J. D., Roberts, G. M., and Stavros, V. G. *Biomedical Spectroscopy and Imaging* **3**(3) (2014).

8. Young, J. D., Staniforth, M., Chatterley, A. S., Paterson, M. J., Roberts, G. M., and Stavros, V. G. *Phys. Chem. Chem. Phys.* **16**(2), 550–562 (2014).

9. Chatterley, A. S., Young, J. D., Townsend, D., Zurek, J. M., Paterson, M. J., Roberts, G. M., and Stavros, V. G. *Phys. Chem. Chem. Phys.* **15**(18), 6879–6892 (2013).

10. Even, U., Jortner, J., Noy, D., Lavie, N., and Cossart-Magos, C. *J. Chem. Phys.* **112**(18), 8068–8071 (2000).

11. Gerhards, M., Schumm, S., Unterberg, C., and Kleinermanns, K. *Chem. Phys. Lett.* **294**(1-3), 65–70 (1998).

12. Frisch, M. J., Trucks, G. W., Schlegel, H. B., Scuseria, G. E., Robb, M. A., Cheeseman, J. R., Scalmani, G., Barone, V., Mennucci, B., Petersson, G. A., Nakatsuji, H., Caricato, M., Li, X., Hratchian, H. P., Izmaylov, A. F., Bloino, J., Zheng, G., Sonnenberg, J. L., Hada, M., Ehara, M., Toyota, K., Fukuda, R., Hasegawa, J., Ishida, M., Nakajima, T., Honda, Y., Kitao, O., Nakai, H., Vreven, T., Montgomery, Jr., J. A., Peralta, J. E., Ogliaro, F., Bearpark, M., Heyd, J. J., Brothers, E., Kudin, K. N., Staroverov, V. N., Kobayashi, R., Normand, J., Raghavachari, K., Rendell, A., Burant, J. C., Iyengar, S. S., Tomasi, J., Cossi, M., Rega, N., Millam, J. M., Klene, M., Knox, J. E., Cross, J. B., Bakken, V., Adamo, C., Jaramillo, J., Gomperts, R., Stratmann, R. E., Yazyev, O., Austin, A. J., Cammi, R., Pomelli, C., Ochterski, J. W., Martin, R. L., Morokuma, K., Zakrzewski, V. G., Voth, G. A., Salvador, P., Dannenberg, J. J., Dapprich, S., Daniels, A. D., Farkas, ., Foresman, J. B., Ortiz, J. V., Cioslowski, J., and Fox, D. J. *Gaussian 09 Revision D.01.* Gaussian Inc Wallingford CT, (2009).

13. Werner, H. J., Knowles, P. J., Knizia, G., Manby, F. R., Schutz, M., Celani, P., Korona, T., Lindh, R., Mitrushenkov, A., Rauhut, G., Shamasundar, K. R., Adler, T. B., Amos, R. D., Bernhardsson, A., Berning, A., Cooper, D. L., Deegan, M. J. O., Dobbyn, A. J., Eckert, F., Goll, E., Hampel, C., Hesselmann, A., Hetzer, G., Hrenar, T., Jansen, G., Koppl, C., Liu, Y., Lloyd, A. W., Mata, R. A., May, A. J., McNicholas, S. J., Meyer, W., Mura, M. E., Nicklass, A., ONeill, D. P., Palmieri, P., Peng, D., Pfluger, K., Pitzer, R., Reiher, M., Shiozaki, T., Stoll, H., Stone, A. J., Tarroni, R., Thorsteinsson, T., and Wang, M. *MOLPRO, version 2012.1, a package of ab initio programs.* see http://www.molpro.net.

14. Yanai, T., Tew, D. P., and Handy, N. C. *Chem. Phys. Lett.* **393**(1-3), 51–57 (2004).

15. Zhao, Y., Schultz, N. E., and Truhlar, D. G. *J. Chem. Theory Comput.* **2**(2), 364–382 (2006).

16. Werner, H. J. and Knowles, P. J. *J. Chem. Phys.* **82**(11), 5053–5063 (1985).

17. LeRoy, R. J. and Liu, W. K. *J. Chem. Phys.* **69**(8), 3622–3631 (1978).

18. Zewail, A. H. *Angew. Chem., Int. Edit.* **39**(15), 2587–2631 (2000).

19. Gerhards, M., Perl, W., Schumm, S., Henrichs, U., Jacoby, C., and Kleinermanns, K. *J. Chem. Phys.* **104**(23), 9362–9375 (1996).

20. LeClaire, J. E., Anand, R., and Johnson, P. M. *J. Chem. Phys.* **106**(17), 6785–6794 (1997).

21. Schumm, S., Gerhards, M., and Kleinermanns, K. *J. Phys. Chem. A* **104**(46), 10648–10655 (2000).

22. Rodriguez, G. and Eden, J. G. *Chem. Phys. Lett.* **205**(4-5), 371–379 (1993).

23. Rodriguez, G., John, P. C., and Eden, J. G. *J. Chem. Phys.* **103**(24), 10473–10483 (1995).

24. Engel, V. *Chem. Phys. Lett.* **178**(1), 130 – 134 (1991).

25. Burgi, T. and Leutwyler, S. *J. Chem. Phys.* **101**(10), 8418–8429 (1994).

26. Weiler, M., Miyazaki, M., Feraud, G., Ishiuchi, S.-i., Dedonder, C., Jouvet, C., and Fujji, M. *J. Chem. Phys. Lett* **4**(22), 3819–3823 (2013).

27. Dean, J. C., Navotnaya, P., Parobek, A. P., Clayton, R. M., and Zwier, T. S. *J. Chem. Phys.* **139**(14), 144313 (2013).

Chapter 5

Photodegradation Pathways in Lignins

The role of intramolecular hydrogen bonding in excited states
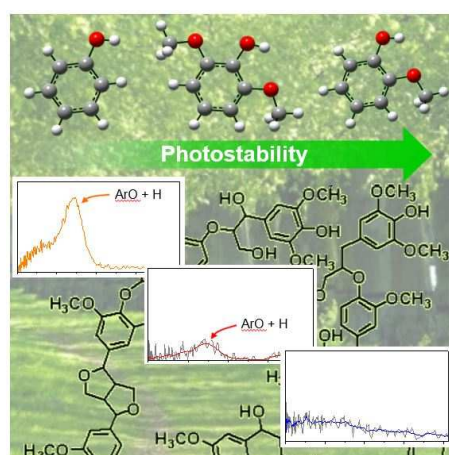
5.1 Introduction

Following on from the *ortho-* substituted phenol-type species, catechol, we now
extend our "bottom-up" approach to the species guaiacol (2-methoxyphenol) and
syringol (2,6-dimethoxyphenol) while, once again, using phenol as a point of com-
parison for the observed excited state dynamics. The structures of these molecules
are shown in Figure 5.1(a-c) which presents an artistic view of the impetus behind
this chapter. By comparing the results here with pre-existing and future investiga-
tions on the monolignols (Figure 5.1(d-f)), we can hopefully garner insight into the
dynamics exhibited by the larger, biological system, lignin (Figure 5.1(g)).

Second only to cellulose, lignin is the most abundant naturally occurring biopoly-
mer on Earth.[1] Present in the cell walls of all vascular plants, it is responsible for
providing structural support, water transport and protection against microorgan-
isms.[1–5] However, due to the heterogeneous nature of the polymer itself, our knowl-
edge of the precise macromolecular structure of lignin is still lacking. It is known
that across different plant species, the various structures, and properties associated
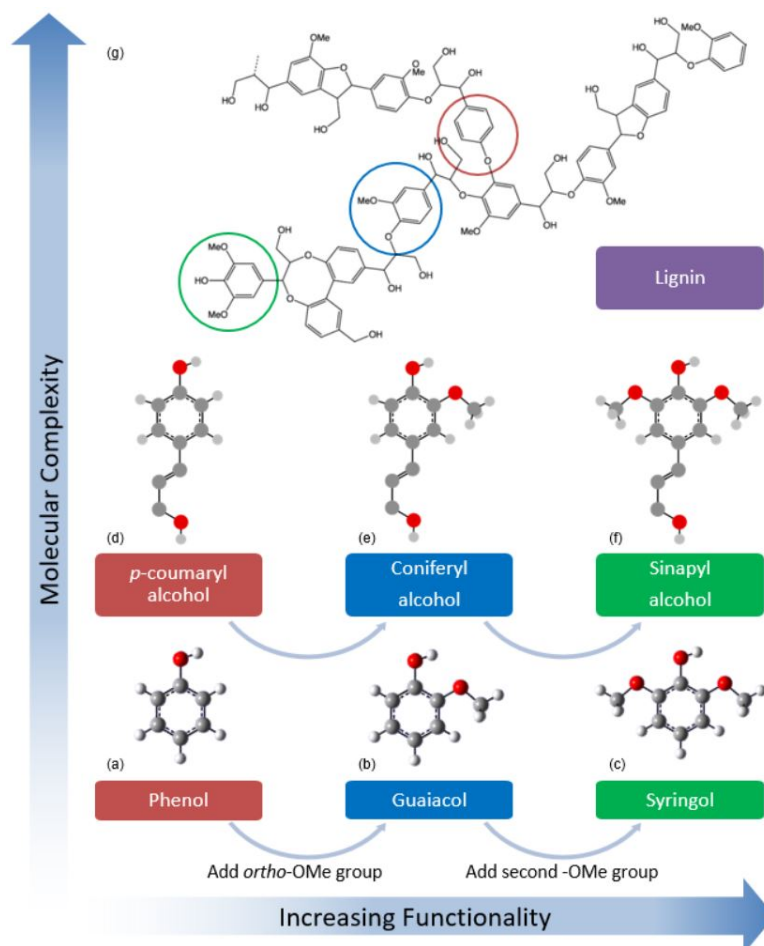
Figure 5.1: (a-c) Chemical structures of the three monolignol chromophores;
phenol, guaiacol and syringol, respectively. (d-f) The related monolignols and
(g) a segment of the naturally occuring biopolymer, lignin with examples of the
chromophores highlighted in the relevant colour.

with them, are dictated by the stoichiometric proportions of the three monolignols presented above: *p*-coumaryl, coniferyl and sinapyl alcohols (Figure 5.1(d-f)).[5,6]

Despite the importance of these molecules, very little is known about the photochemistry of lignin, or the monolignols themselves. Previous high-resolution spectroscopy measurements have been carried out on the closely related analogues *p*-vinylphenol,[7,8] *p*-coumaric acid,[9] and *o*-methoxyphenol (guaiacol).[10] More recently, Zwier and co-workers have reported the first spectroscopic study of the monolignols and β-O-4/β-β dilignols.[11,12] These studies provided new insights into the conformer-specific spectroscopies of model lignins, potentially yielding knowledge of structure-function relationships in the larger polymer network through the "bottom-up" study of the building-blocks themselves. Here, as has been the case throughout this thesis, we use our reductionist approach as a stepping-stone for understanding UV induced photodegradation pathways within lignin in greater detail.

Currently, it is known that one of the primary mechanisms driving photodegredation in these species involves the photo-catalysed formation of phenoxyl-type (ArO, where Ar refers to the phenol, guaiacol or syringol parent molecule) radical sites, generated following the loss of H atoms from the OH moiety, eventually leading to undesired discolouration and structural weakening.[13] With this in mind, we elect to compare and contrast the UV-induced excited state dynamics of phenol, guaiacol and syringol (Figure 5.1(a-c), which are model chromophores of lignin, derived from *p*-coumaryl, coniferyl and sinapyl alcohols, respectively. Similar to catechol (Chapter 4), the presence of the methoxy-group(s) in guaiacol and syringol, *ortho-* to the hydroxy-group, leads to an intramolecular H bond between these two functional moieties, which distorts the geometry from planarity in the first electronically excited $^1\pi\pi^*$ state (S_1), relative to the planar ground state (S_0)
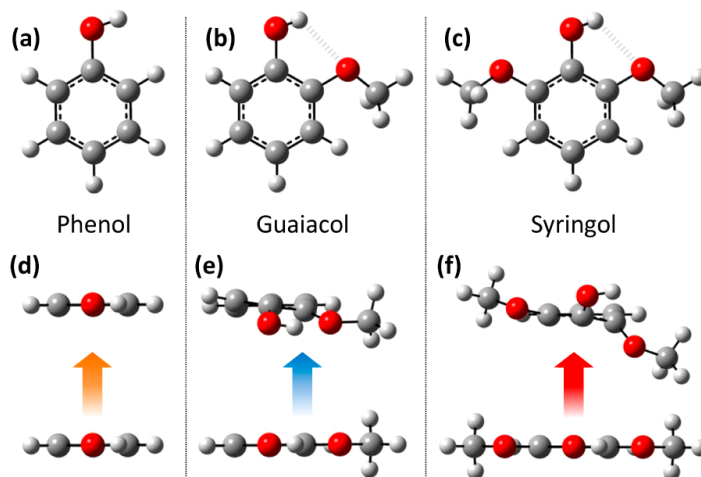
Figure 5.2: (a-c) Chemical structures of the three monolignol chromophores and (d-f) their molecular geometries in both the ground and excited electronic states of the neutral molecule, S_0 and S_1, respectively. Geometries were calculated using TD-M052X/6-311++G(d,p).

structure (Figure 5.2(d-f)).[11,14] In the following chapter, we demonstrate how the different molecular structures of these three UV chromophores in their S_1 states - specifically, the degree of H bonding - can dramatically influence their excited state dynamics and in turn the relative propensies for forming ArO sites (*i.e.* their relative 'photostabilities'), there-by taking a first step towards a more complete *structure-dynamics-function* picture of photodegradation in lignin.

5.2   Experimental

As before, the detailed experimental procedure is described in Chapter 2. Molecular beams were produced by seeding the target molecules (syringol, guaiacol and phenol) into helium at ~2 bar. The valve was heated in order to obtain sufficient vapour pressure of the analyte; typical operating temperatures were ~50 °C, ~40 °C and ~100 °C for syringol, guaiacol and phenol, respectively. Seeded molecular beam pulses were then generated using the Even-Lavie valve[15] operating at a 125 Hz repetition rate with a typical opening time of 13 μs. Following excitation of phenol, guaiacol or syringol using $h\nu_{pu}$, a coherent superposition of low frequency Franck-Condon (FC) active modes are excited in the S_1 state, preparing a vibrational wavepacket as described in Section 1.4 and Chapter 4.[16] As this wave-packet evolves over time, it is then projected (photoionised) onto the ground state of the cation (D_0) by $h\nu_{pr}$, and the resulting parent$^+$ ion signal is recorded as a function of Δt. The pump pulse is centred around the S_1 origin band whilst the probe pulse is tuned to photoionise slightly above the adiabatic ionisation potential (IP$_{ad}$) of the molecule of interest. VMI is used to monitor any loss of H atoms after excitation. Any H atoms are resonantly ionised to form H$^+$ with a 243 nm probe pulse at Δt = 1.2 ns.

5.3   Results and Discussion

5.3.1   Phenol

We begin our discussion with phenol, which once again serves as a benchmark for comparison with guaiacol and syringol. Figure 5.3(a) presents a phenol$^+$ transient (triangles and black line) following excitation at 275 nm and probing with 300 nm. The IP$_{ad}$ of phenol is evaluated as 8.51 eV[18] and thus the combined photon energy of 8.64 eV (275 nm + 300 nm) means we are only above the IP$_{ad}$ by 0.13 eV. The probe wavelengths for phenol, guaiacol and syringol were chosen specifically, in order to be slightly above the IP$_{ad}$, the reason for which we discuss in the ensuing paragraphs. The phenol$^+$ transient is similar to those reported previously using higher probe energies,[17,19] and shows a sharp rise at $\Delta t = 0$ which then plateaus across our 5 ps time window. This plateau is unsurprising, given that the S_1 lifetime of phenol has been previously determined as ~2 ns.[17,19] Further inspection of the transient also shows that, within the signal-to-noise, the ion signal exhibits no obvious 'quantum
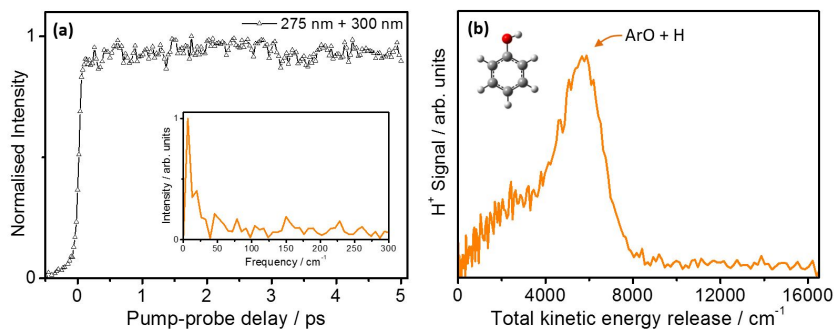
Figure 5.3: (a) TR-IY transients collected from phenol (triangles) following UV excitation and subsequent probing (ionisation) to the resulting phenol$^+$ cation. Inset: The FFT of the transient. (b) The TKER spectra obtained for phenol at 278 nm, adapted from Reference 17.

beating'[16] which suggests that whilst we are creating a coherent superposition of low frequency FC active modes,[20] we are unable to probe this wavepacket motion, in stark contrast to catechol (Chapter 4), guaiacol and syringol (*vide infra*). This is re-enforced by the fast Fourier transform (FFT) of this transient (Figure 5.3(a), inset), which shows no emerging frequencies.

5.3.2 Guaiacol

Figure 5.4(a) presents a guaiacol$^+$ transient following excitation to S_1 with 278 nm and probing with 338 nm (squares and dashed line). The IP_{ad} of guaiacol is located at 7.94 eV,[21] with the combined energy of the pump and probe being 8.12 eV, yielding an excess energy of 0.18 eV. The measured transient of guaiacol$^+$ is similar to that recorded for phenol$^+$ in so much that there is an initial sharp rise at $\Delta t = 0$ which then plateaus within our 5 ps temporal window. However, the similarities with phenol cease here. Following the initial rise, the guaiacol$^+$ signal shows a small, but evident sub-1 ps decay, with a pronounced quantum beat superimposed on top. We recall that, similar to catechol, the S_1 geometry in guaiacol is non-planar (Figure 5.2(e)) in that it distorts out-of-plane in a double minimum potential well. The observed decay is thus attributed to the overall variation in the ionisation cross-section that follows the initial geometry rearrangement out of the FC region as the initially prepared S_1 state evolves towards the non-planar minimum (*cf.* catechol[22]).

We can now utilise a similar approach as was implemented in catechol (Chapter 4) in order to explore the observed quantum beats. Analysis of the guaiacol$^+$ transient with a FFT (Figure 5.4(a), inset) reveals that the beat contains two dominant frequencies with associated energies of 143 cm^{-1} and 163 cm^{-1} (resulting in periodicities of 233 and 205 fs, respectively), which, as we saw in catechol, correspond to wavenumber separations of the vibrational eigenstates within the initially prepared wavepacket.[16] These difference frequencies align very well with the known band separations in an even quanta vibrational progression of the out-of-plane methoxy (OMe) 'flapping' mode (φ), which exhibits by far the largest FC
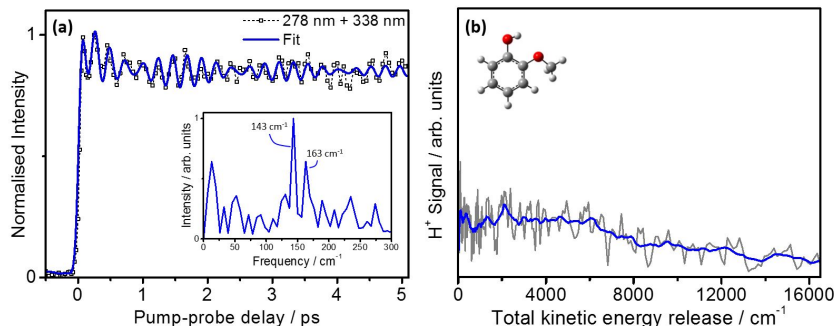
Figure 5.4: (a) TR-IY transients collected from guaiacol (squares) following UV excitation with 278 nm and subsequent probing (ionisation) of the resulting guaiacol$^+$ cation using 338 nm. Superimposed on the data is the sinusoidal fit (blue line). See the text for details. Inset: The FFT for this transient. (b) TKER spectra obtained for guaiacol at 278 nm, the blue line shows a 10 point average through the raw data (grey).

activity in the REMPI/laser induced fluorescence (LIF) spectra (see Reference 14). Dean *et al.* have previously highlighted φ as the dominant motion involved in the initial geometry rearrangement on guaiacol's S_1 surface.[14]

The pronounced beating in φ in Figure 5.4(a) is observed for the same reason we saw in catechol. Referencing the schematic in Figure 4.5(a) once again, following photoexcitation from the planar S_0 ground state in guaiacol, a coherent superposition of even quanta in the OMe flapping mode creates a vibrational wave packet in the non-planar excited state. The final D_0 state of guaiacol$^+$ is planar, and thus the nuclear configuration is once again different, this time between S_1 (non-planar) and D_0 (planar) states. As such, the varying ionisation cross section we observed along the torsional coordinate (ϕ) in catechol is also observed here for guaiacol, this time along the φ (OMe flapping) coordinate.

The broadness of the peaks in the guaiacol FFT (Figure 5.4(a), inset) reflects the limited time window that these beats persist before they dampen out, most likely due to the rapid dephasing of the vibrational wavepacket. This proposition is re-enforced by recalling that our pump pulse is exciting multiple quanta in φ. Indeed, we have extended the guaiacol$^+$ transient out to 100 ps and find no evidence of revivals, suggesting that population in S_1 is channelled irreversibly into modes orthogonal to φ. This contrasts revivals (and fractional revivals) that have been observed in electronic[23–26] and vibrational wavepackets[27–31] excited in atoms and diatomic molecules, respectively. In order to extract a time constant for the dephasing time, τ_{damp}, we fit our measured transient to two cosine functions (with frequencies corresponding to the wavenumber separation of the vibrational states extracted from our FFT), superimposed with an exponential decay (fit details in the appendix). The results of this fit (Figure 5.4(a), blue line) return a dephasing lifetime of $\tau_{damp} = 3.0$ ps, and we discuss the significance of this value below, in relation to the results obtained for syringol.
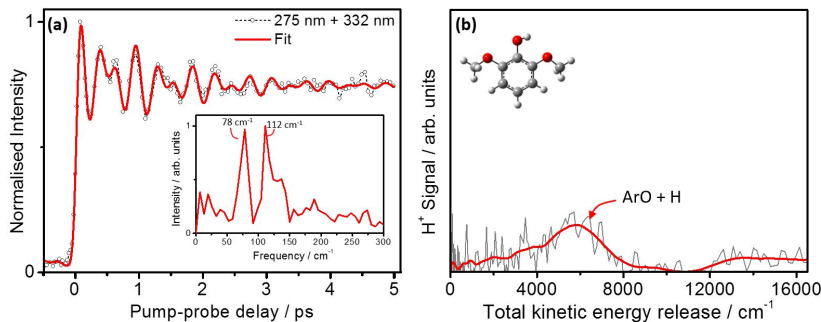
Figure 5.5: (a) TR-IY transients collected from syringol (circles) following UV excitation with 275 nm and ionising with 332 nm. Superimposed on the data is the sinusoidal fit (red line). See the text for details. Inset: The FFT of the transient. (b) Example TKER spectra obtained for syringol at 275 nm, the red line shows a 15 point average through the raw data (grey).

5.3.3 Syringol

Figure 5.5(a) shows the syringol$^+$ transient obtained following excitation at 275 nm and probing at 332 nm (circles and dashed line). The combined photon energy of 8.2 eV is enough to surmount the $\sim$7.9 eV IP$_{ad}$ in syringol with an excess of $\sim$0.3 eV. As with the transient observed in guaiacol (Figure 5.4(a)), following an initial sharp rise at $\Delta t = 0$, there is a clear beating in the syringol$^+$ signal that dampens almost entirely by 5 ps, with no evidence of revivals. Shown inset is the FFT of the same data set, which contains two major frequency components of 78 cm^{-1} and 112 cm^{-1} (resulting in periodicities of 428 and 298 fs, respectively). There also appears to be a weaker component at $\sim$140 cm^{-1}; however, implementing the two major frequency components in our fitting algorithm alone is sufficient to return an excellent fit. As with catechol and guaiacol, these frequencies correspond to wavenumber separations of vibrational states within the wavepacket on S_1, however, spectral congestion in the known REMPI spectrum of syringol (*i.e.* the high density of states (DOS)) makes assigning these modes more cumbersome (see Reference 14). Nonetheless, based on (i) the dominant FC activity of the OMe torsion (ϕ_{OMe}) and φ modes upon excitation to S_1,[14] and (ii) the predicted geometry changes in the S_1 state of syringol (Figure 5.2(f)), these frequencies most likely arise from a coherent superposition of combination modes involving ϕ_{OMe} and φ. Detection of these quantum beats in the TR-IY transient follows for the same reasons outlined above, *i.e.* the presence of a FC detection window arising from the structural distortion between S_1 and D_0 in syringol and syringol$^+$, respectively.

Once again, we fit the syringol$^+$ transient using the method described above (Figure 5.5(a), red line) and extract a dephasing time of $\tau_{damp} = 1.5$ ps, noticeably faster than that observed in guaiacol (*cf.* 3.0 ps). Given that the measured REMPI spectrum of syringol is significantly more congested than that for guaiacol (Reference 14) it is not surprising that the dephasing time determined for syringol is faster; the greater DOS in the initial superposition drives faster dephasing of the vibrational wavepacket.

Intriguingly, we see that the beats in the syringol$^+$ transient (Figure 5.5(a)), relative to the total ion signal, have greater amplitude than those observed in the guaiacol$^+$ transient (Figure 5.4(a)). We offer two possible explanations for this and discuss the validity of each in turn. The first is that in syringol, the initial composition of the wavepacket may only include a limited set of vibrational levels, composed primarily of ϕ_{OMe} and φ modes. However, the REMPI spectrum suggests that the density of vibrational states in S_1 for syringol is far greater than that of guaiacol, as one would expect for a larger molecule (Reference 14) likely ruling out this conjecture. The second is that the FC detection window is more localised in nuclear configuration space for syringol than in guaiacol. Credence to this argument comes from the much greater deviation from planarity in S_1 for syringol *vs* guaiacol. Indeed, time-dependent density functional theory (TD-DFT) calculations on syringol predict that following the $S_1 \leftarrow S_0$ transition, the H bonded OMe group distorts $\sim$50° out-of-plane in one direction, while the OH group, accompanied to a lesser extent by the 'free' OMe group, bends $\sim$25° in the other direction (Figure 5.2(f)). The predicted geometry change is far less pronounced for the OH and OMe groups in guaiacol, as further evidenced by the contrasting profiles of the REMPI/LIF spectra for these two species.[14] Given this fact, coupled with the planar syringol$^+$ geometry, the magnitude of the modulation in ionisation efficiency is expected to be enhanced by virtue of the larger displacement between S_1 and D_0 geometries in syringol (*cf.* Figure 5.2(e) *vs.* (f), and Reference 32).

We highlight that by selecting a probe wavelength such that the combined pump and probe energy far exceeds the IP_{ad}, the beats in the TR-IY signal for guaiacol$^+$ and syringol$^+$ vanish (see Chapter 4). A representative transient collected from syringol, such that the total $h\nu_{\text{pu}} + h\nu_{\text{pr}}$ energy supersedes the IP_{ad} (275 nm +

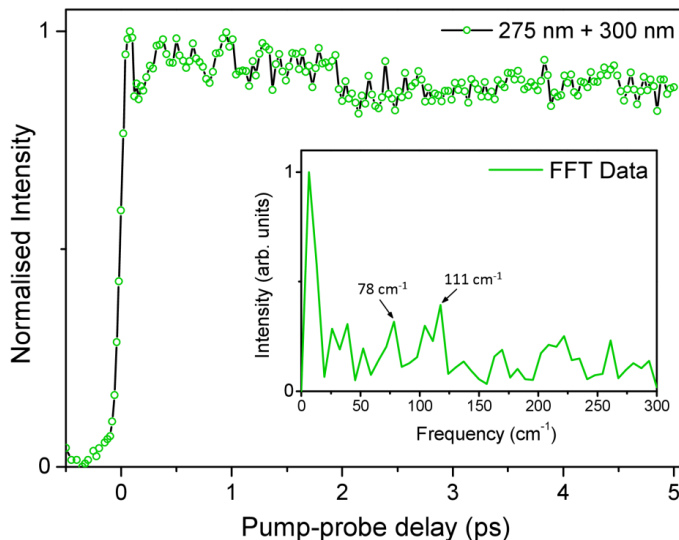**Figure 5.6:** TR-IY transient collected from syringol following UV excitation at 275 nm and subsequent probing using 300 nm, highlighting the lack of coherence (within the collected data) following excitation at pump and probe energies that exceed IP_{ad}. Inset: The FFT of the transient.

300 nm, respectively) is shown in Figure 5.6. Excitation at these wavelengths yields a result similar to that seen for phenol; an initial sharp rise which then plateaus across our 5 ps time window. Inset is the FFT of the reported data; it is clear there is very little evidence of any oscillatory components in the transient, demonstrating the sensitivity of the detection window to the probe wavelength (Figure 4.5(a)), green arrow). We recognise once again that a coherent superposition of vibrational modes is generated irrespective of any structural differences between S_1 and S_0 (*cf.* phenol). However, it is the effective FC window created by this geometry change that allows us to probe the temporal evolution of the prepared wavepacket and observe a quantum beat using TR-IY.

5.3.4   Lignin Chromophore Photostability

Given the above evidence for out-of-plane geometry changes in guaiacol and syringol's S_1 states (relative to S_0 and D_0), which is absent in phenol's, we now pose the question, how does this affect the relative propensities for photoinduced H atom loss and formation of ArO sites in these three lignin chromophores? For phenol, the previously discussed experimental studies demonstrate that the $^1\pi\sigma^*$ (S_2) state, which is dissociative along the O–H coordinate (see potential energy cuts in Section 1.6), is responsible for producing ArO + H species at all excitation energies above (and including) the S_1 origin (*via* either tunnelling beneath the conical intersection (CI) or by ultrafast coupling onto S_2 at shorter wavelengths). This is identified through the characteristic production of high KE H atoms,[33–35] and is in accordance with the original postulate of Sobolewski and Domcke, which we introduced in Section 1.6.1.[36] H atoms produced *via* this mechanism are illustrated by the peak at ∼6000 cm^{-1} in the representative TKER spectrum in Figure 5.3(b). However, as the analogous TKER spectrum in Figure 5.4(b) shows, no similar high KE signature is observed for the production of ArO + H species in guaiacol. A broad component peaked at low KE is observed however, which, as we have shown in previous studies, is multicomponent in nature and attributed to both multiphoton processes and statistical unimolecular decay on S_0.[22,33] We interpret the absence of the high KE feature to be a consequence of the intramolecular H bond between the OH and OMe groups, which induces a barrier to O–H dissociation and aborts any formation of ArO + H products.[37] This also suggests that, despite the photoinduced geometry change inferred from our TR-IY measurements and earlier studies,[14] the intramolecular H bond between the OH and OMe groups is still maintained in the initially excited S_1 state of guaiacol and, as a consequence, the S_1 lifetime increases from ∼2 ns in phenol[17,19] to ∼7 ns in guaiacol (see Reference 22), given that O–H fission is no longer a viable decay pathway. Intramolecular H bonding is also present in the planar S_0 ground state of syringol, although our above analysis suggests that out-of-plane distortion of its OH and OMe groups in S_1 is far more dramatic than guaiacol. This is in-line with the TD-DFT geometry optimisation, presented in Figure 5.2(f), which demonstrates a

large decrease in the proximity of the H bonded OH and OMe moieties following photoexcitation (2.72 $\mathring{A}$ separation between the H atom in OH and the O atom in OMe in S_1, compared to 2.08 $\mathring{A}$ in S_0, and a dihedral angle of $\sim 70°$ between the two groups). This will necessarily weaken the intramolecular H bond, providing a greater potential for the now 'free' O–H bond to undergo dissociation. Indeed, the small high KE feature ($\sim$6000 cm^{-1}) present in the TKER spectrum in Figure 5.5(b) provides evidence that ArO + H photoproducts are formed from syringol, albeit with a far smaller yield than observed for phenol (*cf.* Figure 5.3(b)), which exhibits no steric/structural constraints to photoinduced O–H fission. In support of this, and unlike guaiacol, we note that the measured S_1 lifetime for syringol ($\sim$2.5 ns) is more comparable to that of phenol's. The small broad feature present above $\sim$12000 cm^{-1} is attributed to H$^+$ generated directly through dissociative ionisation,[33] given its persistence when setting our probe wavelength off resonance for H atom detection ($h\nu_{\mathrm{pr}} \neq 243$ nm).

For completeness, we note that at much shorter wavelengths ($\leq$220 nm) all three chromophores generate ArO + H products as demonstrated by the TKER spectra in Figure 5.7, derived from H Rydberg atom photofragment translational spectroscopy (HR-PTS) measurements of jet-cooled samples of syringol at 215 nm (a) and guaiacol at 220 nm (b). As Figure 5.7 shows, the TKER spectra are qualitatively similar to those reported previously for photolysis of many other phenols,[33] exhibiting a 'fast' feature centred at TKER $\sim$10000 cm^{-1} that is consistent with direct O–H bond fission along the S_2 ($^1\pi\sigma^*$) potential energy surface. This result is somewhat unsurprising given that excitation at such short wavelengths is
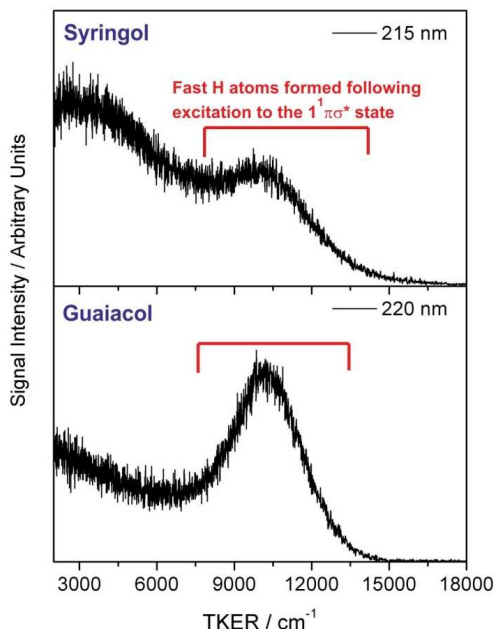

Figure 5.7: (a) TKER spectra collected from syringol following UV excitation at 215 nm and (b) the spectra obtained following excitation of guaiacol at 220 nm. The clear high KE feature centred at TKER $\sim$10000 cm^{-1} is consistent with direct O-H bond fission on the $^1\pi\sigma^*$ (S_2) potential energy surface.

likely populating vibrational modes in S_1 that lie above the S_1/S_2 CI, allowing for ultrafast coupling onto S_2, or directly exciting the dissociative state.[22]

5.4 Conclusions and Outlook

In the preceding chapter we have explored the early time vibrational motions in phenol, guaiacol and syringol; chromophores of the important bio-polymer lignin. For the latter two species, we used time-resolved ion yield measurements in order to create a sensitive Franck-Condon window that allows the temporal evolution of the vibrational wavepacket created following excitation to be tracked as a function of time. The FC window is afforded by the dramatic geometry change upon photoionisation, as was shown for catechol in Chapter 4. While the creation of the probing window is the same between the two chapters, the results observed here highlight a situation wherein the photoprepared wavepacket very quickly (~3.0 ps and ~1.5 ps for guaiacol and syringol, respectively) dephases as a result of efficient IVR to modes orthogonal to the φ/ϕ_{OMe} coordinates.

    We close by returning to our original question of the relative photostabilities of these three lignin chromophores. Based on the knowledge that ArO radical formation drives photodegradation of the lignin biopolymer, the relative photostabilities of the chromophore sites can be broadly ordered as guaiacol > syringol > phenol (in order of decreasing stability), which, with the exception of phenol, we understand to largely be dictated by the degree of H bonding preserved after out-of-plane rearrangement in their S_1 excited states. Naturally, the findings from the present study only consider the photostability of lignin's isolated chromophores in the gas phase (and at select wavelengths[i]), although we note that solvation effects (*e.g.* from H_2O) are likely to be minimal given the highly hydrophobic nature of the larger biopolymer[13] suggesting the gas phase can act as a good benchmark here. It is interesting to note that there is evidence of this ordering in the composition of natural lignin, which is often dominated by coniferyl alcohol and in many cases contains <10 % *p*-coumaryl alcohol.[38] With this in mind, future studies of the lignin building-blocks will be important to further verify how this behaviour maps onto larger components of lignin. High-resolution spectroscopy measurements already suggest that in para substituted analogues of these chromophores, distorted excited state geometries will still likely play a role in the ensuing dynamics.[14] The work here therefore offers another key step towards developing a more intimate *structure-dynamics-function* understanding of photodegradation in lignin.

---

[i]The present studies have focused on photoexcitation around the S_1 origin of these chromophores. At higher excitation energies ($\leq$220 nm), we acknowledge that H atom loss from the OH group becomes active in all three chromophores as seen in Figure 5.7. This does not, however, affect our overall conjecture about their relative photostabilities within lignin, given that (i) solar irradiance will be significantly reduced at these much shorter UV wavelengths and (ii) the total propensity for O-H bond fission across their full UV absorption range still follows the order given in the main text.

References

1. Boerjan, W., Ralph, J., and Baucher, M. *Annu. Rev. Plant Biol.* **54**, 519–546 (2003).

2. Vanholme, R., Demedts, B., Morreel, K., Ralph, J., and Boerjan, W. *Plant Physiol.* **153**(3), 895–905 (2010).

3. Morreel, K., Kim, H., Lu, F., Dima, O., Akiyama, T., Vanholme, R., Niculaes, C., Goeminne, G., Inze, D., Messens, E., Ralph, J., and Boerjan, W. *Anal. Chem.* **82**(19), 8095–8105 (2010).

4. van der Hage, E. R. E., Boon, J. J., Steenvoorden, R. J. J. M., and Weeding, T. L. *Anal. Chem.* **66**(4), 543–550 (1994).

5. Evtuguin, D. V. and Amado, F. M. L. *Macromol. Biosci.* **3**(7), 339–343 (2003).

6. Reale, S., Di Tullio, A., Spreti, N., and De Angelis, F. *Mass Spectrom. Rev.* **23**(2), 87–126 (2004).

7. de Groot, M., Buma, W. J., Gromov, E. V., Burghardt, I., Koppel, H., and Cederbaum, L. S. *J. Chem. Phys.* **125**(20) (2006).

8. Morgan, P. J., Mitchell, D. M., and Pratt, D. W. *Chem. Phys.* **347**(1-3), 340–345 (2008).

9. Smolarek, S., Vdovin, A., Perrier, D. L., Smit, J. P., Drabbels, M., and Buma, W. J. *J. Am. Chem. Soc.* **132**(18), 6315 (2010).

10. Fujimaki, E., Fujii, A., Ebata, T., and Mikami, N. *J. Chem. Phys.* **110**(9), 4238–4247 (1999).

11. Rodrigo, C. P., James, William H., I., and Zwier, T. S. *J. Am. Chem. Soc.* **133**(8), 2632–2641 (2011).

12. Dean, J. C., Walsh, P. S., Biswas, B., Ramachandran, P. V., and Zwier, T. S. *Chem. Sci.* **5**(5), 1940–1955 (2014).

13. George, B., Suttie, E., Merlin, A., and Deglise, X. *Polym. Degrad. Stab.* **88**(2), 268–274 (2005).

14. Dean, J. C., Navotnaya, P., Parobek, A. P., Clayton, R. M., and Zwier, T. S. *J. Chem. Phys.* **139**(14), 144313 (2013).

15. Even, U., Jortner, J., Noy, D., Lavie, N., and Cossart-Magos, C. *J. Chem. Phys.* **112**(18), 8068–8071 (2000).

16. Zewail, A. H. *Angew. Chem., Int. Edit.* **39**(15), 2587–2631 (2000).

17. Roberts, G. M., Chatterley, A. S., Young, J. D., and Stavros, V. G. *J. Chem. Phys. Lett* **3**(3), 348–352 (2012).

18. Lipert, R. J. and Colson, S. D. *J. Chem. Phys.* **92**(5), 3240–3241 (1990).

19. Pino, G. A., Oldani, A. N., Marceca, E., Fujii, M., Ishiuchi, S. . I., Miyazaki, M., Broquier, M., Dedonder, C., and Jouvet, C. *J. Chem. Phys.* **133**(12), 124313 (2010).

20. Nix, M. G. D., Devine, A. L., Cronin, B., Dixon, R. N., and Ashfold, M. N. R. *J. Chem. Phys.* **125**(13), 133318 (2006).

21. Yuan, L. W., Li, C. Y., Lin, J. L., Yang, S. C., and Tzeng, W. B. *Chem. Phys.* **323**(2-3), 429–438 (2006).

22. Chatterley, A. S., Young, J. D., Townsend, D., Zurek, J. M., Paterson, M. J., Roberts, G. M., and Stavros, V. G. *Phys. Chem. Chem. Phys.* **15**(18), 6879–6892 (2013).

23. Verlet, J. R. R., Stavros, V. G., Minns, R. S., and Fielding, H. H. *J. Phys. B-At. Mol. Opt.* **36**(17) (2003).

24. Verlet, J. R. R., Stavros, V. G., Minns, R. S., and Fielding, H. H. *Phys. Rev. Lett.* **89**, 263004 Dec (2002).

25. Stavros, V. G., Ramswell, J. A., Smith, R. A. L., Verlet, J. R. R., Lei, J., and Fielding, H. H. *Phys. Rev. Lett.* **83**(13), 2552–2555 (1999).

26. Wals, J., Fielding, H. H., Christian, J. F., Snoek, L. C., Van Der Zande, W. J., and Van Linden Van Den Heuvell, H. B. *Phys. Rev. Lett.* **72**, 3783–3786 Jun (1994).

27. Dantus, M., Bowman, R. M., and Zewail, A. H. *Nature* **343**(6260), 737–739 (1990).

28. Farmanara, P., Ritze, H.-H., Stert, V., and Radloff, W. *Chem. Phys. Lett.* **307**(12), 1 – 7 (1999).

29. Fischer, I., Vrakking, M. J. J., Villeneuve, D. M., and Stolow, A. *Chem. Phys.* **207**(2-3), 331–354 (1996).

30. Vrakking, M. J. J., Villeneuve, D. M., and Stolow, A. *Phys. Rev. A* **54**, R37–R40 Jul (1996).

31. Goto, H., Katsuki, H., Ibrahim, H., Chiba, H., and Ohmori, K. *Nat. Phys.* **7**(5), 383–385 (2011).

32. Rodriguez, G., John, P. C., and Eden, J. G. *J. Chem. Phys.* **103**(24), 10473–10483 (1995).

33. Roberts, G. M. and Stavros, V. G. *Chem. Sci.* **5**(5), 1698–1722 (2014).

34. Dixon, R. N., Oliver, T. A. A., and Ashfold, M. N. R. *J. Chem. Phys.* **134**(19), 194303 (2011).

35. Ashfold, M. N. R., Devine, A. L., Dixon, R. N., King, G. A., Nix, M. G. D., and Oliver, T. A. A. *Proc. Natl. Acad. Sci. U. S. A.* **105**(35), 12701–12706 (2008).

36. Sobolewski, A. L., Domcke, W., Dedonder-Lardeux, C., and Jouvet, C. *Phys. Chem. Chem. Phys.* **4**(7), 1093–1100 (2002).

37. Yang, Y. L., Ho, Y.-C., Dyakov, Y. A., Hsu, W.-H., Ni, C.-K., Sun, Y.-L., Tsai, W.-C., and Hu, W.-P. *Phys. Chem. Chem. Phys.* **15**, 7182–7190 (2013).

38. Baucher, M., Monties, B., Van Montagu, M., and Boerjan, W. *Crit. Rev. Plant Sci.* **17**(2), 125–197 (1998).

Chapter 6

Conclusions and Outlook

6.1 Summary

The approach applied in this thesis is "bottom-up" gas phase spectroscopy. By starting with 'simpler' molecules we are able to form a foundation of knowledge that we are then able to methodically build on in order to understand the excited state relaxation mechanisms exhibited by larger, more realistic systems, following absorption of UV radiation. The highly complementary techniques of time-resolved ion yield and velocity map imaging provide unprecedented insight into the excited state dynamics of the target species, and by coupling with high level *ab initio* calculations, we are able to rationalise the dynamics of increasingly complex biologically relevant molecules.

We began this thesis with an overview of photophysics and gas phase femtochemistry. The introduction, which was by no means an exhaustive list, covered the fundamental concepts that were pertinent to the results chapters presented; starting with the photophysical and photochemical processes that can occur in molecules followed by the quantum mechanical principles that govern these processes. The femtosecond probing techniques utilised throughout, TR-IY and TR-VMI, were then described in detail. Finally, a brief introduction to photostability was presented, focussing primarily on the archetypal system, phenol. Phenol was chosen as the basis for our "bottom-up" approach due to the myriad of investigations already performed on the system and because it provides a wonderful platform upon which to increase molecular complexity with further functionalisation of the heteroaromatic system.

An outline of the experimental setup utilised in these experiments was presented in Chapter 2. This included a summary of the femtosecond laser system, with details regarding the generation of pump and probe pulses, followed by an in depth look at the vacuum chambers, and the components contained therein, that make up our experiment. Particular attention was paid to the generation of molecular beams and the arrangement of components that allows for the accurate recording, and subsequent analysis, of TR-IY and TR-VMI information.

Chapter 3 explored the excited state dynamics of resorcinol (1,3-dihydroxybenzene) following UV excitation at a range of pump wavelengths, $\lambda = 278$ - 255 nm. The techniques employed provided an excellent overview of how a combination of ultrafast TR-VMI and TR-IY measurements coupled with complementary *ab initio* calculations can provide a rigorous description of a molecule's excited state dynamics following interaction with UV light. It was seen that after promoting population to the $1^1\pi\pi^*$ state, the timescale, τ_1, for excited state relaxation decreased as a function of excitation energy from 2.70 ns to $\sim$120 ps. This increase in relaxation rate was assigned to competing deactivation mechanisms. Tunnelling beneath the $1^1\pi\pi^*/^1\pi\sigma^*$ conical intersection, followed by coupling onto the dissociative $^1\pi\sigma^*$ state, yielded H atoms born with high kinetic energy ($\sim$5000 cm^{-1}). We postulated that this mechanism is in direct competition with an internal conversion process that is able to transfer population from the photoexcited $1^1\pi\pi^*$ state back

to a vibrationally excited ground state, S_0^*. The results presented highlighted the profound effect that the presence of additional functional groups, and more specifically the precise location of the functional groups, can have on the excited state dynamics of model heteroaromatic systems and provided an excellent starting point for the remaining species investigated in this thesis.

In Chapter 4, building on the knowledge obtained from the previous chapter, we excited a coherent superposition of vibrational states in the first excited electronic state (S_1) of 1,2-dihydroxybenzene (catechol) in order to explore the vibrational motions present at the very early stages of the excited state dynamics. Excitation of the *ortho-* substituted species resulted in the formation of a vibrational wave packet which could be probed due to the FC window afforded by the pronounced geometry change upon photoionisation from S_1 to the ground state of the cation (D_0). Little to no dephasing of the created wavepacket was observed and the beats were seen to persist for the duration of the excited state lifetime ($\sim$10 ps) implying that IVR is not a dominant feature of catechol's relaxation dynamics, at least at the early stages of deactivation. The observed quantum beats, which, by comparison to frequency resolved experiments, we assigned to superpositions of the strongly mixed, low-frequency OH torsional mode τ_2, elegantly demonstrated how changes in geometry upon photoionisation from the S_1 state to the ground state of the cation (D_0) enables one to probe vibrational motion (and thus, energy flow) at the very early stages of photoexcitation in an important biological chromophore.

Finally, Chapter 5 explored the photoinduced dynamics of the lignin building blocks syringol, guaiacol, and phenol. Following UV irradiation of syringol and guaiacol, a coherent superposition of out-of-plane OH torsion and/or OMe torsion/flapping motions was created in the first excited $^1\pi\pi^*$ (S_1) state, again resulting in the formation of a vibrational wavepacket. The temporal evolution of said wavepacket was then probed by virtue of the dramatic nonplanar $\rightarrow$ planar geometry change upon photoionisation. Phenol was incorporated into this study as a point of comparison, since no analogous geometry change is present following excitation, and so any similar quantum beat pattern was absent. In syringol, the distortion away from planarity in S_1 was shown to be pronounced enough to actually reduce the degree of intramolecular H bonding (between OH and OMe groups), enabling H atom elimination from the OH group; something that was not seen in guaiacol. H bonding is preserved after excitation in guaiacol, despite the nonplanar geometry in S_1, which prevents O-H bond fission. The excited state behaviour seen in these three systems affects the propensity for forming undesired phenoxyl radical species which could be damaging to the larger biopolymer. Our conclusions on the relative "photostabilities" of the lignin chromophores (phenol < syringol < guaiacol) were beautifully corroborated by nature itself, with the literature showing that the stoichiometric proportion of these systems follows this trend across a plethora of biological samples.

6.2 Outlook and Future Work

The work in this thesis has demonstrated not only the versatility of time-resolved ion yield and velocity map imaging techniques, but we have also explored the profound effect that even simple modifications to a molecule's complexity can have on the ensuing excited state dynamics. Looking to the future there is huge potential for the techniques utilised in this thesis to be used in the study of larger and more biologically relevant systems. There are a number of avenues for future research that the group is currently exploring and a brief selection of possible investigations is outlined below. Additionally, further collaboration between our group with other laboratories should result in extremely exciting and detailed insights into more complex molecular systems.

6.2.1 Vibrational Motion in Related Systems

In Chapters 4 and 5 we used time-resolved ion yield as an effective probe for vibrational motion following excitation to an electronic excited state. The varying ionisation cross-section that we utilised as our sensitive probing method was afforded by a structural distortion in the excited state. In theory, provided a molecule exhibits an analogous geometry change upon photoexcitation (coupled with strong FC activity in the low-lying vibrational modes), vibrational motions can be investigated in that system. This can hopefully lead to further details regarding how vibrational modes couple with one another in the electronic excited states of other important biological chromophores, which could provide invaluable insight into the relaxation mechanisms that are in operation.

6.2.2 Extension to the Solution Phase

Future experiments could extend our "bottom-up" approach towards an understanding of the effect solvent has on the excited state dynamics of biological chromophores. There are two main approaches available: firstly direct collaboration with solution phase experimentalists allow comparative studies to be performed. In our laboratory, solution phase femtosecond experiments are now routinely performed using time-resolved electronic (UV/Vis) absorption spectroscopy. A fine example of a recent intra-group, dual-phase experiment can be seen in Reference 1.

Secondly, solvent effects can be measured in the gas phase, by performing clustering experiments. In experiments such as these, the molecule or ion of interest is clustered with a small number of solvent molecules (*e.g.* water, ammonia, methanol *etc.*), allowing the effect of solvation to be investigated in a step-wise fashion (*i.e.* small-to-large clusters). Another avenue of research would be to explore the effect of clustering on the early time vibrational motions in catechol. These experiments have the potential to enable the observation of intermolecular energy transfer through the dampening of vibrational motions. Preliminary TR-IY measurements

on the catechol dimer and catechol.$(H_2O)_n$ where $n = 1$ or 2, have indicated that even small clusters have a dramatic effect on the observed coherent wavepackets and the excited state lifetime.

6.2.3 Sunscreen Molecules

Despite the widespread use of sunscreens, very little is known regarding the photochemistry/photophysics of the molecules incorporated in the many commercially available lotions. While they are designed to protect human skin from the harmful effects of the UV radiation from the Sun, the photochemistry of large biomolecules may result, for example, in the formation of free radicals responsible for DNA damage, and, consequently, cancer.[2,3] Studying these compounds is essential to evaluating their safety and provides vital information that may lead to the development of more efficient sunscreens in the future.

Recent theoretical work by Karsili *et al.* suggests OH/OMe bond extensions, ring centred out-of-plane deformations and E/Z photoisomerism are all potentially operative internal conversion pathways for ferulic acid, a common sunscreen component.[4] The $^1\pi\pi^*$ and $^1n\pi^*$ states of ferulic acid are found to be close in energy and possess multiple conical intersections, suggesting possible deactivation pathways exist between these states. We have recently taken steps within the group (utilising solution- and gas-phase methodologies) to explore these deactivation mechanisms in a number of naturally occuring (plant) and commercial (synthesised) sunscreen molecules.[5,6] The knowledge garnered by performing gas-phase measurements have thus far proven vital in the effort towards unravelling the complex solution phase dynamics.

References

1. Horbury, M. D., Baker, L. A., Quan, W.-D., Young, J. D., Staniforth, M., Greenough, S. E., and Stavros, V. G. *J. Phys. Chem. A* (2015).

2. Stavros, V. G. *Nat. Chem.* **6**(11), 955–956 (2014).

3. Sambandan, D. R. and Ratner, D. *J. Am. Acad. Dermatol.* **64**(4), 748–758 (2011).

4. Karsili, T. N. V., Marchetti, B., Ashfold, M. N. R., and Domcke, W. *J. Phys. Chem. A* **118**(51), 11999–12010 (2014).

5. Baker, L. A., Horbury, M. D., Greenough, S. E., Ashfold, M. N., and Stavros, V. G. *Photochem. Photobiol. Sci.* **14**(10), 1814–1820 (2015).

6. Baker, L. A., Horbury, M. D., Greenough, S. E., Coulter, P. M., Karsili, T. N., Roberts, G. M., Orr-Ewing, A. J., Ashfold, M. N., and Stavros, V. G. *J Phys. Chem. Lett.* **6**(8), 1363–1368 (2015).

Appendix A

Appendix: Fit Functions

A.1 Fitting Parent and H atom Transients

The fitting of time resolved ion yield and velocity map imaging transients requires the use of multiple fitting functions; in particular a Gaussian distribution, an exponential decay and an exponential rise. The latter two are convoluted with a Gaussian which represents our instrument response function (IRF). Where more than one exponential function (rise or decay) is required to accurately fit the data, combinations of the following functions can be utilised.

The Gaussian distribution in terms of pump probe delay (Δt) has the form:

$$g(\Delta t) = y_0 + A \, exp \left(\frac{(t - t_0)^2}{2\sigma^2} \right) \tag{A.1}$$

where y_0 is the baseline offset, A is the magnitude, t_0 is time zero (the centre of the Gaussian) and σ is the peak width which can be related to the full width at half maximum (FWHM) by the following:

$$\sigma = \frac{\text{FWHM}}{2\sqrt{2 \, ln2}} \tag{A.2}$$

The IRF convoluted exponential decay has the form:

$$f(\Delta t) = g(\Delta t) \otimes A \, exp \left(-\frac{(t - t_0)}{\tau} \right) \tag{A.3}$$

where A is the function's magnitude, t is the offset from time zero, τ is the rise time and $g(\Delta t)$ is the convoluted Gaussian, from Equation A.1, that models the IRF.

The closely related exponential rise, which is also convoluted with the IRF, has the form:

$$f(\Delta t) = g(\Delta t) \otimes A \left[1 - exp \left(-\frac{(t - t_0)}{\tau} \right) \right] \tag{A.4}$$

where all paramaters are as described above.

A.2 Fitting TKER Spectra

The fitting of TKER spectra (where appropriate) uses a combination of functions to fit the low energy statistical feature and high energy features (such as those that arise from dissociation along $\pi\sigma^*$ states). These functions are a Boltzmann distribution and a Gaussian distribution. The Gaussian function is as described above while the Boltzmann distribution, in terms of the TKER (x), has the form:

$$f(x) = y_0 + \frac{A\sqrt{x}}{exp(x/w)} \tag{A.5}$$

where y_0 is the baseline offset, A is the pre-exponential factor and W is the distribution width.

A.3 Fitting Quantum Beats

A.3.1 Catechol

The TR-IY transients in Chapter 3.5 are modelled using a combination of (i) an exponential decay, τ_{dec}, which reflects the lifetime of the S_1 state; this is convoluted with a Gaussian IRF, $g(\Delta t)$ (Equation A.1), of $\sim$120 fs, (ii) two cosine components that describe the two oscillatory components from the FFT, ω_1 and ω_2, with associated phase-shifts of p_1 and p_2 and (iii) an exponential decay which takes into account the damping of the photoexcited wavepacket (τ_{damp}). These functions are in the order described above, and have the form:

$$y = \left(g(\Delta t) \otimes A' \, exp^{\frac{-\Delta t}{\tau_{dec}}} \right) \times \left(\left[(B\cos((\omega_1\Delta t) + p_1) + \ldots \right. \right.$$
$$\left. \left. C\cos((\omega_2\Delta t) + p_2)) \times \, D \, exp^{\frac{-\Delta t}{\tau_{damp}}} \right] + A'' \right) \tag{A.6}$$

In the above, $A' - D$ describes the amplitude of each component function in the total fit. The offset of amplitude A'' is input to ensure that the two cosine components do not force the signal into negative amplitude at any point.

In order to produce the scaled trace in Figure 4.5(c), the fit function from Figure 4.4 is scaled with respect to the S_1 lifetime. The resulting function is as follows:

$$y = \frac{\left(g(\Delta t) \otimes A' \, exp^{\frac{-\Delta t}{\tau_{dec}}} \right) \times \left(\left[(B\cos((\omega_1\Delta t) + p_1) + C\cos((\omega_2\Delta t) + p_2)) \times D \, exp^{\frac{-\Delta t}{\tau_{damp}}} \right] + A'' \right)}{\left(g(\Delta t) \otimes A' \, exp^{\frac{-\Delta t}{\tau_{dec}}} \right)} \tag{A.7}$$

A.3.2 Syringol and Guaiacol

TR-IY transients for Chapter 4.4 are modelled using a modified form of the equation above in which an additional decay function is incorporated to take into account the initial geometry rearrangement seen for these species. The function consists of (i) an exponential decay, τ_{dec}, reflecting the lifetime of the S_1 state; this is convoluted with the Gaussian IRF, $g(\Delta t)$ (Equation A.1), (ii) two cosine components that describe the two oscillatory components from the FFT, ω_1 and ω_2, with associated phase-shifts of p_1 and p_2 (iii) an exponential decay which takes into account the dephasing lifetime, τ_{damp}, of the photoexcited wavepacket and (iv) an exponential decay to reflect the timescale for the initial geometry relaxation from the vertical excitation geometry in S_1, τ_{GR}. These functions are in the order described above, and have the form:

$$
\begin{aligned}
y = \left(g(\Delta t) \otimes A\, exp^{\dfrac{-\Delta t}{\tau_{dec}}} \right) &\times \left(\left[(B \cos((\omega_1 \Delta t) + p_1) + \ldots \right.\right. \\
C \cos((\omega_2 \Delta t) + p_2)) &\times \left. D\, exp^{\dfrac{-\Delta t}{\tau_{damp}}} \right] \left. + E\, exp^{\dfrac{-\Delta t}{\tau_{\mathrm{GR}}}} \right)
\end{aligned}
\tag{A.8}
$$

where $A - E$ corresponds to the contribution of each component function to the total fit.